NORTHWESTERN UNIVERSITY

Efficient Simulation Techniques for Dielectrics and Their Effects on
Electrolytes and Patchy Colloids

A DISSERTATION

SUBMITTED TO THE GRADUATE SCHOOL
IN PARTIAL FULFILLMENT OF THE REQUIREMENTS

for the degree

DOCTOR OF PHILOSOPHY

Field of Physics

By

Huanxin Wu

EVANSTON, ILLINOIS

December 2017

ABSTRACT

Efficient Simulation Techniques for Dielectrics and Their Effects on Electrolytes and

Patchy Colloids

Huanxin Wu

Many phenomena that occur on the nanoscale, such as the electric double layer and the self-assembly of charged nanoparticles, are driven by the electrostatic force. Although current simulation techniques can handle the long-range Coulomb potential efficiently, the inhomogeneity in materials of such systems often gives rise to significant polarization charges that have to be determined by solving the non-trivial Poisson's equation. Thus, dielectric effects are often ignored in previous simulation studies despite their potential importance. This dissertation presents various techniques that can resolve the polarization charges efficiently. These techniques are applied to uncover the significance of dielectric effects in several systems.

In Chapter 1, the mathematical formulation for charged systems that involve inhomogeneous dielectric media is introduced.

Chapter 2 presents a detailed comparison between the iterative dielectric solver (IDS), a recently developed boundary-element-based algorithm that is optimized for molecular

dynamics (MD) simulations, and the generalized image-charge method that is designed for Monte Carlo (MC) simulations. Both algorithms are applied to study the interaction between two colloids immersed in electrolytes. I find that the IDS excels the image-charge method in both efficiency and capability when multiple colloids are concerned.

In Chapter 3, the IDS is applied to study the asymmetric electrolyte distribution near dielectric interfaces that exhibit structures on the nanoscale. I demonstrate that even for neutral dielectric interfaces, surface structures can alter the ion distribution and further create charge patterns on the surfaces.

Chapter 4 introduces a refinement to the IDS to accurately compute polarization charges for anisotropic particles. We discover that the matrix equation of the IDS can be ill-conditioned when multiple dielectric mismatches are present. An effective yet intuitive method is proposed to improve the accuracy.

In Chapter 5, the improved IDS is applied to study the electrolyte distribution near patchy particles, in particular Janus particles. The findings reveal that dielectric effects substantially influence the electric double layer, which has important implications for biological objects with dielectric anisotropy.

Chapter 6 further extends the IDS to treat conducting surfaces and bulk dielectrics, objects with spatially varying permittivities. First, by imposing the Dirichlet boundary condition, I show that the IDS is capable of solving equipotential problems, and even problems with mixed boundary conditions. Then systems with bulk dielectrics are considered. With the extension of the IDS to the volume-element method, the algorithm

obtains results identical to the theoretical prediction for the image potential of a silica–silicon slab. These two extensions of the IDS open avenues to simulate a collection of problems with polarization effects.

In Chapter 7, the excess surface tension of asymmetric electrolytes at dielectric interfaces is studied via a combination of MC simulations and the charge renormalization theory. I find that charge renormalization not only affects the bulk behavior of asymmetric electrolytes but also their properties at interfaces. For an electrolyte–metal interface, the surface tension could be non-monotonic at low concentrations.

I conclude this dissertation with a brief summary of the main findings and some outlook for each chapter in Chapter 8.

Acknowledgements

I would like to thank my advisor, Prof. Erik Luijten. Inspired by his expertise and passion for computational soft matter, I embarked on this challenging yet rewarding journey five years ago. From him, I received strong support and learned numerous valuable lessons, perfectionism, attention to details, critical thinking, presentation skills, to name a few. Many years later, I will probably miss the long afternoon discussions Erik and I had, brainstorming and debating ideas on dielectrics.

This dissertation owes many thanks to other committee members, Prof. John Marko and Prof. Monica Olvera de la Cruz. The advices they offered at my thesis proposal and later meetings are essential for me to improve this research.

Most of my research is also made possible by all my innovative and hard-working collaborators, Prof. Monica Olvera de la Cruz, Prof. Vinayak P. Dravid, Prof. Chad. A. Mirkin, Prof. Zhenli Xu, Prof. Xiangjun Xing, Prof. Francisco Solis, Zecheng Gan, Mingnan Ding, Ming Han and Benjamin D. Myers. My special thanks to Dr. Kipton Barros, who created the iterative dielectric solver that provides a solid foundation for my work.

This journey is definitely more enjoyable with the companion of many brilliant labmates, Wei Qu, Bernard Beckerman, Ming Han, Zonghui Wei, Amir Maghsoodi, Ziwei Wang, Hanne Antila, Ian Patrick Madden, Hang Yuan, Ryan Franks and Amelia Plunk. I also feel fortunate to have spent my first year in graduate school with Prof. James Sauls,

whose deep theoretical knowledge and absolute dedication to teaching I always admire. Being an international student, I built long-lasting friendships with many of my Chinese colleagues, Bo Fu, Xu Chen, Siyuan Shi, Li Zeng, Hao Wu, Xiao Chen, Kaicheng Zhang, etc.

Lastly, I extend deep gratitude to my family, Hang Xie, and my friends for they are my wells of joy when the milestones are achieved and my sources of strength when the future is obscure.

Dedication

To the memory of Peilan Huang, for her unfading love.

Life is so beautiful. It's a pity that we have to say goodbye.

To my family.

Table of Contents

List of Figures

CHAPTER 1

Introduction

Electrostatic interactions are of fundamental importance for understanding the structure–function relationships of many physical and biological systems, including colloidal suspensions, membranes, biopolymers, and energy devices [3, 4, 5]. All-atom computer simulations of such systems are generally prohibitively expensive, due to the required repeated evaluation of the forces or internal energies of molecular configurations. Thus, continuum approximations and coarse-grained models are often adopted. For example, the solvent is usually treated as an implicit continuum described by a (static) dielectric permittivity. The ion distributions in this solvent can be described by mean-field approximations such as the Poisson–Boltzmann theory and its modifications [6, 7, 8, 9]. These continuum models have been widely used, but are only accurate in limited parameter regimes, as polarization and many-body effects are often ignored.

Alternatively, water can be treated in the continuum approximation, whereas the ions are treated as discrete particles, incorporating ionic correlations and ion-size effects. This coarse-graining strategy, the so-called primitive model for electrolytes, is commonly employed in particle-based molecular dynamics (MD) or Monte Carlo (MC) simulations (see, e.g., [10, 11]). Although this is a powerful approach, a formidable computational challenge that remains is the rapid calculation of electrostatic polarization due to the dielectric mismatch at material interfaces, such as the dielectric contrast between the implicit solvent and the solutes. Polarization is relevant in a wide range of systems,

including colloidal suspensions [12, 13, 14], cloud droplets [15, 16], and protein folding and stabilization [17]. Determination of the polarization field through analytical solution of Poisson's equation is very difficult. Closed-form representations, in the form of harmonic series, of the Green's function are known only for specific geometries such as planar, spherical, and cylindrical interfaces [18, 19, 20, 21, 13, 22, 23]. Moreover, even if the closed-form Green's function is employed, the computation of the harmonic series during simulations can still be too expensive if large systems are investigated.

For these reasons, methods for the determination of electrostatic polarization at dielectric interfaces have attracted significant renewed attention [13, 24, 25, 26, 2, 14]. These methods essentially seek direct numerical solutions to the Poisson's equation that converge rapidly and accurately.

At an arbitrary location in the domain $V \in \mathbb{R}^3$, the electric filed $\mathbf{E}$ satisfies the differential form of Gauss's law [27],

$$(1.1) \qquad \nabla \cdot \mathbf{E}(\mathbf{r}) = \frac{\rho(\mathbf{r})}{\epsilon_0} ,$$

and—if no time-dependent magnetic field is present—Faraday's law,

$$(1.2) \qquad \nabla \times \mathbf{E}(\mathbf{r}) = \mathbf{0} ,$$

where $\rho(\mathbf{r})$ is the total charge density and ϵ_0 the vacuum permittivity. From the Helmholtz decomposition,

$$(1.3) \qquad \mathbf{E}(\mathbf{r}) = -\nabla \Phi(\mathbf{r}) ,$$

we arrive at Poisson's equation for the electrostatic potential $\Phi(\mathbf{r})$,

$$(1.4) \qquad -\nabla^2 \Phi(\mathbf{r}) = \frac{\rho(\mathbf{r})}{\epsilon_0} \; .$$

For convenience, we define the linear operator $\mathcal{G} = -\nabla^{-2}$, so that the solution of Eq. (1.4) can be represented as

$$(1.5) \qquad \Phi(\mathbf{r}) = \frac{\mathcal{G}\rho(\mathbf{r})}{\epsilon_0} = \int_V G_0(\mathbf{r}, \mathbf{r}')\rho(\mathbf{r}')d\mathbf{r}' \; ,$$

where G_0 is the Green's function for Eq. (1.4), satisfying

$$(1.6) \qquad -\nabla^2 G_0(\mathbf{r}, \mathbf{r}') = \delta(\mathbf{r} - \mathbf{r}') \; .$$

For free-space boundary conditions, $G_0 = 1/(4\pi\epsilon_0 |\mathbf{r} - \mathbf{r}'|)$ is simply the Coulomb potential due to a unit source charge, whereas for periodic boundary conditions G_0 can be treated via the Ewald summation. Combining Eq. (1.3) and Eq. (1.5) we can represent the electric field as

$$(1.7) \qquad \mathbf{E}(\mathbf{r}) = -\nabla \frac{\mathcal{G}\rho(\mathbf{r})}{\epsilon_0} \; .$$

We restrict ourselves to systems comprised of objects with linear and isotropic dielectric response, i.e., characterized by a spatially varying dielectric constant $\epsilon(\mathbf{r})$ or, equivalently, a local electric susceptibility $\chi(\mathbf{r}) = \epsilon(\mathbf{r})/\epsilon_0 - 1$. The local polarization field $\mathbf{P}$ induced by the electric field $\mathbf{E}$ is then given by the constitutive relation

$$(1.8) \qquad \mathbf{P}(\mathbf{r}) = \epsilon_0 \chi(\mathbf{r})\mathbf{E}(\mathbf{r}) \; .$$

As a result, the polarization charge associated with the polarization field reads

(1.9)
$$\rho_{pol}(\mathbf{r}) = -\nabla \cdot \mathbf{P}(\mathbf{r}) = -\nabla \cdot [\epsilon_0 \chi(\mathbf{r})\mathbf{E}(\mathbf{r})] \ .$$

Note that the total charge density ρ at location $\mathbf{r}$ consists of both free charge density and polarization charge density (also referred to as bound charge density),

(1.10)
$$\rho(\mathbf{r}) = \rho_f(\mathbf{r}) + \rho_{pol}(\mathbf{r}) \ .$$

In simulations of dielectric objects, $\rho_f(\mathbf{r})$ is specified by the particle configuration, whereas the efficient calculation of $\rho_{pol}(\mathbf{r})$ is our primary objective. In the following, I discuss how to construct a linear operator equation for the bound charge density.

Substitution of Eq. (1.3) into Eq. (1.9) yields

(1.11)
$$\rho_{pol}(\mathbf{r}) = \epsilon_0 \nabla \cdot [\chi(\mathbf{r})\nabla\Phi(\mathbf{r})]$$
$$= \epsilon_0 \chi(\mathbf{r})\nabla^2\Phi(\mathbf{r}) + \epsilon_0 \nabla\chi(\mathbf{r}) \cdot \nabla\Phi(\mathbf{r}) \ .$$

This implies that polarization charge may arise in two ways, namely nonzero divergence of the electric field, which corresponds to locations of free charge, and spatial variation of the electric susceptibility. The first term on the right-hand side of Eq. (1.11) can be reduced to $-\chi(\mathbf{r})\rho(\mathbf{r})$ with Eq. (1.4) and the second term can be rewritten as $-\nabla\epsilon(\mathbf{r}) \cdot \mathbf{E}(\mathbf{r})$. Applying Eq. (1.10), we obtain

(1.12)
$$\frac{\epsilon(\mathbf{r})}{\epsilon_0}[\rho_f(\mathbf{r}) + \rho_{pol}(\mathbf{r})] + \nabla\epsilon(\mathbf{r}) \cdot \mathbf{E}(\mathbf{r}) = \rho_f(\mathbf{r}) \ ,$$

which can be simplified via Eq. (1.1) to

$$(1.13) \qquad\qquad \nabla \cdot \epsilon(\mathbf{r})\mathbf{E}(\mathbf{r}) = \rho_{\mathrm{f}}(\mathbf{r}) \ .$$

Here we have two choices for substituting the electric field $\mathbf{E}$. One choice is to substitute Eq. (1.3), resulting in an alternative form of Poisson's equation,

$$(1.14) \qquad\qquad -\nabla \cdot \epsilon(\mathbf{r})\nabla\Phi(\mathbf{r}) = \rho_{\mathrm{f}}(\mathbf{r}) \ .$$

This formulation differs from Eq. (1.4) in two ways: The source term of this equation is simply the *free* charge density ρ_{f}, thus there is no need to solve for ρ_{pol}. In exchange, the position-dependent dielectric constant leads to a Green's function $\widetilde{G}$ that is no longer in simple Coulomb form like G_0. Instead, it satisfies

$$(1.15) \qquad\qquad -\nabla \cdot \epsilon(\mathbf{r})\nabla\widetilde{G}(\mathbf{r}, \mathbf{r}') = \delta(\mathbf{r} - \mathbf{r}') \ .$$

Thus, the solution for Eq. (1.14) can be represented as

$$(1.16) \qquad\qquad \Phi(\mathbf{r}) = \int_V \widetilde{G}(\mathbf{r}, \mathbf{r}')\rho_{\mathrm{f}}(\mathbf{r}')d\mathbf{r}' \ .$$

Here $\widetilde{G}$ in the exterior region (i.e., the region outside the dielectric objects, with relative permittivity ϵ_{m}) is a sum of two parts,

$$(1.17) \qquad\qquad \widetilde{G}(\mathbf{r}, \mathbf{r}') = \widetilde{G}_{\mathrm{Coul}}(\mathbf{r}, \mathbf{r}') + \widetilde{G}_{\mathrm{pol}}(\mathbf{r}, \mathbf{r}') \ ,$$

where $\widetilde{G}_{\mathrm{Coul}}(\mathbf{r}, \mathbf{r}') = G_0(\mathbf{r}, \mathbf{r}')/\epsilon_{\mathrm{m}}$ is the the Coulomb potential of a unit charge in a dielectric medium with permittivity ϵ_{m} and the polarization potential $\widetilde{G}_{\mathrm{pol}}(\mathbf{r}, \mathbf{r}')$ satisfies

the Laplace equation,

$$(1.18) \qquad\qquad \nabla^2 \widetilde{G}_{\mathrm{pol}}(\mathbf{r}, \mathbf{r}') = 0 \ .$$

Obviously, the difficulty in solving Eq. (1.14) lies in obtaining $\widetilde{G}_{\mathrm{pol}}$. For simple geometries, it is possible to represent $\widetilde{G}_{\mathrm{pol}}$ via image-charges, see Section 2.3.

On the other hand, Eq. (1.13) can be viewed as an integral equation. We substitute Eq. (1.7) and define the operator

$$(1.19) \qquad\qquad \mathcal{A} = -\nabla \cdot \frac{\epsilon(\mathbf{r})}{\epsilon_0} \nabla \mathcal{G}$$

to arrive at a linear equation linking the polarization charge density and the free charge density,

$$(1.20) \qquad\qquad \mathcal{A}\rho_{\mathrm{pol}} = b \ ,$$

with

$$(1.21) \qquad\qquad b = (1 - \mathcal{A})\rho_{\mathrm{f}} \ ,$$

where I have separated the bound charge from the free charge. Equation (1.20) is applicable to general electrostatic problems in any isotropic and linear dielectric continuum, i.e., $\epsilon(\mathbf{r})$ can be any spatially varying function. However, its numerical solution requires discretization of the entire domain. The computational cost can be greatly reduced by exploiting the observation that for many physical systems the dielectric constant varies rapidly only at the interfaces between media. This justifies the approximation to confine

ourselves to systems with sharp dielectric interfaces, where $\nabla\epsilon(\mathbf{r})$ is non-zero only at the interfaces. This leads to the *boundary-element method* (BEM) approach that has been proposed in various forms [28, 29, 30, 31, 32, 33, 34, 35, 2]. The BEM offers the advantage that arbitrary geometries can be handled with relative ease. Moreover, the BEM facilitates the treatment of periodic geometries commonly employed in electrostatics problems.

Since the BEM offers a completely different approach than the image-charge method, in Chapter 2, I compare two recently proposed algorithms in each field, namely the iterative dielectric solver (IDS) [2] and the generalized image-charge method [36], in details for a spherical colloidal system. The flexibility of the BEM in geometries enables us to answer non-trivial interfacial problems, such as the electrolyte distribution near structured dielectric interfaces (see Chapter 3). Despite the success of the original IDS, when applied to anisotropic particles, Janus colloids for example, its accuracy is suboptimal. I address this challenge in Chapter 4 via the Jacobi preconditioner. This improved algorithm helps us to understand the electrolyte structure near patchy colloids in Chapter 5. Since the IDS is essentially based on the Neumann boundary condition, it is not applicable to equipotential surfaces, such as electrodes kept at constant potentials, despite their wide appearance in nano-devices. In Chapter 6, I demonstrate that the IDS can be extended to treat such Dirichlet boundary problems as well, and even problems with mix boundary conditions, while maintaining its computational efficiency. I also propose a volume-element method (VEM) that can handle systems with spatially varying permittivities. The dielectric effects that affect the electrolyte distribution near surfaces also have important consequences for the surface tension. A study on the excess surface tension of asymmetric electrolytes at dielectric interfaces is presented in Chapter 7.

CHAPTER 2

Comparison of the iterative dielectric solver (IDS) and the generalized image-charge method

This chapter represents a close comparison of the boundary-element method and the generalized image-charge method. To present a complete story, I have included some of the image-charge method derivations by Zecheng Gan and Zhenli Xu. The content of this chapter is based on the following publication:

- Zecheng Gan[*], Huanxin Wu[*], Kipton Barros, Zhenli Xu, and Erik Luijten, Comparison of efficient technique for the simulation of dielectric objects in electrolytes, *J. Comp. Phys.* **291**, 317–333 (2015)

2.1. Introduction

The relevance of polarization problems in wide areas of science makes it pressing to perform a quantitative comparison of the *boundary-element method* (BEM) and *image-charge method* (ICM) in terms of accuracy, efficiency, and performance. Starting from the Poisson's equation, the BEM solves its boundary integral form, while the ICM originates from its harmonic series solution. In certain cases, it is possible to avoid the evaluation of harmonic series via an image-charge representation of the closed-form Green's functions [37, 38, 39, 40, 41]. Recently, this ICM has been extended to the treatment of multiple spheres via recursive reflections [36]. This approach not only provides a fast

---

[*]Z. Gan and H. Wu contributed equally to this paper

approximation to the Green's function, but also can be easily accelerated by well-known algorithms, because the approximation is a sum of Coulomb potentials.

Here, two recently developed adaptations of both approaches are investigated in detail. The BEM for general mobile dielectric objects was proposed and implemented in Refs. [2, 14] for molecular dynamics (MD) simulations. It is now named the *iterative dielectric solver* (IDS). The ICM for multiple spheres was presented in Ref. [36]; there my collaborators present its first implementation within a Monte Carlo (MC) simulation. For the IDS, surface bound charge is obtained from the solution of a dense linear system via the generalized minimum residual (GMRES) method [42], using a formulation that is particularly well conditioned [43, 2]. Moreover, the matrix–vector product required in each GMRES iteration is accelerated by a fast Ewald solver, in the IDS the particle–particle particle–mesh (PPPM) method [44, 45] (but note that the IDS is independent of the choice of the solver). This combination of techniques yields a near-linear scaling calculation in the number of discrete boundary elements. For the ICM, the single-sphere image-charge formula is applied recursively using reflections between spheres. The singular or nearly singular quadrature problem for the image line charge integral has been well approximated. The image-charge number is chosen to achieve a specified accuracy at minimal cost. Thus, a set of image charges is constructed that represents the polarization potential. The Barnes–Hut octree algorithm [46, 47, 48] is used to efficiently calculate the interaction of a source charge with other charges, in a manner tailored for the single-particle displacements employed in MC simulations [49].

To illustrate these algorithm properties, I present results for a representative problem, namely the ensemble-averaged mean force between a pair of colloidal particles immersed

in an electrolyte. The mean force is typically employed to investigate the effective interactions between colloids (although typically without taking into account dielectric effects), and has attracted significant interest in recent years [50, 51, 52, 53, 54, 55, 56], due to its fundamental importance in colloidal science. I demonstrate how the simulations can decompose the total mean force into contributions arising from ion–polarization interactions, interactions between bound charges, and entropic effects.

This chapter is organized as follows. I first rederive the formulations of the IDS and ICM in Sec. 2.2 and 2.3, respectively. Then, their computational complexity is compared in Sec. 2.4, followed by tests of the accuracy and parameter choices of both algorithms in Sec. 2.5. In Sec. 2.6, I present a practical illustration in the form of MD and MC simulation results for the induced mean force between dielectric colloidal spheres. I conclude with a summary in Sec. 2.7.

2.2. Iterative dielectric solver

Here I summarize the key ideas of the IDS [2]. Consider a model system consisting of $\mathcal{P}$ uniform dielectric objects $\mathcal{S}_i$ ($1 \leq i \leq \mathcal{P}$), embedded in a dielectric continuum. We assume that all objects are neither touching nor intersecting each other, i.e., $\mathcal{S}_i \bigcap \mathcal{S}_j = \varnothing$. The domain V can then be divided into an interior region $\Omega = \bigcup_{i=1}^{\mathcal{P}} \mathcal{S}_i$ and an exterior region $V \backslash \Omega$. Any free charge *within* Ω is replaced with free charge density σ_f at the object surfaces that produces the equivalent electric field in the exterior region (cf. [2, Sec. IV.I]). In addition, there is a bulk free charge density $\rho_\mathrm{f}(\mathbf{r})$ in the exterior region. The dielectric constant $\epsilon(\mathbf{r})$ is set to be piecewise constant, with discontinuities only at

the object interfaces,

$$(2.1) \qquad \epsilon(\mathbf{r}) = \begin{cases} \epsilon_0 \epsilon_i & \mathbf{r} \in \mathcal{S}_i, \\ \epsilon_0 \epsilon_{\mathrm{m}} & \mathbf{r} \in (V \backslash \Omega) \end{cases} ,$$

where ϵ_i and ϵ_{m} are the relative permittivities of object i and the embedding medium, respectively. The polarization charge density $\rho_{\mathrm{pol}}(\mathbf{r})$ due to variation of the dielectric constant is then only present on the object surfaces and reduces to the surface bound charge density $\sigma_{\mathrm{pol}}(\mathbf{r})$.

To obtain a linear operator equation for $\sigma_{\mathrm{pol}}(\mathbf{r})$ analogous to Eq. (1.20), we first recall the standard boundary condition for the electric displacement field at any point $\mathbf{r}$ on the object surfaces, as implied by Eq. (1.13),

$$(2.2) \qquad \epsilon_0 \left[\epsilon_{\mathrm{m}} \mathbf{E}_{\mathrm{out}}(\mathbf{r}) - \epsilon_i \mathbf{E}_{\mathrm{in}}(\mathbf{r}) \right] \cdot \hat{\mathbf{n}} = \sigma_{\mathrm{f}}(\mathbf{r}) ,$$

where $\mathbf{E}_{\mathrm{in}}(\mathbf{r})$ and $\mathbf{E}_{\mathrm{out}}(\mathbf{r})$ are the electric field inside and outside the surface at point $\mathbf{r}$, respectively, and $\hat{\mathbf{n}}$ is the outward unit normal to the surface at $\mathbf{r}$. Likewise, Eq. (1.1) implies

$$(2.3) \qquad \epsilon_0 \left[\mathbf{E}_{\mathrm{out}}(\mathbf{r}) - \mathbf{E}_{\mathrm{in}}(\mathbf{r}) \right] \cdot \hat{\mathbf{n}} = \sigma_{\mathrm{f}}(\mathbf{r}) + \sigma_{\mathrm{pol}}(\mathbf{r}) .$$

Combining Eq. (2.2) and Eq. (2.3) and defining the electric field at the surface as $\mathbf{E}(\mathbf{r}) = \left[\mathbf{E}_{\mathrm{in}}(\mathbf{r}) + \mathbf{E}_{\mathrm{out}}(\mathbf{r}) \right]/2$, we obtain

$$(2.4) \qquad \bar{\epsilon}_i \left[\sigma_{\mathrm{f}}(\mathbf{r}) + \sigma_{\mathrm{pol}}(\mathbf{r}) \right] + \epsilon_0 \Delta \epsilon_i \mathbf{E}(\mathbf{r}) \cdot \hat{\mathbf{n}} = \sigma_{\mathrm{f}}(\mathbf{r}) ,$$

where $\bar{\epsilon}_i = (\epsilon_i + \epsilon_{\mathrm{m}})/2$ and $\Delta\epsilon_i = \epsilon_{\mathrm{m}} - \epsilon_i$. This has the same form as Eq. (1.12), except that it avoids the factor $\nabla\epsilon(\mathbf{r})$ which is ill-defined at the interface. Observe how free charge not located on the object surfaces enter this equation through the electric field $\mathbf{E}$. Finally, Eq. (2.4) is expressed in a linear form equivalent to Eq. (1.20),

$$(2.5) \qquad \mathcal{A}_{\mathrm{s}}\sigma_{\mathrm{pol}} = b_{\mathrm{s}} \ ,$$

where

$$(2.6) \qquad \mathcal{A}_{\mathrm{s}}\sigma_{\mathrm{pol}} \equiv \bar{\epsilon}_i\sigma_{\mathrm{pol}} + \epsilon_0\Delta\epsilon_i\mathbf{E}_{\mathrm{pol}} \cdot \hat{\mathbf{n}} \ ,$$

with

$$(2.7) \qquad \mathbf{E}_{\mathrm{pol}}(\mathbf{r}) = \sum_{i=1}^{\mathcal{P}} \int_{\partial \mathcal{S}_i} \frac{\sigma_{\mathrm{pol}}(\mathbf{s}')(\mathbf{r} - \mathbf{s}')}{4\pi\epsilon_0|\mathbf{r} - \mathbf{s}'|^3} d\mathbf{s}'$$

the polarization field from all surface polarization charge at $\mathbf{s}' \neq \mathbf{r}$ and

$$(2.8) \qquad b_{\mathrm{s}} = (1 - \bar{\epsilon}_i)\sigma_{\mathrm{f}} - \epsilon_0\Delta\epsilon_i\mathbf{E}_{\mathrm{f}} \cdot \hat{\mathbf{n}} \ ,$$

with

$$(2.9) \qquad \mathbf{E}_{\mathrm{f}}(\mathbf{r}) = \sum_{i=1}^{\mathcal{P}} \int_{\partial \mathcal{S}_i} \frac{\sigma_{\mathrm{f}}(\mathbf{s}')(\mathbf{r} - \mathbf{s}')}{4\pi\epsilon_0|\mathbf{r} - \mathbf{s}'|^3} d\mathbf{s}' + \int_{V\backslash\Omega} \frac{\rho_{\mathrm{f}}(\mathbf{r}')(\mathbf{r} - \mathbf{r}')}{4\pi\epsilon_0\epsilon_{\mathrm{m}}|\mathbf{r} - \mathbf{r}'|^3} d\mathbf{r}' \ .$$

The first term on the right-hand side of Eq. (2.9) represents the contribution from all surface charges at $\mathbf{s}' \neq \mathbf{r}$ and the second term originates from all free charge not at the surfaces (i.e., located in the embedding medium). The fields $\mathbf{E}_{\mathrm{pol}}$ and $\mathbf{E}_{\mathrm{f}}$ are evaluated at each surface point.

To solve Eq. (2.5) numerically, the IDS discretizes the interfaces into M finite boundary elements and transforms it into a matrix equation. Since $\mathcal{A}_\mathrm{s}$ has been shown to be well-conditioned [43, 2], this method of finding the polarization charge distribution is more suitable than alternative approaches. Direct solution of the matrix form of Eq. (2.5) requires costly $[\mathcal{O}(M^3)]$ matrix inversion. This inversion needs to be repeated whenever the dielectric geometry changes—e.g., in each time step in a MD simulation of dielectric objects—and even for static dielectric geometries the solution involves dense matrix–vector multiplication at cost $\mathcal{O}(M^2)$. A far more efficient technique is the use of an iterative solver, for which the IDS select GMRES [42]. GMRES only involves matrix–vector products, and aims to minimize the norm of the residual of Eq. (2.5),

(2.10)
$$r = b_\mathrm{s} - \mathcal{A}_\mathrm{s}\sigma_\mathrm{pol}$$
$$= \sigma_\mathrm{f} - \bar{\epsilon}(\sigma_\mathrm{f} + \sigma_\mathrm{pol}) - \epsilon_0\Delta\epsilon_i(\mathbf{E}_\mathrm{f} + \mathbf{E}_\mathrm{pol}) \cdot \hat{\mathbf{n}} \;,$$

where $\mathbf{E}_\mathrm{f} + \mathbf{E}_\mathrm{pol}$ is the *total* electric field at each surface patch, which can be computed directly with a fast Ewald solver. Thus, for a system containing M boundary elements and N isolated free charges, the residual can be obtained at a cost $\mathcal{O}((M+N)\log(M+N))$ for PPPM [44, 45] or even $\mathcal{O}(M+N)$ for the fast multipole method (FMM) [57, 58, 59, 60]. In practical MD simulations, once convergence has been attained in the first time step, subsequent time steps require less than 4 iterations to obtain the surface charge density with a relative error smaller than 10^{-4} [2, 14]. An additional advantage of computing the electric field via Ewald summation is that periodic images are automatically taken into account, as is customary for simulations of electrostatic systems in bulk geometries.

I note that several additional considerations affect the accuracy and convergence rate. For boundary elements of finite size and nonzero curvature, surface charge within an element contributes to the normal component of the electric field and thus to the polarization charge. To first approximation, this has been taken into account via a "curvature correction." The IDS approximates the correction term by assuming disk shaped patches with mean curvature, which works well for the spherical colloidal system in this chapter [61, 31]. Higher-order corrections can be applied as well [2, Sec. IV.B]. More sophisticated treatments via numerical quadrature are discussed in Refs. [62, 43, 63]. An alternative approach is the so-called "qualocation" method (cf. Sec. 4.1), which has been found to yield similar accuracy [64]. The IDS further improves the convergence rate by constraining the net charge on dielectric objects per Gauss's law [2, Sec. IV.H].

2.3. Image-charge method

If all $\mathcal{P}$ dielectric objects $\mathcal{S}_i$ are of spherical shape, then an alternative method to the BEM is the ICM. We start with a single dielectric sphere (i.e., $\mathcal{P} = 1$) of radius a and relative permittivity ϵ_1 with background permittivity ϵ_m. By using spherical harmonics [65, 66] (also known as the Kirkwood series) and by using the ICM [38], the polarization potential of a unit source charge located at $\mathbf{r}_\mathrm{s}$ at any position $\mathbf{r}$ outside the sphere can be written as the sum of contributions from a Kelvin image $q_\mathrm{K} = -\frac{\epsilon_1 - \epsilon_\mathrm{m}}{\epsilon_1 + \epsilon_\mathrm{m}} a/r_\mathrm{s}$ inside the sphere at the inversion point $\mathbf{r}_\mathrm{K} = \mathbf{r}_\mathrm{s} a^2/r_\mathrm{s}^2$ and a line image charge distributed along $\mathbf{x} = x\mathbf{r}_\mathrm{s}/r_\mathrm{s}$ with $x \in [0, r_\mathrm{K}]$. $(L-1)$-point Gauss–Legendre quadrature can be used to approximate the line charge potential [67], resulting a total of L image charges for the polarization potential.
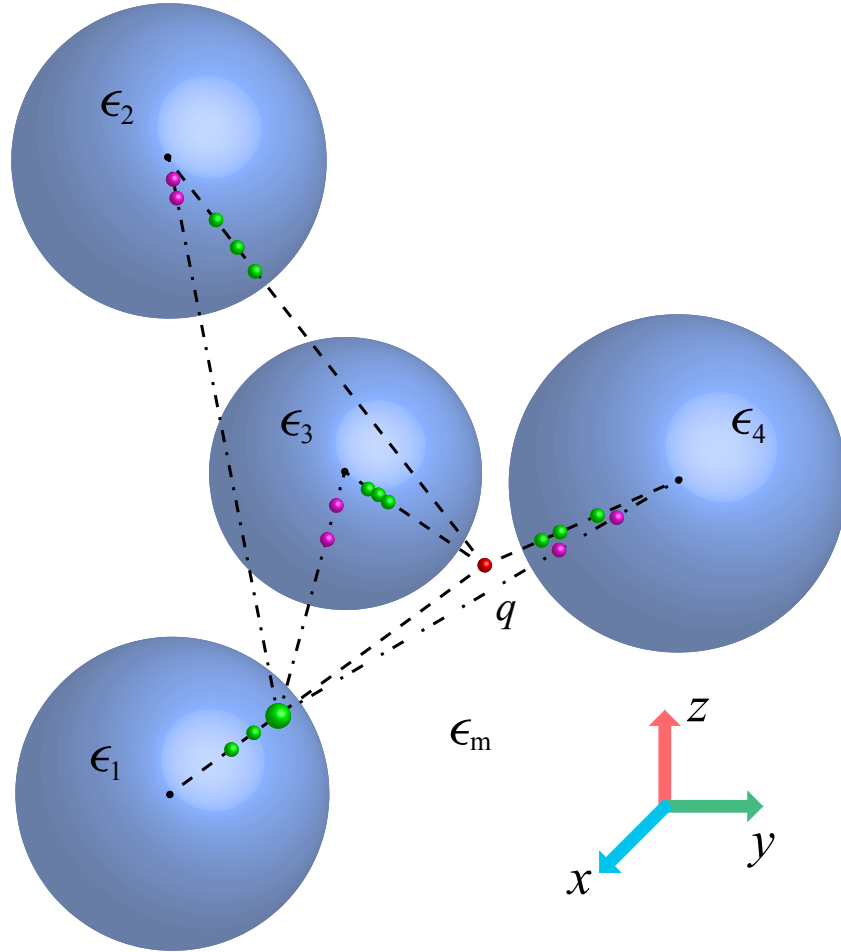
Figure 2.1. Construction of image charges by reflections between dielectric spheres (blue). A source charge q located in the exterior region induces L_1 first-level image charges (green spheres, here $L_1 = 3$) inside each sphere. Subsequently, each first-level image induces L_2 second-level images inside all other spheres. In this example $L_2 = 2$ and only the images for the enlarged first-level image are shown (purple spheres). This reflection procedure is performed recursively until convergence is reached.

When $\mathcal{P} > 1$, the polarization potential can be contructed by a procedure of iterative image charge reflections [68, 36], as illustrated in Fig. 2.1. If a unit charge is located at $\mathbf{r}_s$ in the exterior region, then L_1 image charges are produced in each sphere. To

include the contribution from the image charges at other spheres, L_2 additional (second-level) image charges are generated in $\mathcal{P}_j (j \neq i)$ for each of the L_1 image charges in $\mathcal{P}_i$. Recursive iteration of this procedure yields the polarization potential [36]. If we estimate the polarization potential at reflection level R, the number of image charges $\mathcal{I}$ is

$$(2.11) \qquad \mathcal{I} = \mathcal{P} \sum_{i=1}^{R} \left[(\mathcal{P} - 1)^{i-1} \prod_{j=1}^{i} L_j \right] .$$

Thus $\mathcal{I}$ increases exponentially with R. Fortunately, the truncation error decreases rapidly. Moreover, analysis of the quadrature error shows that for higher reflection levels $i > 1$, L_i may be reduced without loss of accuracy [69]. Finally, since the polarization energy now is comprised of Coulombic interactions between image and source charges, it can be evaluated via fast algorithms such as the FMM [57, 58, 59, 60] or treecode algorithms [46, 47, 48].

Although the ICM avoids the need to calculate surface bound charge, it can be obtained directly once the electrostatic potential in the exterior region $\Phi_{\mathrm{out}}(\mathbf{r})$ or the electric field has been computed from the free and image charges. This explicit evaluation is useful, e.g., for comparison with the IDS. If $\mathbf{E}_{\mathrm{out}}(\mathbf{r})$ denotes the electric field in the exterior region (relative permittivity ϵ_{m}), then the normal component of this field at position $\mathbf{r}$ on an interface with a dielectric object (relative permittivity ϵ_{in}) is

$$(2.12) \qquad \mathbf{E}_{\mathrm{out}}(\mathbf{r}) \cdot \hat{\mathbf{n}} = -\frac{\partial \Phi_{\mathrm{out}}(\mathbf{r})}{\partial n} ,$$

where $\hat{\mathbf{n}}$ is the outward normal. The normal component of the *interior* electric field in the dielectric, at the same surface position, then follows from Eq. (2.2) and can be substituted

in Eq. (2.3) to obtain the bound charge density

$$(2.13) \qquad \sigma_{\mathrm{pol}}(\mathbf{r}) = \frac{1}{\epsilon_{\mathrm{in}}} \left[(\epsilon_{\mathrm{in}} - \epsilon_{\mathrm{m}}) \epsilon_0 \mathbf{E}_{\mathrm{out}}(\mathbf{r}) \cdot \hat{\mathbf{n}} - (\epsilon_{\mathrm{in}} - 1) \sigma_{\mathrm{f}}(\mathbf{r}) \right] \ .$$

I illustrate this with a practical example in Sec. 2.5.3.

2.4. Efficiency comparison

To compare the computational complexity of both methods, I consider geometries that are amenable to both approaches, e.g., configurations of spheres. Even though the efficiency will depend on implementation and also on the physical system considered, general observations can be made. Specifically, the computational cost of both methods is dominated by the electrostatic solver and hence determined by the total number of charges that contribute to the electrostatic potential.

Consider a system of N free point charges placed outside $\mathcal{P}$ neutral spherical dielectric objects. In the IDS, if a total of M surface elements are required to achieve a certain accuracy, the total number of charges is $N+M$. For the PPPM method employed in [2, 14], the computational cost of a single time step is thus $\mathcal{O}((N + M)\log(N + M))$, although (as noted in [2]) the FMM may be better suited to the nonuniform distributions typical of the IDS. For dielectric systems containing objects of similar size, $M \propto \mathcal{P}$, so that the IDS has a nearly linear dependence on both the number of source charges N and the number of dielectric object $\mathcal{P}$. It must be noted, however, that M may have to be increased if point charges approach a dielectric interface very closely, or if multiple dielectric objects aggregate. In addition, I remark that in each time step GMRES typically requires 4 evaluations of the electrostatic potential to reach convergence.

For the ICM, the same system consists of N source charges and $N\mathcal{I}$ image charges. In the Barnes–Hut octree algorithm [46, 47, 48], the computational complexity of an MC cycle scales as $\mathcal{O}(N\mathcal{I}\log(N\mathcal{I}))$ [70]. Not only does $\mathcal{I}$ increase as a power law of $\mathcal{P}$, cf. Eq. (2.11), it also is comparable in magnitude to M (See Sec. 2.5.2). However, whereas for the IDS it appears additive to N in the computational cost, for the ICM it appears multiplicatively. Thus, for large N or $\mathcal{P}$, the IDS generally outperforms the ICM. An important advantage of the ICM, on the other hand, is that geometric singularities are naturally avoided, as it employs a closed-form expression for the Green's function. In addition, the number of image charges in the ICM does not depend on the colloidal size, making it advantageous for the simulation of large colloids. Moreover, the efficiency can be increased by dynamically tuning $\mathcal{I}$ based upon the geometry, e.g., when dielectric objects are spaced far apart or source charges are not close to an object. Also, since the image charges are distributed nonuniformly within the spheres, the computational cost can be reduced by decreasing the number of clusters in the Barnes–Hut octree algorithm.

If the dielectric objects have arbitrary (nonuniform) surface charge density, no additional computational expense is incurred in the IDS, as this charge can be distributed across the boundary patches. On the other hand, in the ICM this surface discretization is generally costly, as it increases the number of source charges. For immobile objects, the potential generated by these charges and their image charges is constant and can be precomputed within a simulation, but for dynamic dielectric objects this is not the case.

As a concrete comparison between the IDS and ICM I consider the system of two colloids immersed in an electrolyte, described in Sec. 2.6 below (all technical parameters are described there as well). I determine the time it takes to obtain an independent sample

for the net force on one of the colloids from the integrated autocorrelation time [71]. Using the IDS, this requires 120 MD time steps, corresponding to 45 seconds of CPU time (Intel Xeon E5-2620 v3, 2.40 GHz). When interpreting this time requirement, it is important to note that the system contains $N = 702$ ions as well as $M = 2944$ surface elements. On the other hand, in the ICM an independent sample is obtained after every 1000 MC cycles, where a cycle corresponds to one proposed move per ion (on average). For the parameter choice adopted in Sec. 2.6 ($\mathcal{I} = 310$ image charges, reflection level "5332" as described in Sec. 2.5.2) this corresponds to 50 seconds of CPU time, although this can be reduced to 40 seconds by choosing $\mathcal{I} = 248$ image charges (reflection level "4332") while retaining a sufficient precision, cf. Sec. 2.5.2. In comparing these numbers, it should be noted that the cylindrical simulation cell adopted for the ICM contains only 276 ions, 2.5 times less than the periodic cell employed in the IDS (the larger cell in the IDS is chosen to avoid artificial periodicity effects). A final practical point is that the net force follows directly in the MD simulation, whereas relatively costly numerical differentiation [Eq. (2.19)] is required in the MC simulation. Given the slow decorrelation of the system it is important to avoid performing this derivative unnecessarily often.

2.5. Numerical results: Static configurations

2.5.1. Model setup

To test the performance of these two algorithms, my collaborators and I apply them to a system of two dielectric colloids immersed in an electrolyte (Fig. 2.2). The solvent is treated implicitly as a dielectric continuum with relative permittivity ϵ_{m} and the colloids and ions are represented explicitly by spheres with a soft repulsive potential. The colloidal
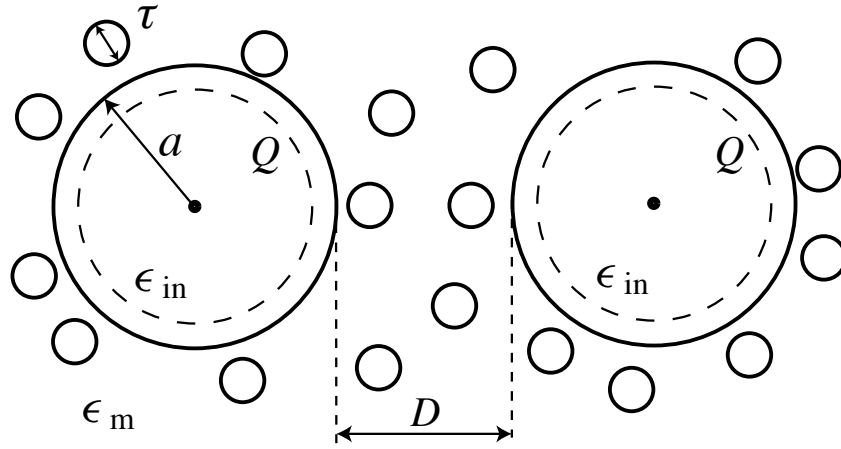
Figure 2.2. Two-dimensional illustration of the so-called primitive model of two dielectric colloids surrounded by an electrolyte.

particles ("macroions") have radius a and are placed at a surface-to-surface separation D. They both carry a total free charge $Q = Ze$ distributed uniformly on their surface and have an internal dielectric constant ϵ_{in}. The ions are of diameter τ with charge $q = ze$ and are considered non-polarizable, although their effective charge is reduced by a factor $1/\epsilon_m$ due to polarization of the surrounding medium.

The potential energy of the system V_{tot} can be expressed as a sum of three contributions

$$(2.14) \qquad\qquad V_{tot} = V_{LJ} + V_{Coul} + V_{pol} \,,$$

where V_{LJ} represents the non-electrostatic repulsions, V_{Coul} the pairwise electrostatic interactions between the free charges, and V_{pol} the polarization energy arising from the

interactions involving bound charges. The repulsive interaction between any two parti-cles i and j is modeled via a shifted-truncated Lennard-Jones (LJ) potential

$$(2.15) \qquad \beta u_{\mathrm{LJ}}(r_{ij}) = \begin{cases} \infty & \text{if } r_{ij} \leq \Delta_{ij} \\ 4\left[\left(\frac{c}{r_{ij}-\Delta_{ij}}\right)^{12} - \left(\frac{c}{r_{ij}-\Delta_{ij}}\right)^{6}\right] + 1 & \text{if } \Delta_{ij} < r_{ij} < \Delta_{ij} + 2^{\frac{1}{6}}c \\ 0 & \text{if } r_{ij} \geq \Delta_{ij} + 2^{\frac{1}{6}}c \end{cases} ,$$

where $\beta = 1/(k_{\mathrm{B}}T)$ is the inverse thermal energy (with k_{B} Boltzmann's constant and T the absolute temperature), r_{ij} the distance between the particle centers, and $\Delta_{ij} = (d_i + d_j)/2 - c$ the hard-core distance. Here, d_i and d_j are the diameters of particles i and j, respectively, and c is set to be the diameter of the mobile ions, $c = \tau$. Thus, at contact ($D = 0$, $r = 2a = d$) the two colloids have a repulsive Lennard-Jones interaction energy $u_{\mathrm{LJ}} = k_{\mathrm{B}}T$. To avoid the singularity that would arise if the position of an ion would coincide with a surface element, the surface elements are placed at the divergence of the sphere–ion shifted-truncated LJ potential, i.e., at a radius $a - \tau/2$.

The central force $F_{\mathrm{tot}}(D) = -\partial V_{\mathrm{tot}}/\partial D$ between the two colloids thus comprises two contributions

$$(2.16) \qquad\qquad\qquad F_{\mathrm{tot}}(D) = F_{\mathrm{LJ}}(D) + F_{\mathrm{ele}}(D) ,$$

where we only consider the component parallel to their center-to-center axis, and $F_{\mathrm{LJ}}(D)$ is the force originating from the LJ interactions and $F_{\mathrm{ele}}(D)$ the electrostatic force. Whereas the former is straightforward to obtain, the evaluation of $F_{\mathrm{ele}}(D)$ is nontrivial. As derived in [2] by differentiation of the total energy, the total electrostatic force on a rigid dielectric

object $\mathcal{S}_i$ is

$$(2.17) \qquad F_{\text{ele}}(D) = \int_{\mathcal{S}_i} f'(\mathbf{r}) d\mathbf{r} \;,$$

where $f'(\mathbf{r})$ is the parallel component of

$$(2.18) \qquad \mathbf{f}(\mathbf{r}) = \epsilon_{\text{m}} \left[\rho_{\text{f}}(\mathbf{r}) + \rho_{\text{pol}}(\mathbf{r}) \right] \mathbf{E}(\mathbf{r}) \;,$$

In the BEM-based calculations, I thus compute the total electrostatic force via summation over all boundary elements.

On the other hand, when using the ICM, my collaborators evaluate $F_{\text{ele}}(D)$ through numerical differentiation of the energy,

$$(2.19) \qquad F_{\text{ele}}(D) \approx -\frac{V_{\text{ele}}(D + \delta D) - V_{\text{ele}}(D)}{\delta D} \;.$$

For a given configuration, they first evaluate the total electrostatic energy $V_{\text{ele}} = V_{\text{Coul}} + V_{\text{pol}}$, and then displace one colloid by δD along the vector connecting the centers of the two colloids. Since this entails a change in $\epsilon(\mathbf{r})$, recalculation of V_{ele} requires the reconstruction of all image charges. For the system specified below, we choose $\delta D = 2 \times 10^{-5}$ Å.

In the numerical comparisons presented here, I set the solvent conditions to represent water at room temperature, i.e., $T = 298$ K and $\epsilon_{\text{m}} = 80$, resulting in a Bjerrum length $\ell_{\text{B}} = e^2/(4\pi\epsilon_0\epsilon_{\text{m}}k_{\text{B}}T) = 7.14$ Å. The colloids have dielectric constant $\epsilon_{\text{in}} = 2$ and diameter $d_{\text{M}} = 40$ Å. The electrolyte consists of $C_{\text{s}} = 100$ mM 2:2 salt (ion diameter $\tau = 4.5$ Å), which corresponds to a Debye length $\ell_{\text{D}} = \sqrt{\epsilon_0\epsilon_{\text{m}}k_{\text{B}}T/(8C_{\text{s}}e^2)} = 4.81$ Å. I focus on dielectric effects by choosing $Q = 0$ (or, equivalently, $\sigma_{\text{f}} = 0$), so that the electrostatic
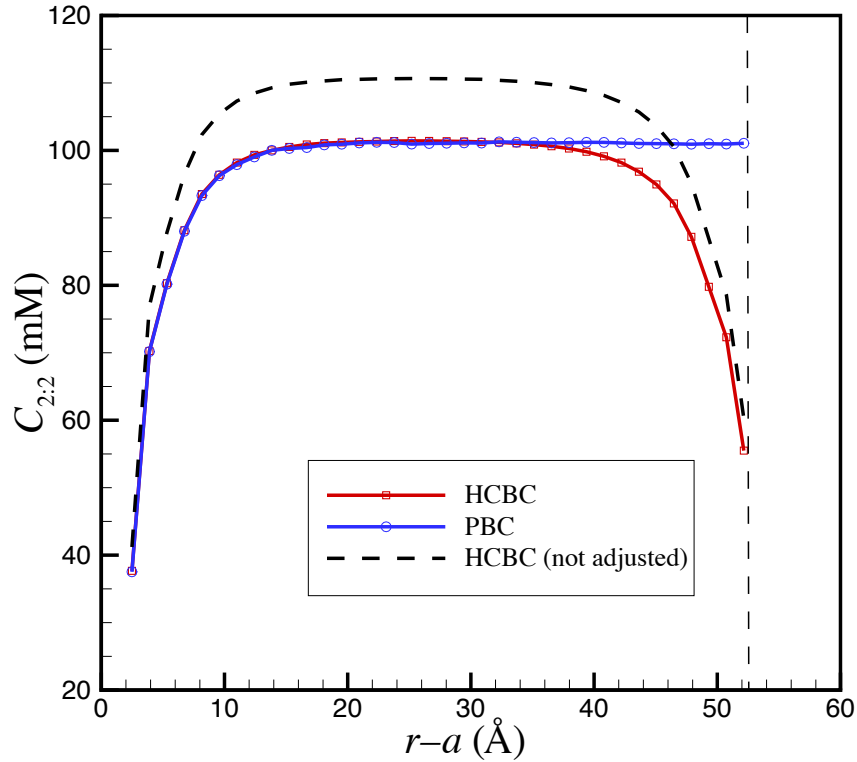
Figure 2.3. Comparison of the radial distribution of divalent ions around an isolated dielectric colloid (radius $a = 20$ Å) placed in a periodic box of linear size 180 Å ("PBC") and in a spherical cell (radius 72.65 Å) with hard-core boundary conditions ("HCBC"). Whereas the periodic box shows a constant salt concentration away from the colloidal surface, the system with the spherical hard wall exhibits significant depletion of salt near the wall (location marked by the dashed vertical line), which in turn gives rise to a spurious increase of the bulk concentration [indicated by the curve "HCBC (not adjusted)"]. To account for this effect, we adjust the number of ions such that both systems have the same effective bulk salt concentration (curve "HCBC").

force acting on the two colloids arises solely from the interactions of the polarization charge induced on either colloid with the salt ions and with the induced charge on the other colloid. I choose divalent salt, since the dielectric forces scale as z^2.

For calculations involving the ICM my collaborators employ a cylindrical cell [72], where the ions are confined by hard walls (both the cylindrical shell and its top and bottom), such that an ion acquires infinite energy if its center is moved outside of the cylinder. The colloids are fixed on the cylinder axis, while the mobile ions can move freely within the cylinder. The cylinder radius (65 Å) and length (190 Å) are chosen to be much larger than the Debye screening length. For the IDS I instead employ a cubic, periodically replicated box. In Sec. 2.5.2, I use configurations that are produced by the ICM, but for the comparison calculations performed with the IDS I place these configurations (which contain 300 ions) in a box of much larger volume (linear dimension 4500 Å) than the cylindrical cell, to suppress effects of the periodic boundary conditions. On the other hand, for the equilibrium results in Sec. 2.6 I find that the cylindrical volume suffers from significant boundary effects. Ions near the cylinder walls lack a symmetric shell of screening counterions, which in turns leads to a depletion of ions at the wall [73]. Figure 2.3 illustrates this effect for a spherical cell. If the number of ions is not adjusted to account for this effect, the concentration in the remainder of the cylinder will be significantly *increased*, hindering an accurate comparison with the IDS results. In the IDS I realize a salt concentration of 100 mM by placing 702 ions in a box of linear dimension 180 Å, which due to the excluded volume of the colloids results in an effective (bulk) concentration of ~101 mM. On the other hand, in the ICM one must reduce the number of ions from 300 to 276 to achieve the same concentration in the bulk, as confirmed in Fig. 2.3 for the spherical system. Whereas it also would have been possible to eliminate this effect via an attractive surface potential, I demonstrate in Sec. 2.6 that a proper bulk salt concentration surrounding the colloids is sufficient to reproduce the correct mean colloidal force.
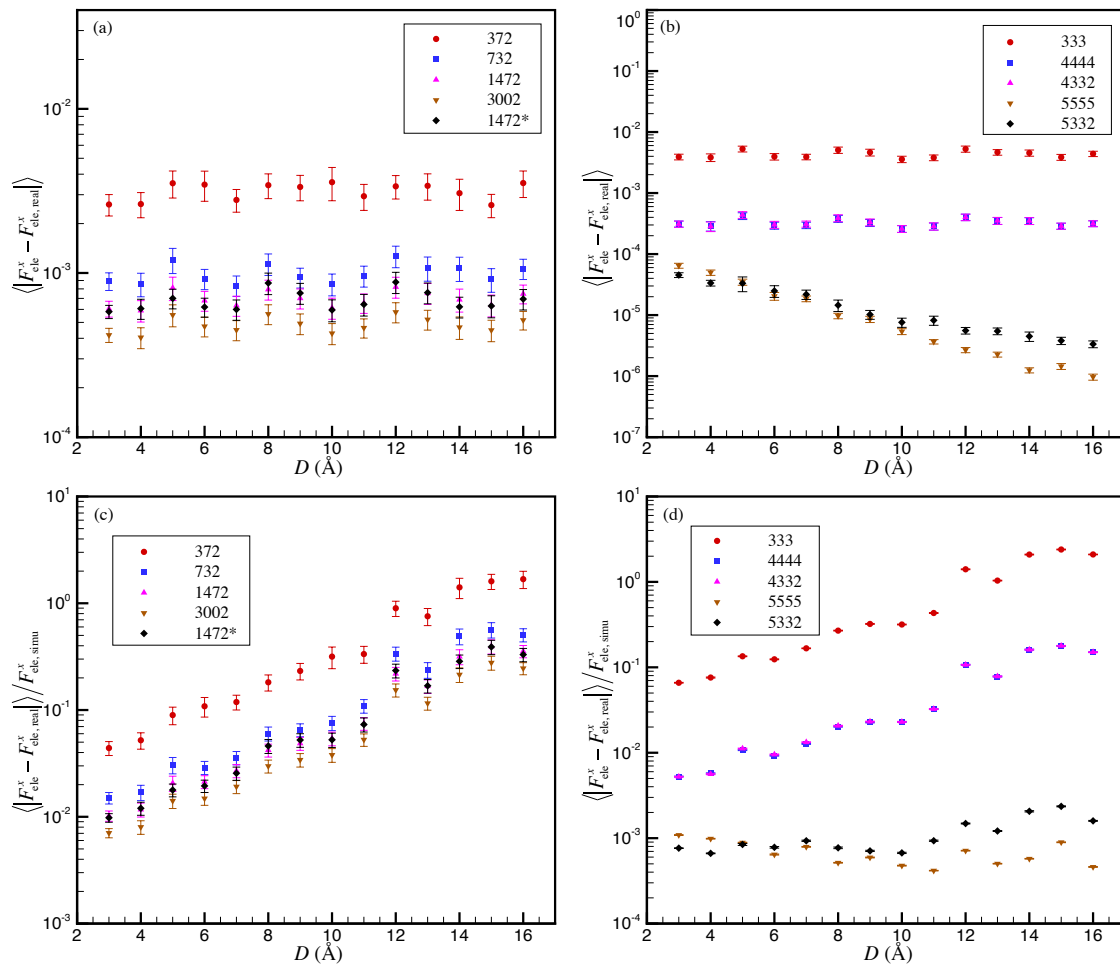
Figure 2.4. Accuracy of the electrostatic force between two neutral colloids immersed in an electrolyte, as a function of surface separation, $D = 3$–16 Å. Physical parameters are described in the main text. Panels (a) and (b) show the ensemble-averaged absolute error in the component of the absolute force along the center-to-center axis between the colloids for (a) the IDS at different surface discretizations (numbers in the key indicate the number of surface elements per sphere) and (b) the ICM at different reflection levels R and numbers of image charges L_i (numbers in the key indicate the number of image charges per reflection level). It is important to note that these estimates significantly *overestimate* the error obtained in a typical simulation, by averaging the absolute values of the deviations. Panels (c) and (d) show the same data as panels (a) and (b), respectively, but normalized by the magnitude of the force. The increase of these relative uncertainties with increasing D simply reflects the fact that the induced forces become very small at larger colloid separations. The exception to this trend are the ICM data [panel (d)] for the "5332" and "5555" parameters; here the relative deviation remains mostly flat since the effect of the decreasing force is partly negated by the decrease in the truncation error with increasing D [cf. panel (b)]. Force unit is $k_\mathrm{B}T/\ell_\mathrm{B}$. Ensemble averages are obtained from 100 independent equilibrium configurations, where the same set of configurations is employed for the IDS and ICM calculations.

2.5.2. Parameter dependence for the IDS and the ICM

We first examine the accuracy of both methods as a function of parameter choice (surface discretization for the IDS and number of images and level of reflection for the ICM). For each of 14 surface separations D (3–16 Å, in steps of 1 Å) we perform a simulation of the system described above (cylindrical cell, 300 ions) to produce 100 independent configurations corresponding to thermodynamic equilibrium. For each of these configurations, we then compute the force on one of the colloids using the ICM with $L = 5$, $R = 6$ and direct pairwise summation. These parameters yield an absolute accuracy of 10^{-7} and the results serve as the reference values.

Figure 2.4 shows, for each separation D, the absolute error in the force on a single colloid averaged over the 100 configurations as computed with the IDS and ICM for various parameter choices, along with the relative errors.

For the IDS I focus on the number of surface elements. Thus, I choose a sufficiently small convergence criterion for GMRES and high enough accuracy for the Ewald solver (relative error 10^{-4} for both GMRES and Ewald) to ensure that errors resulting from these two factors are small compared to the discretization error. As shown in Fig. 2.4(a), for systems with 372 to 3002 patches per colloid, the ensemble-averaged absolute errors in the forces are less than $0.003 k_\mathrm{B} T / \ell_\mathrm{B}$ for all 14 separations. Moreover, they decrease monotonically with increasing number of boundary elements, improving by an order of magnitude between the coarsest and the finest grids. We also investigate the role of the orientation of the surface grid [data labeled "1472*"]. Whereas all other grids are oriented such that for both colloids a grid point (center of a surface element) lies on their center-to-center axis, for "1472*" the grid is oriented such that this axis passes through the

edge of a surface element. The grid orientation can have a significant effect in individual configurations, depending on whether an ion resides close to a surface element, but I find that such differences vanish in the ensemble averages, as expected. In practical simulations (Sec. 2.6), I employ 1472 surface elements per colloid, which yields an absolute error less than $10^{-3} k_B T / \ell_B$. I note that the absolute deviations provide an upper bound for the systematic errors incurred in the simulations. Figure 2.4(c) shows the same data as panel (a), but normalized by the magnitude of the force. As this force becomes small when D increases, the relative deviations display an increasing trend.

Figures 2.4(b) and (d) show the absolute deviations in the force as well as the relative values of these errors for the same configurations as employed in panels (a) and (c), but now calculated by the ICM. To study the convergence of the polarization potential, my collaborators vary both the maximum reflection level R and the number of image charges L_i for each level. The different choices are labeled "$L_1 L_2 \cdots L_R$" and show a decrease in the absolute error by at least two orders of magnitude between "333" and "5555". Interestingly, the results in Fig. 2.4(b) show that the number of images at the higher reflection levels can be decreased without consequences for the accuracy, with excellent agreement between "4444" and "4332," and quite close agreement between "5555" and "5332". This approach can significantly reduce the computational cost. For example, "5332" requires $\mathfrak{I} = 310$ image charges per source charge (ion), five times less than "5555" ($\mathfrak{I} = 1560$). The decreasing error with increasing D in panel (b) arises from the decreasing truncation error.
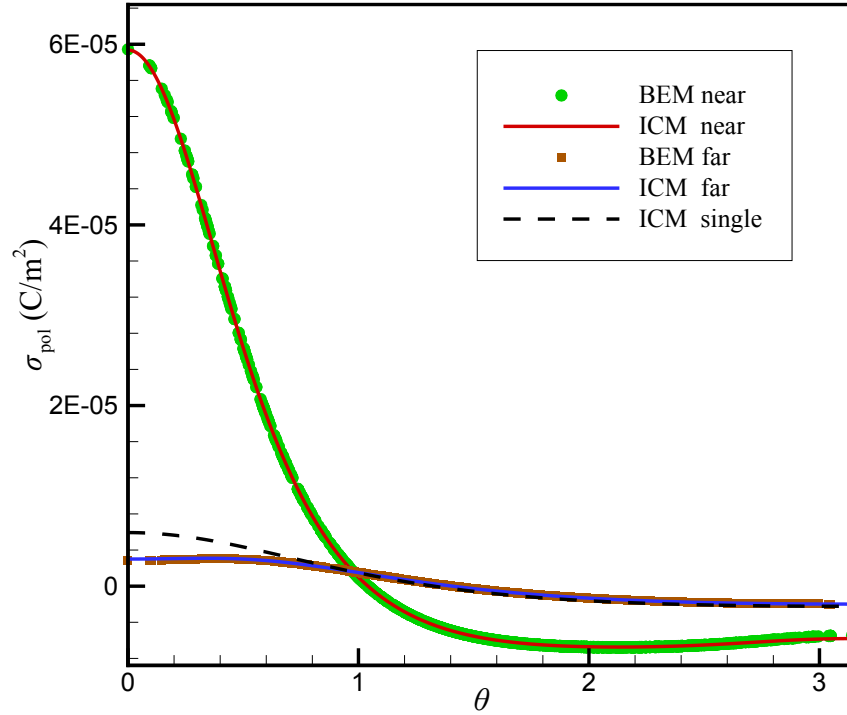
Figure 2.5. Comparison of the IDS and the ICM for the surface bound charge density σ_{pol} induced by a monovalent positive ion at $x = 60$ Å on two colloids ($\epsilon_{\mathrm{in}} = 2$) at $x = 21.5$ Å ("near") and $x = -21.5$ Å ("far") in water ($\epsilon_{\mathrm{m}} = 80$). The azimuthal symmetry makes it possible to parametrize σ_{pol} by the polar angle θ between the positive x-axis and the surface points. The results from both methods are in excellent agreement. The curve labeled "ICM single" represents the bound charge density on the "far" colloid in the absence of the intervening "near" colloid, illustrating the screening effect of the latter.

2.5.3. Induced surface charge density

It is instructive to compare the polarization charge as computed by the IDS and the ICM. We center the two spherical colloids at $(\pm 21.5, 0, 0)$Å (i.e., at a surface separation $D = 3$ Å), and place a single positive monovalent ion at $(60, 0, 0)$Å. Even this simple configuration is not easy to treat analytically, due to the interaction between polarization charges on different spheres. For both colloids, we determine σ_{pol} as a function of the polar angle θ. In the IDS, I use 1472 surface elements per colloid. For the ICM, my collaborators use "5555" [i.e., $R = 4$ and $L_i = 5$ $(i = 1, \ldots, 4)$] and exploit (2.13) to determine σ_{pol} for arbitrary θ. As shown in Fig. 2.5, the results obtained by both methods are in excellent agreement.

I note some interesting physical aspects of the induced polarization. Since the permittivity of the colloids ($\epsilon_{\mathrm{in}} = 2$) is lower than of the surrounding medium ($\epsilon_{\mathrm{m}} = 80$), positive bound charge accumulates near $\theta = 0$, i.e., the region facing the ion. This positive charge is then compensated by a gradually varying negative bound charge density over the rest of the colloidal surfaces, such that the neutrality condition is satisfied for the total bound charge on each colloid. In the IDS, I also constrain the net bound charge to be zero after each iteration to facilitate convergence and accuracy. In addition, σ_{pol} for the "far" sphere (positioned on the negative x-axis) has much lower bound charge density than the "near" sphere (positioned on the positive x-axis). This is not only due to its larger distance from the ion, but also due to the screening effect of the bound charges on the "near" sphere, which can be approximated as a dipole with its dipole moment pointing towards the positive source charge, partially canceling the source charge field. This is confirmed by the curve labeled "ICM single" in Fig. 2.5, which shows the surface bound charge density on

the sphere on the negative x-axis in the *absence* of the dielectric sphere on the positive x-axis. The induced charge density is then significantly higher, especially at small θ.

2.6. Numerical results: Thermodynamic equilibrium

Having verified the accuracy of both methods and the required parameter choices, I now proceed to evaluate their performance in practical simulations of thermodynamic properties. As a model system, I consider the ensemble-averaged force between two neutral dielectric colloids induced by a symmetric divalent aqueous electrolyte. As noted in Eq. (2.16), this force has two contributions: (i) the short-range excluded-volume repulsions that result in a depletion-type [74, 75] force that is ultimately entropic in nature and (ii) an electrostatic contribution involving polarization charges induced by ions. The ensemble-average of even the first contribution is not easily obtained by other means, given that the ionic arrangements are influenced by ion–ion interactions as well as ion–polarization interactions, where the polarization charges in turn are determined by the ionic configurations. For the second contribution, already the force in a single sample, Eq. (2.17) and Eq. (2.18), requires careful consideration.

For the IDS, I perform MD simulations that start from 702 ions randomly arranged around the two colloids. I employ the velocity Verlet algorithm with a Langevin thermostat (damping parameter time $20t_0$, where $t_0 = (m\tau^2\beta)^{1/2}$ is the LJ unit time with τ the ion diameter and m the ion mass). The RMS relative error of the PPPM method is chosen to be $\mathcal{O}(10^{-4})$ with real space cutoff 4.0τ. Starting from a small time step (to remove particle overlaps) I gradually increase the time step to $0.3t_0$. After 6×10^4 time steps

(corresponding to $3700t_0$ due to the varying time step size) I commence sampling and continue for 15×10^4 time steps ($45000t_0$). The electrostatic force on each of the colloids is sampled after every 150 steps, whereas the shifted-truncated LJ repulsions (which exhibit a large variance and decorrelate rapidly) are sampled 30 times more frequently. For each separation, I perform 200 independent runs, resulting in a total of 4×10^5 independent samples per separation for the electrostatic force and 1.2×10^7 samples for the depletion force.

The ICM is incorporated within canonical MC simulations employing single-particle moves with a maximum displacement ℓ_B, resulting in an acceptance rate $\sim 47\%$. To realize the efficiency of the Barnes–Hut octree algorithm for the evaluation of the energy change resulting from a single displacement, we use a tailored variant of the octree routine [49]. The multipole acceptance criteria (MAC) and the order of approximation p in the treecode are set to be MAC $= 0.1$ and $p = 3$, which guarantees a relative error of less than 1.4×10^{-5}. From a random configuration with 276 ions, our collaborators perform simulated annealing over 10^5 cycles (a single cycle corresponds to one move per particle on average), lowering the temperature from $T = 2100$ K to $T = 298$ K. After another 10^5 equilibration cycles, they continue for 10^7 production cycles (100 independent runs of 10^5 cycles per separation), sampling every full cycle. Per separation, this yields 5×10^4 independent samples for the electrostatic force and 2×10^6 samples for the depletion force. The force on one colloid is computed through numerical differentiation, Eq. (2.19).

Figure 2.6(a) shows the mean electrostatic and excluded-volume force as a function of colloid surface separation. I choose $M = 2 \times 1472$ curved surface elements in the IDS and four levels of reflection ("5332") for the ICM, which has 310 image charges per
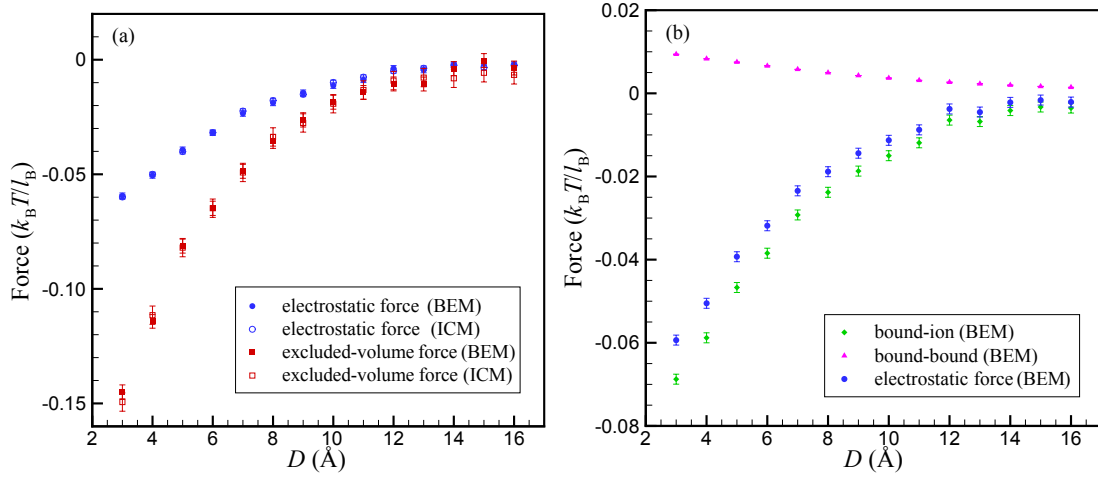
Figure 2.6. Mean force between two neutral dielectric colloids induced by a divalent aqueous electrolyte (100 mM). IDS data are obtained via a MD simulation incorporating the boundary-element method, whereas the ICM data are calculated in a MC simulation with iteratively reflected image charges. (a) Mean electrostatic and excluded-volume force. Note that both forces are attractive and have a similar range. (b) Decomposition of the electrostatic force into an attractive contribution due to ion–bound charge forces (green diamonds) and a repulsive contribution due to the forces between bound charges induced on different colloids (purple triangles; error bars smaller than the symbol size). Note that the blue circles correspond to the same symbols as shown in panel (a), and represent the sum of the bound–bound forces and the bound–ion forces.

ion (10 first-level images, 30 second-level, 90 third-level, and 180 fourth-level). I note that Fig. 2.4(b) indicates that already with parameter choice "4332" the ICM could have achieved an accuracy comparable to that of the IDS for 1472 patches per colloid, although this would have reduced the number of image charges by only 20%. For all separations the IDS/MD and ICM/MC data agree within the statistical uncertainties. These results also demonstrate the importance of polarization effects in the induced colloidal attraction: The electrostatic force has a magnitude of around 40% of the excluded-volume forces. Using the IDS, I can easily decompose the polarization forces into interactions between bound charges residing on separate colloids and interactions between bound charges and ions [Fig. 2.6(b)]. I note that the time-averaged polarization charge vanishes, owing to the anion–cation symmetry of the salt. However, the instantaneous force of a bound charge on the ion that induces it is always repulsive, and this effect is stronger in the region between both colloids, as the ion there will experience a repulsive force from bound charges it induces on both colloids. This leads to a depletion of ions in this region, so that the average net ion–bound charge force between the colloids is *attractive*, reinforcing the depletion attraction induced by the excluded-volume interactions. On the other hand, the bound–bound interaction between the two colloids is repulsive for symmetry reasons.

2.7. Conclusion

I have reviewed two numerical approaches for solving the Poisson equation in systems with discontinuous dielectric constant, namely a method based upon image charges and the IDS based upon discretization of dielectric interfaces. Specifically, both methods are applied to systems comprised of multiple dielectric objects. The IDS can be applied to

arbitrary geometries. The ICM avoids the need for surface discretization by exploiting a closed-form representation of the Green's function, but is restricted to assemblies of spherical objects. I have analyzed the computational complexity of both approaches and through direct comparison have demonstrated how, for a given accuracy, the number of image charges can be reduced at higher reflection levels. My collaborators and I have implemented both methods in particle-based simulations, the IDS within a MD simulation and the ICM within a MC simulation. As a practical demonstration, I have used these simulations to determine the salt-induced attractive effective force between two neutral dielectric colloidal particles.

CHAPTER 3

Application of the IDS to structured dielectric interfaces

This chapter represents a close comparison between my simulation results and the linearized Poisson–Boltzmann theory. The theory part is performed by Prof. Francisco Solis.

3.1. Introduction

The behavior of electrolytes near interfaces has important consequences for surface properties and for processes that take place in their vicinity, such as redox reactions in electrochemical capacitors [76], ion transfer at biomembranes [77], controlling the surface tension of aqueous solutions [78, 79], and establishing colloidal stability via electric double layers [80]. Despite being the very foundation of modern electrochemistry, complete understanding of the electrolyte structure is still elusive. Direct probes of the electrolyte structure near an interface have long been challenging in experiments [81, 82]. Theoretical approaches have used the classical Poisson–Boltzmann (PB) model, which offers good descriptions for dilute symmetric electrolyte, but often breaks down at high concentrations, in asymmetric electrolytes, or near strongly charged surfaces [83, 84, 3]. Such breakdown is due to features ignored in the mean field model such as ion size [85, 86], ion hydration [87], dielectric effects [78], and the molecular-scale structure of the liquid solution [88]. Many refinements in the theory have been made, including the modified Poisson–Boltzmann [7], the Born–Green–Yvon approximations [89], the hypernetted

chain [90], and the charge renormalization [91]. However, we are still far from a complete description. Surface structure can have strong influence on the interfacial properties. In fact, physical roughness should be carefully considered in many applications [92, 93, 94]. For example, the Derjaguin–Landau–Verwey–Overbeek (DLVO) interaction, determined by the repulsive double layer and the attractive van der Waals interaction, differs significantly for rough surfaces compared to perfect smooth ones [95, 96, 97, 98]. Moreover, due to the permittivity mismatch at the interface, ions induce polarization charges on the surface, which is nontrivial for structured surfaces. Such polarization charge profile has to be determined by solving the Poisson's equation.

Numerical solutions to the polarization problem offers another alternative. However, even with the rapid growth of computational power, previous simulation studies have primarily focused on geometrically simple surfaces that the method of image charges can be exploited [99, 24, 100]. One can resort to finite-difference or finite-element methods for structured interfaces. Such algorithms involve discretization of the whole 3-dimensional space, while the induced charges only reside on the surface. Thus, these methods are inefficient for dynamic simulation purposes which require updating the polarization charges at each time step. In this chapter, I apply the iterative dielectric solver (IDS) [2, 14] to study the structured interfaces.

Since surface structures present in nanoscale that is non-feasible for first-principle nor all-atom simulations, I simulate the system with a coarse-grained model with implicit solvent, which captures the finite size effects, the ionic coupling, and the polarization effects. To focus on the dielectric effects, I study neutral dielectric interfaces, where the electrostatic interaction between the interface and the ions is purely due to surface
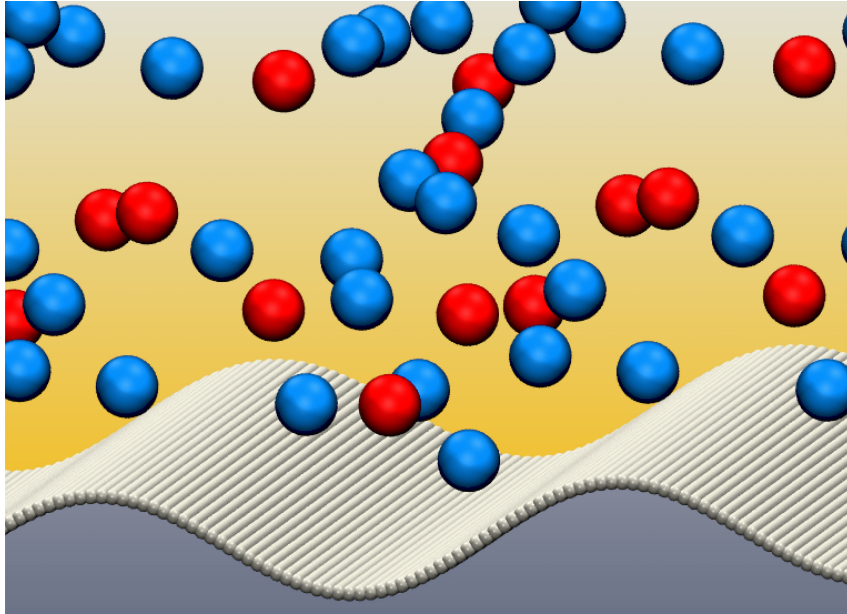
Figure 3.1. Primitive model of an asymmetric electrolyte near a neutral sinusoidal dielectric interface. The positive divalent (red) ions the negative monovalent (blue) ions are emerged in continuum water with relative permittivity $\epsilon_m = 80$. The medium below the interface has relative permittivity $\epsilon_s = 2$. Apart from the polarization charges, the ions also interact with the surface via the shifted–truncated Lenard–Jones potential.

polarization charges. My collaborator also studies the system using a mean field model, the linearized Poisson–Boltzmann equation. Careful modeling of the interaction between the ions and interface allows him to construct a suitable boundary condition that reflects the properties of the rough surface. The model can then reproduce the ion densities near the surface and into the bulk.

3.2. Method and Model

Consider a neural solid–liquid interface $\mathbf{S}$, where the two media have different relative permittivities: $\epsilon_s(\mathbf{s})$ for the solid and $\epsilon_m(\mathbf{s})$ for the liquid medium. As I am able to use the iterative dielectric solver (IDS) to address the interaction of the ions with the dielectric

interface, I can then carry out simulations of a primitive model in this environment. I model the hydrated ions as equal size spheres of diameter $\sigma = 7.14\text{Å}$ with point charges of valence z_i embedded in their centers. In nature, biomolecular structures, such as membranes and proteins often display complicated surface topographies. As a basic model, I consider a solid–liquid interface with sinusoidal surface topography (see Fig. 3.1). The dielectric medium is piecewise uniform separating the electrolyte and a low permittivity medium, in my case $\epsilon_\text{s} = 2$, representing materials such as lipid bilayers [101, 102, 103]. Such dielectric interface can be described by equation $z = A\cos(2\pi x/\lambda)$, where A is the amplitude of surface undulation and λ is its wavelength. I start from a configuration of $A = \sigma$ and $\lambda = 10\sigma$ for our discussion and later vary the amplitude and the surface structure. Since the roughness length scale of our surface is much larger than the water molecule size, I treat the background solvent as implicit dielectric continuum of relative permittivity $\epsilon_\text{m} = 80$. The interface is discretized into a curved rectangular mesh. To capture the excluded volume effects and the atomistic nature of the surface, each mesh point interacts with the ions via the shifted–truncated Lennard–Jones (LJ) interaction. The distance between adjacent mesh points is 0.2σ. Such fine mesh also guarantees less than 10^{-3} error in the force calculation of the IDS for worst configurations when ions are closest to the surface. Since for symmetric electrolytes, dielectric effects are the same for both ion species, it is more interesting to explore the behavior of asymmetric electrolytes. I carry out simulations of 2:1 electrolytes at 50 mM concentration. Slab simulation box of dimension $10 \times 10 \times 100\sigma^3$ is used with periodicities in both x and y directions. The dielectric interface is centered at $z = 0$. The electrolyte only stays in upper half of the box. The slab height is sufficiently high to eliminate the boundary effects. Using a Langevin

thermostat with damping time $20t_0$, where $t_0 = (m\sigma^2 k_B T)^{1/2}$ is the LJ unit time with $k_B T$ the Boltzmann factor and m the ion mass. The system is kept at room temperature with Bjerrum length $l_B = \sigma$.

To better understand the features observed in the simulations, my collaborator and I contrast them with results from a linearized mean field theory. He uses a standard linear PB description of the electrolyte bulk. Boundary conditions for the model are constructed so as to capture the behavior of the ions near the surface. In the PB approximation, the mean field electric potential ϕ satisfies the equation $\nabla^2 \phi - \kappa^2 \phi = 0$, where the square inverse screening length is $\kappa^2 = 4\pi e^2 (\sum_i c_i Z_i^2)/(\epsilon_0 k_B T)$ with e the proton charge, c_i and Z_i the concentration and the valence of the ith ion species, respectively. The charge density ρ is then obtained from the potential as $\rho = -(\sum_i c_i Z_i^2)e\phi/(k_B T)$. Boundary conditions for the potential and surface charge density should reflect the properties of the polarizable surface. Simulation observations and the geometric structure of the surface suggest that the potential at the surface, at points with coordinate x along the modulation direction should be, approximately, of the form $\phi|_\mathbf{s} = \Phi_0 + \Phi_1 \cos(2\pi x/\lambda)$. The constants Φ_0 and Φ_1 can be chosen to fit the simulations over a range of conditions. To solve the equation, it is convenient to use curvilinear coordinates (s, y, t) adapted to the surface. The y coordinate is unchanged, while $x = s - A\sin(2\pi s/\lambda)\exp{-t/\lambda}$ and $z = t + A\cos(2\pi s/\lambda)\exp{-t/\lambda}$. In the new coordinates, the actual surface corresponds to $t = 0$. The PB equation can now be solved in a power expansion on the amplitude of the modulation. My collaborator carries out this procedure below and show that the bulk behavior of the system can be approximated in this way for small modulation amplitudes. It can be shown that the leading term in the expansion of the potential has the form $\phi = \Phi_0 \exp(-\kappa t)$, while higher

order terms in the expansion acquire an oscillatory behavior along the s (or x) coordinate while decaying into the bulk along the t (or z) coordinate.

The form of the boundary condition noted above can be justified by considering the interaction of a single ion with the polarizable surface. An approximate calculation of the features of this interaction can be carried out as a perturbative expansion on the surface modulation amplitude. The mean field energy of a single ion of valence Z near the surface, ignoring the presence of all other ions, is $U = (1/2)Ze\phi_P$ where ϕ_P is the electric potential that arises solely from the surface polarization charges. The perturbative approach expands the polarization potential as $\phi_P = \phi_P^{(0)} + \phi_P^{(1)} + \ldots$, and similar expansions are applied to the charge density and the geometric quantities. The order of a term in the expansion is the power of the modulation amplitude A that appears in the expression. The potential is calculated by first solving Eq. (2.4) for the polarization charges. The zeroth order of this calculation corresponds to the case of a single ion near a flat interface. In that case, we have $\bar{\epsilon}\sigma^{(0)} + \epsilon_0 \Delta\epsilon \hat{\mathbf{n}}^{(0)} \cdot \mathbf{E}^{(0)} = 0$. Since $\hat{\mathbf{n}}^{(0)} \cdot \mathbf{E}^{(0)}$ receives no contribution from other polarization charges as the fields they create are parallel to the surface, we have $\mathbf{n}^{(0)} \cdot \mathbf{E}^{(0)} = (4\pi\epsilon_0)^{-1} Ze\mathbf{x}/|\mathbf{x} - \mathbf{x}'|^3$, where $\mathbf{x}'$ is a point at the surface and we take the ion position as $\mathbf{x} = (0, 0, a)$. Integration of the Coulomb potential due to the resulting surface charge density gives the standard image-charge potential $\phi_P^{(0)} = (4\pi\epsilon_0)^{-1}(\Delta\epsilon/\bar{\epsilon})Ze/(2a)$. The resulting energy of the ion is $U^0 = (4\pi\epsilon_0)^{-1}(\Delta\epsilon/\bar{\epsilon})Z^2 e^2/(4a)$. This expression is positive when the solid phase has a lower permittivity.

The first order term in the expansion of the potential is associated with the deformation of the surface. To simplify its calculation, we consider the limit where the ion is brought to the interface. In addition, we consider first the case where its position

coincides with a peak of the deformed surface. Results for other positions follow from this result. According to the image-charge result, the energy in this limit is singular but the exclusion of a small region around the ion renders the result finite. We denote the size of this region as a to indicate that it can be made to correspond to the distance from the surface. The evaluation retains an explicit dependence on the wavelength, which is the key feature of interest in our analysis. A more complex calculation, maintaining the ion at a finite distance from the interface, gives similar results. In this limit, the first oder terms in Eq. (2.4) read $\bar{\epsilon}\sigma^{(1)} + \epsilon_0\Delta\epsilon\hat{\mathbf{n}}^{(1)} \cdot \mathbf{E}^{(0)} = 0$. Other terms in the expansion of the equation cancel due to the geometry used. The first order term in the expression for the normal is $\hat{\mathbf{n}}^{(1)} = [-(2\pi A/\lambda)\sin(2\pi x/\lambda), 0, 0]$. We obtain $\sigma^{(1)} = -(2\pi A/\lambda)(\Delta\epsilon/\bar{\epsilon})Ze\sin(kx)x/(x^2 + y^2)^{3/2}$. The potential created at the ion location is the integration of this density times the Coulomb potential. The potential has a leading term $\phi_{\mathrm{P}}^{(1)} = (\Delta\epsilon/\bar{\epsilon})CZe(A/\lambda^2)\ln a$ with C a positive constant. For positive ions, this excess potential is negative. For other positions, the leading term in the potential is approximately $\phi_{\mathrm{P}}^{(1)} = (\Delta\epsilon/\bar{\epsilon})\cos(2\pi x/\lambda)CZe(A/\lambda^2)\ln a$. We note that the mean curvature of the surface $R^{-1} = (1/2)\cos(2\pi x/\lambda)$. Therefore, our result can be understood as indicating the dependence of the potential as a function of the curvature $\phi_{\mathrm{P}}^{(1)} = (\Delta\epsilon/\bar{\epsilon})CZeR^{-1}\ln(a)/2$. This expression can be used as an approximation for the potential in cases other than sinusoidal modulation. As a result, the energy of interaction between ion and surface has the first order contribution $U^{(1)} = (\Delta\epsilon/\bar{\epsilon})(C/4)Z^2eR^{-1}\ln a$.

For a particle near the surface the dominant term of its energy is given by its interaction with the polarization charges. We can then write the excess charge density near the surface in terms of the Boltzmann population factor $\exp[-(U^{(0)} + U^{1)})/k_BT]$. Using our results

for the potential due to the surface, we see that the expansion of this expression results in contributions that match the from indicated by the modulated boundary condition. Expanding the exponential factor and multiplying by the bulk densities, we obtain an excess charge density near the surface, within an atomic diameter from it, of the form

$$(3.1) \qquad \delta q = -\sum_i c_i e Z_i^3 \left[C_1 - C_2 A \lambda^{-2} \cos(2\pi x/\lambda) \right] \ .$$

In this expression, the constants C_i are positive according to the functional form of the estimated potentials. Their values can be estimated in terms of the parameters of the system but we note that, within the calculation outlined above, they depend on the specific cutoff a chosen. Equation (3.1) retains the dependence on valencies and characteristic lengths. In particular, we emphasize that the result is not zero for asymmetric electrolytes. The net charge is a result of the asymmetric depletion of ions near the interface. Additionally, the sign of the first order term indicates that the depletion is stronger at concave regions. Given the form of the excess charge density, and the linear PB relation between charge density and potential, this result requires the boundary values of the potential to take the modulated form introduced above.

3.3. Results and Discussion

Figure 3.2 shows results for the ion number density near the modulated surface for the 2:1 electrolyte. In the absence of dielectric contrast, as expected, up to fluctuations, the bulk monovalent ion density is twice of the divalent ions. Steric effects do create a small asymmetric depletion near the surface, which are stronger for the divalent ions. This effect appears as ions near the interface lack a symmetric shell of screening counterions. The
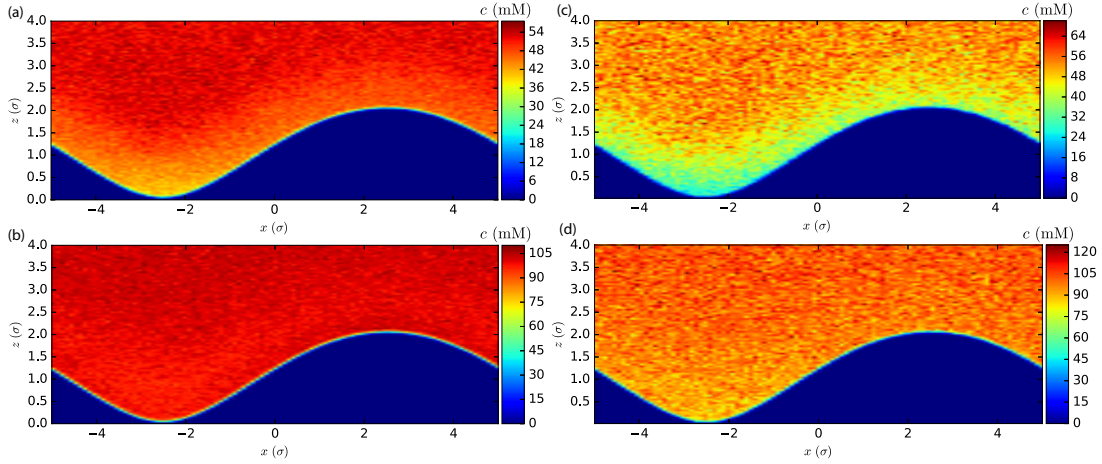
Figure 3.2. (a) The divalent ion and (b) the monovalent ion density distributions above a structured interface *without* dielectric mismatch. (c) and (d) are the corresponding ion distributions *with* permittivity mismatch 80/2. The polarization charges significantly increase the surface depletion.

asymmetric counterion shell pulls the ions towards the bulk [69]. These results serve as a baseline to assess the effects of the dielectric contrast case. Once the dielectric contrast is turned on, I observe a much stronger depletion of both charge species, which is enhanced by the dielectric effects as the ions interact with their own polarization charges of the same kind. This depletion extends further into the bulk than the one created by steric effects, showing the long range nature of electrostatic interactions. More importantly, since the interaction between the ion and its polarization charges scales with Z^2 and decays as r^{-1} with r the ion–surface distance, the divalent ions are much more depleted near the surface than the monovalent ions. Such asymmetry breaks the balance of concentration in the bulk, i.e., $c_{+2} = (1/2)c_{-1}$ for charge neutrality, and results in a net negative charge cloud above the surface [see Fig. 3.3(a)]. It is important to note that although similar effect happens even for the interface without dielectric mismatch [see Fig. 3.3(b)] due to difference in the counterion shell, the net charge density is substantially weaker.
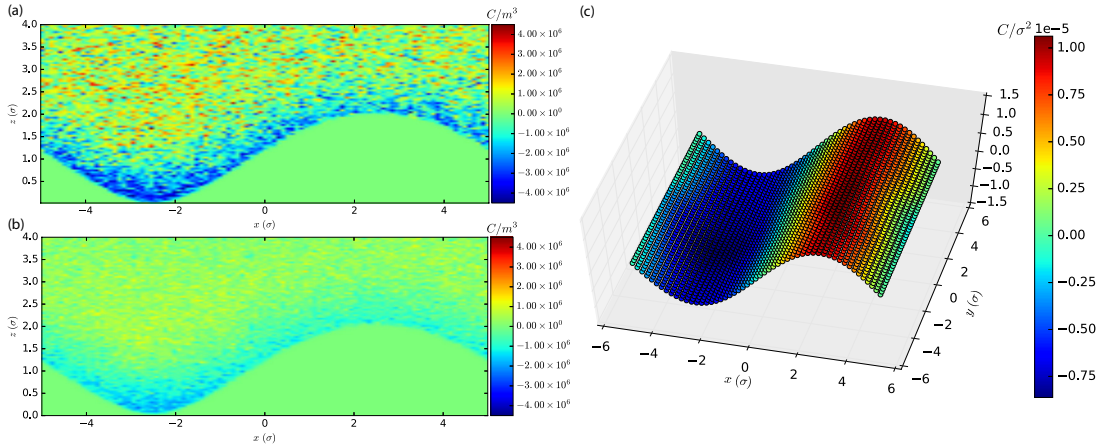
Figure 3.3. The net charge cloud formed by 50 mM 2:1 electrolyte above a (a) structured dielectric interface of permittivity 80/2, (b) neutral interface without dielectric mismatch. (c) The corresponding surface polarization charge density.

Along with the charge density due to ions, my simulations also calculate the average surface induced charge density. The net induced charge of the interface is zero, but it presents persistent non-zero averages as a function of position, consistent with the modulation of the ionic charge density. The average induced charge density is positive at concave regions and negative in the convex ones as shown in Fig. 3.3(c).

The dependence of the induced charge and ion charge density on surface structure can be further investigated by changing the parameters of the modulated surface. I have carried out simulations where the modulation magnitude A ranges from 0 to 2σ. Figure 3.4 shows the induced charge density averaged over the y direction, along which the properties of the system are invariant. For small amplitudes, the induced charge density profile shows a sinusoidal pattern, consistent with the arguments developed for the linearized Poisson–Boltzmann theory. For larger amplitudes, I observe that the induced charge density amplitude is larger and varies more rapidly at the peak than at the valley. The sinusoidal
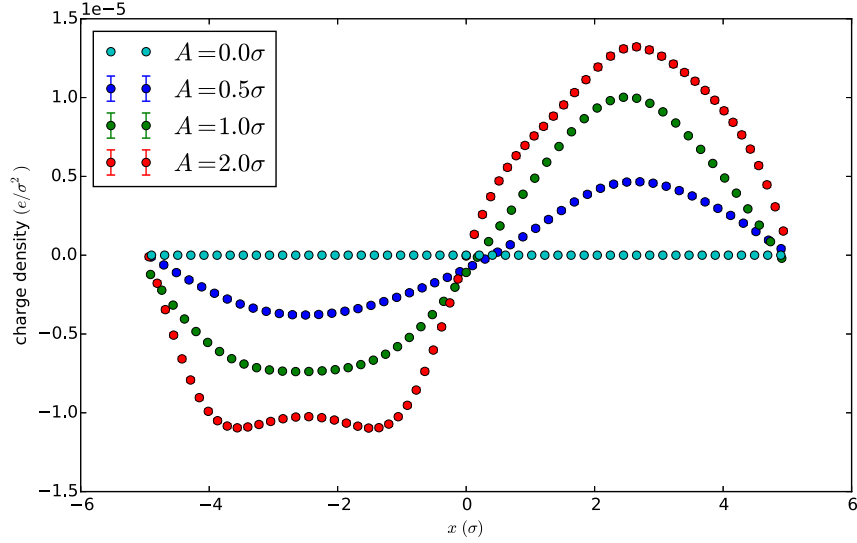
Figure 3.4. The net surface polarization charge distribution at various undulation amplitudes.

behavior breaks down at high amplitude ($A = 2.0\sigma$). This is caused by steric effects as ions cannot reach the bottom of the valley since the gap between the two slopes becomes too narrow.

For the range of amplitudes where the observed response is linear, it is possible to analyze the simulation results in light of the linearized PB approach outlined above. For the case $A = \sigma$, my collaborator solves the PB equation for the bulk ion density while fitting the potential amplitudes in Eq. (3.1) to match the simulation results. With the fitted boundary conditions, the model solutions reproduce key features of the simulations results: the region of significant charge density deviation from neutrality in the simulations corresponds to the screening length size from the model. In agreement to the simulations, the model predicts a sinusoidal charge distribution along the surface modulation direction both at the solid–liquid interface and within the bulk. Fig. 3.5 shows the ionic charge density from the solutions to linearized PB equation. Panels (b) and (c) of the figure
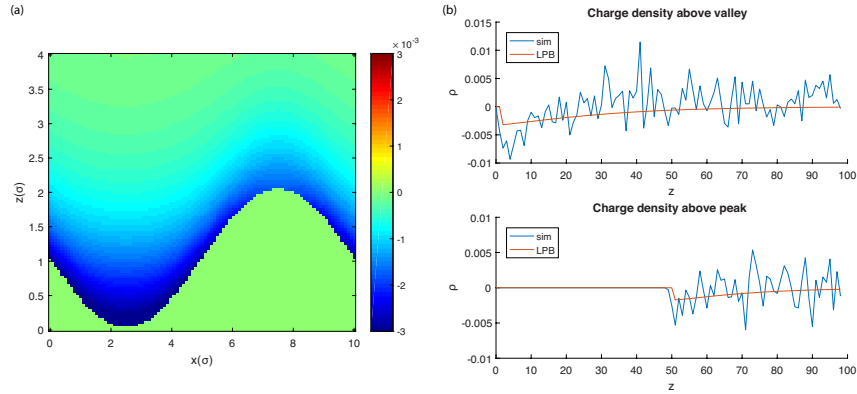
Figure 3.5. (a) The charge density obtained from solution to the linearized PB equation. The boundary condition constants were chosen to best match (see main text) the properties of the simulation data for undulation amplitude $A = \sigma$. (b) Comparison between the simulation results and the linearized PB predictions for densities along the z coordinates for x positions that coincide with the peak and the valley of the surface, respectively.

show comparisons of the model solution with simulation results for the densities observed along the z direction at positions above the peak and the valley of the surface. Charge density simulation data is fitted to the functional form of the PB solution that has two constants that can be used for the fit. The constants are determined by a least squared fitting of the charge density above the peaks and the valleys. While the simulation results have noise, it is possible to observe the decay of the average charge density into the bulk as well as the difference in the values of the density at the peak and valley points.

The phenomenon I have found in my simulations and model analysis, of curvature dependent charge depletion is generic, not limited to surfaces with modulation in a single dimension, and can be generalized to other structures. For example, Fig. 3.6 shows the net surface polarization charge pattern of the same 50 mM 2:1 electrolyte above a structured dielectric interface with permittivity mismatch 80/2, but has surface modulation in both
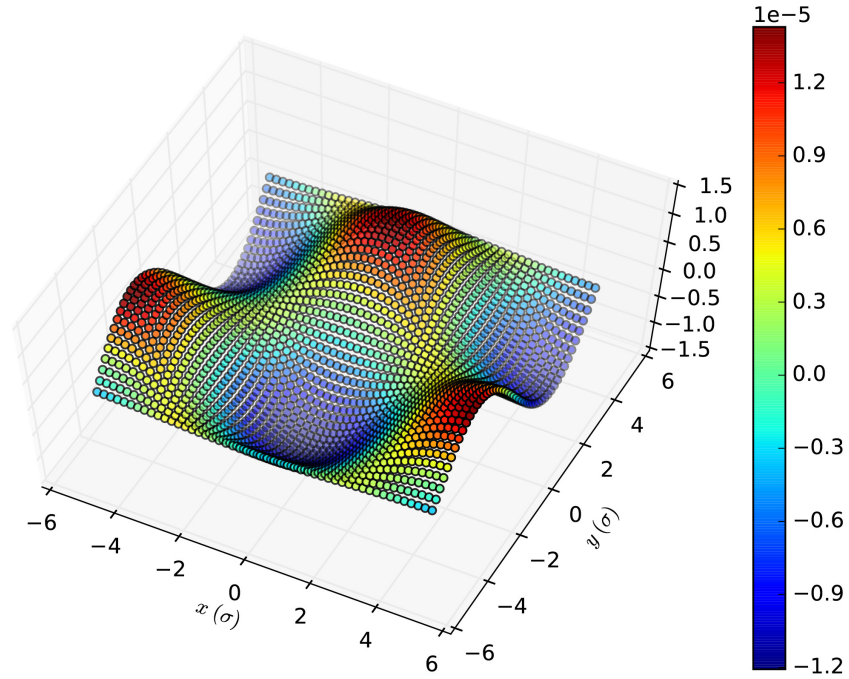
Figure 3.6. The surface induced charge density of a structured dielectric interface with modulations in both x and y directions. Same as the sinusoidal case, the dielectric mismatch is 80/2 with a 50 mM 2:1 electrolyte is above the surface.

x and y directions $z(x, y) = A \cos(kx) \sin(ky)$. Similar to my previous results, the valleys acquire a negative surface polarization charge.

3.4. Conclusion

The simulations presented, along with the arguments used in the construction of the mean field theory, demonstrate that the effect observed is universal. The local curvature of the surface always induces effective surface polarization and ion accumulation in the presence of asymmetric electrolytes. The effect should be observable not only in the electrolyte bounding walls, but also at the surface of electrolyte-immersed colloids. These findings can be applied to the design of surfaces with useful physical–chemical properties.

CHAPTER 4

The refined IDS for multiple dielectric mismatches

The content of this chapter is based on the following publication:

- Huanxin Wu and Erik Luijten, Accurate and efficient numerical simulation of dielectrically anisotropic particles (in submission)

4.1. Introduction

Although in principle BEM-based matrix equation solvers can be applied to obtain the electrostatic potential around dielectric objects of arbitrary geometry and dielectric configuration, it is well known that its accuracy and convergence rate are highly dependent on the conditioning of the boundary-element equations [104]. This conditioning depends not only on the BEM formalism [43], but also on many other factors, including object geometry [2], level of discretization, and shape of each boundary-element [43, 105]. It can be improved via *preconditioning* techniques, such as proposed in the context of both Poisson's equation [106] and the Poisson–Boltzmann equation [107] for multi-region dielectric problems with large numbers of boundary elements. However, neither the role of dielectric heterogeneities (such as present in patchy colloids, proteins, etc.) nor the spectrum of the BEM matrix have been examined explicitly. Here we perform such an analysis and attain an intuitive physical understanding of the role of preconditioning. This in turn enables us to extend the iterative dielectric solver (IDS) introduced in Refs. 2 and 14 for achieving high accuracy and fast convergence of the BEM. The technique proposed here has been

successfully applied to study the electric double layer of colloids that are anisotropic in shape as well as permittivity [108] and is applicable to arbitrarily shaped objects with multiple dielectric mismatches.

Unlike finite-difference methods (FDM) [109, 110, 111, 112] or finite-element methods (FEM) [113, 114], which partition the entire spatial domain, BEMs instead formulate partial differential equations as boundary integral equations, and only seek the boundary values. For Poisson's equation in electrostatics, the boundary values can either be the surface charge density or the surface potential and its derivatives. The boundary-integral formulation of Poisson's equation is then solved to match these boundary values with given boundary conditions. Since the permittivity often varies rapidly at dielectric boundaries, the approximation of sharp dielectric interfaces that separate piecewise uniform media is typically utilized in the modeling of dielectric materials [28]. Under this assumption, Poisson's equation only needs to be solved on two-dimensional meshes instead of three-dimensional (3D) grids.

4.2. Methods and Results

Following the notation and the derivation of Eq. (2.4) (cf. Sec. 2.2), here I discuss the principles of the BEM that are applied to the IDS, which help to distinguish the IDS from previous BEM methods. The BEM discretizes the interfaces and represents the continuous surface charge density $\sigma(\mathbf{s})$ with a set of basis functions $f_i(\mathbf{s})$ defined at each of N boundary patches,

$$(4.1) \qquad \sigma(\mathbf{s}) = \sigma_{\mathrm{f}}(\mathbf{s}) + \sigma_{\mathrm{pol}}(\mathbf{s}) = \sum_{i=1}^{N} \sigma_i f_i(\mathbf{s}) \, ,$$

where σ_i is the weight at the ith patch [115]. For simplicity, piecewise-constant basis functions are widely adopted [43, 116],

$$
(4.2) \qquad f_i(\mathbf{s}) = \begin{cases} 1 & \text{if } \mathbf{s} \in s_i \\[2mm] 0 & \text{if } \mathbf{s} \notin s_i \end{cases} ,
$$

where s_i is the enclosure of patch i. Under this approximation, $\sigma(\mathbf{s})$ is discretized onto the N boundary patches, each carrying a charge density σ_i. For a finite number of patches, this approximate $\sigma(\mathbf{s})$ does not satisfy Eq. (2.4) exactly, but results in a residual. To minimize this residual, the BEM forces it to be orthogonal to a set of test functions [117]. If these test functions coincide with our basis functions, this would reduce to the standard Galerkin method [104]. If, in addition to the discretization, we assume that the bulk free charge distribution consists of point charges, Eq. (2.4) can be written in matrix form $\mathcal{A}\boldsymbol{\sigma} = \mathbf{b}$, with

$$
(4.3) \qquad \mathcal{A}_{ij} = \iint_{s_i} \left\{ \bar{\epsilon}(\mathbf{s})\delta_{ij} + \iint_{s_j} \left[\frac{\Delta\epsilon(\mathbf{s})}{4\pi} \frac{\hat{\mathbf{n}}(\mathbf{s}) \cdot (\mathbf{s} - \mathbf{s}')}{|\mathbf{s} - \mathbf{s}'|^3} \right] d\mathbf{s}' \right\} d\mathbf{s}
$$

and

$$
(4.4) \qquad b_i = -\iint_{s_i} \left[\frac{\Delta\epsilon(\mathbf{s})}{4\pi} \sum_k \frac{q_k}{\epsilon(\mathbf{r}_k)} \frac{\hat{\mathbf{n}}(\mathbf{s}) \cdot (\mathbf{s} - \mathbf{r}_k)}{|\mathbf{s} - \mathbf{r}_k|^3} \right] d\mathbf{s} + \iint_{s_i} \sigma_\mathrm{f}(\mathbf{s})d\mathbf{s} \ .
$$

The nested integral in Eq. (4.3), if evaluated via one-point quadrature at patch centroids, can lead to two different formulations. If $\mathbf{s}$ is evaluated at s_i, we have the collocation

approach [118], with

$$(4.5) \qquad \mathcal{A}_{ij} = \iint_{s_i} \bar{\epsilon}(\mathbf{s})\delta_{ij}d\mathbf{s} + a_i \frac{\Delta\epsilon(\mathbf{s}_i)}{4\pi} \iint_{s_j} \frac{\hat{\mathbf{n}}(\mathbf{s}_i)\cdot(\mathbf{s}_i-\mathbf{s}')}{|\mathbf{s}_i-\mathbf{s}'|^3}d\mathbf{s}' \; .$$

If $\mathbf{s}'$ is evaluated at s_j, we arrive at the qualocation approach [119], which at similar computational effort gives much better accuracy [116, 1], especially for flat patches [64].

For large-scale simulations, the solver must not only be accurate, but also highly efficient. IDS [2] takes the qualocation approach,

$$(4.6) \qquad \mathcal{A}_{ij} \;=\; a_i\bar{\epsilon}(\mathbf{s}_i)\delta_{ij} + a_j \frac{\Delta\epsilon(\mathbf{s}_i)}{4\pi} \iint_{s_i} \frac{\hat{\mathbf{n}}(\mathbf{s})\cdot(\mathbf{s}-\mathbf{s}_j)}{|\mathbf{s}-\mathbf{s}_j|^3}d\mathbf{s} \; ,$$

$$(4.7) \qquad b_i \;=\; -\frac{\Delta\epsilon(\mathbf{s}_i)}{4\pi} \iint_{s_i} \sum_k \frac{q_k}{\epsilon(\mathbf{r}_k)} \frac{\hat{\mathbf{n}}(\mathbf{s})\cdot(\mathbf{s}-\mathbf{r}_k)}{|\mathbf{s}-\mathbf{r}_k|^3}d\mathbf{s} + \iint_{s_i} \sigma_{\mathrm{f}}(\mathbf{s})d\mathbf{s} \; ,$$

where Eq. (4.6) can be precomputed for fixed dielectric geometries, but becomes time-dependent for mobile dielectric objects. Thus, to reduce computational cost, the integral is approximated by one-point (centroid) quadrature for $i \neq j$ and a curvature correction is added by assuming disk-shaped patches with mean curvature for $i = j$ [31]. By further assuming that source charges cannot approach the dielectric interfaces very closely, and approximating Eq. (4.7) via one-point quadrature as well, we arrive at simplified expressions for which the collocation and qualocation approaches coincide,

$$(4.8) \qquad \mathcal{A}_{ij} \;=\; \bar{\epsilon}_i\delta_{ij} + a_j \frac{\Delta\epsilon_i}{4\pi} \frac{\hat{\mathbf{n}}_i\cdot(\mathbf{s}_i-\mathbf{s}_j)}{|\mathbf{s}_i-\mathbf{s}_j|^3} \; ,$$

$$(4.9) \qquad b_i \;=\; -\frac{\Delta\epsilon_i}{4\pi} \sum_k \frac{q_k}{\epsilon(\mathbf{r}_k)} \frac{\hat{\mathbf{n}}_i\cdot(\mathbf{s}_i-\mathbf{r}_k)}{|\mathbf{s}_i-\mathbf{r}_k|^3} + \sigma_{\mathrm{f}}(\mathbf{s}_i) \; ,$$
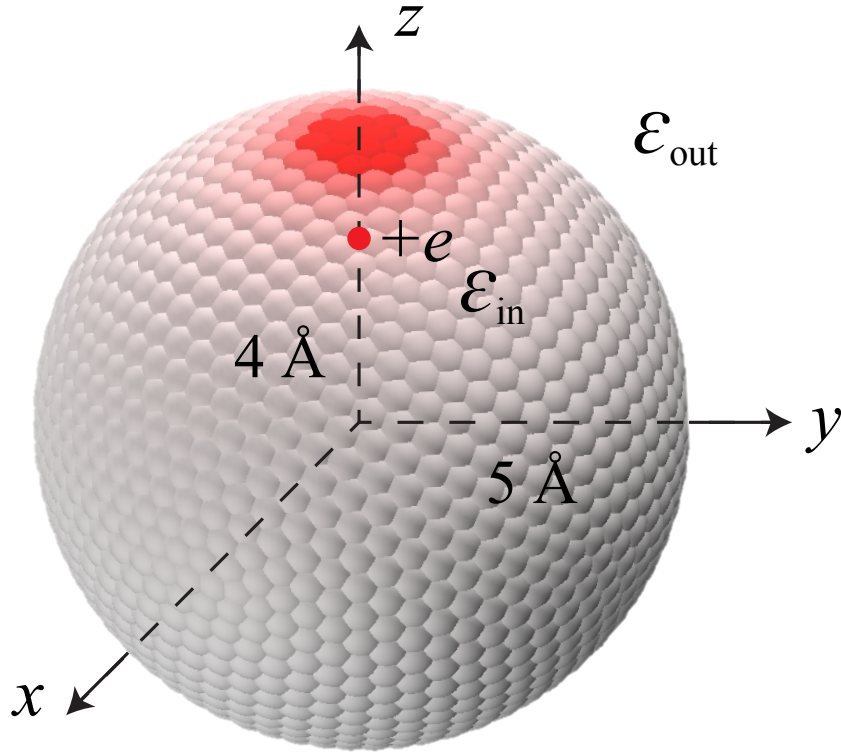
Figure 4.1. Test system introduced in Ref. 1 to examine the accuracy of various Poisson solvers. A positive unit charge is placed 4 Å from the center of a dielectric sphere ($\epsilon_{\text{in}} = 80$) of radius 5 Å. The sphere is embedded in a background medium with relative permittivity $\epsilon_{\text{out}} = 2$. Shading on the sphere surface indicates the induced charge.

with $\bar{\epsilon}_i \equiv \bar{\epsilon}(\mathbf{s}_i)$, $\Delta\epsilon_i \equiv \Delta\epsilon(\mathbf{s}_i)$, and $\hat{\mathbf{n}}_i \equiv \hat{\mathbf{n}}(\mathbf{s}_i)$. To retain the dimensionality of Eq. (2.4), I have divided both sides of $\sum_j \mathcal{A}_{ij}\sigma_j = b_i$ by the patch area a_i.

In the context of the dielectrically heterogeneous particles examined below, it proves insightful to first closely examine the performance of the IDS approach proposed in Ref. 2 for a uniform spherical particle, with specific focus on the consequences of the one-point quadrature in Eqs. (4.8) and (4.9). We adopt a test case from Ref. 1, i.e., the polarization potential of a dielectric sphere ($\epsilon_{\text{in}} = 80$, $\epsilon_{\text{out}} = 2$) of radius 5 Å, induced by a positive unit charge ($q = +e$) located *inside* the sphere, at a distance 4 Å away from the sphere

center (Fig. 4.1). In Ref. 1, this was found to be a remarkably challenging system, with strong deviations between some numerical approaches and the analytical solution [120] for the induced potential along the z-axis. The collocation approach [32] was observed to yield a potential more than twice smaller than the analytical result for a spherical surface discretized into 364 or 1456 flat tiles, with each tile subdivided into 100 elements for numerical integration (Fig. 4.2). On the other hand, the qualocation method [119] was found to yield excellent agreement with the analytical solution for the same tiling and subdivision. Figure 4.2 shows that even the one-point quadrature implementation of IDS performs far better than collocation with flat disks [32, 64], for similar global discretization levels (i.e., number of patches employed for the entire sphere). Yet, the deviation from the analytical result is still quite significant. This is fully mitigated by imposing the "net induced-charge constraint" derived in Ref. 2. For this test case, the net induced charge on the sphere is nonzero, and the total (free *and* bound) charge Q should be q/ϵ_{out} (Ref. 2, Sec. IV.H). The total bound charge itself consists of two contributions: the bound charge at the source charge location $(q/\epsilon_{\text{in}} - q)$ and the surface induced charge, so that the latter must equal $q/\epsilon_{\text{out}} - q/\epsilon_{\text{in}}$. Mathematically, such "net induced-charge constraint" is equivalent to the boundary condition at infinity, where the electrostatic potential Φ of the system should approach $\Phi(\mathbf{r})|_{r\to\infty} = \frac{Q}{4\pi\epsilon_0 r}$. To enforce this physical constraint within GMRES, for simplicity I evenly distribute the net charge over all patches for the initial trial solution $\boldsymbol{\sigma}^{(0)}$ and enforce the inner product of the patch areas $(a_1, a_2, \ldots, a_N)$ and each subsequent basis vector, $\Delta^{(m)} = \sum_{i=1}^{N} a_i(\mathbf{q}_m)_i$, to be zero, by subtracting $\Delta^{(m)}/N$ from the computed induced surface charge of each patch at every iteration. This technique, which comes at negligible computational cost, yields excellent

agreement with the analytical solution and rapid convergence as a function of the number of surface patches. Indeed, the accuracy is comparable with the full qualocation approach at similar discretization levels, while avoiding the use of subpatch discretization to obtain the second term of $\mathcal{A}_{ij}$ in Eq. (4.6) (i.e., only a single evaluation per patch, rather than numerical integration over 100 subtiles). I note that IDS [2] employs patches with a fixed curvature, implemented via a curvature correction [31], but this is not to be confused with curved surface elements [64], which are computationally far more costly. Also, I have explicitly verified that this curvature correction has a near-negligible effect on the results in Fig. 4.2.

The high accuracy of IDS for this test case arises from two aspects of the spectrum of the matrix operator $\mathcal{A}$. First, $\mathcal{A}$ is well-conditioned. For $\mathcal{A}\boldsymbol{\sigma} = \mathbf{b}$, the L_2-norm condition number $\kappa(\mathcal{A}) = \eta_{\max}(\mathcal{A})/\eta_{\min}(\mathcal{A})$ characterizes the sensitivity of the solution $\boldsymbol{\sigma}$ to a perturbation in $\mathbf{b}$, where $\eta_{\max}(\mathcal{A})$ and $\eta_{\min}(\mathcal{A})$ are the largest and smallest singular values of $\mathcal{A}$, respectively. A perturbation $\delta\mathbf{b}$ in $\mathbf{b}$ will lead to a perturbation $\delta\boldsymbol{\sigma}$ in $\boldsymbol{\sigma}$, whose norm is bounded by the condition number [121],

$$(4.10) \qquad \frac{\|\delta\boldsymbol{\sigma}\|}{\|\boldsymbol{\sigma}\|} \leq \kappa(\mathcal{A})\frac{\|\delta\mathbf{b}\|}{\|\mathbf{b}\|} \ .$$

A typical MD simulation employs a fast Ewald solver with moderate accuracy, leading to inaccuracies in $\mathbf{b}$. Thus, an accurate solution of $\boldsymbol{\sigma}$ requires a small condition number $\kappa(\mathcal{A})$. For a normal matrix, $\kappa(\mathcal{A}) = |\lambda_{\max}(\mathcal{A})|/|\lambda_{\min}(\mathcal{A})|$, with λ its eigenvalues. Whereas the sphere of Fig. 4.1 is dielectrically isotropic, the patches differ slightly in area, causing the matrix $\mathcal{A}$ to be asymmetric, which results in complex eigenvalues, albeit with small imaginary parts. The condition number $\kappa(\mathcal{A})$ can be computed explicitly, since the spectrum λ
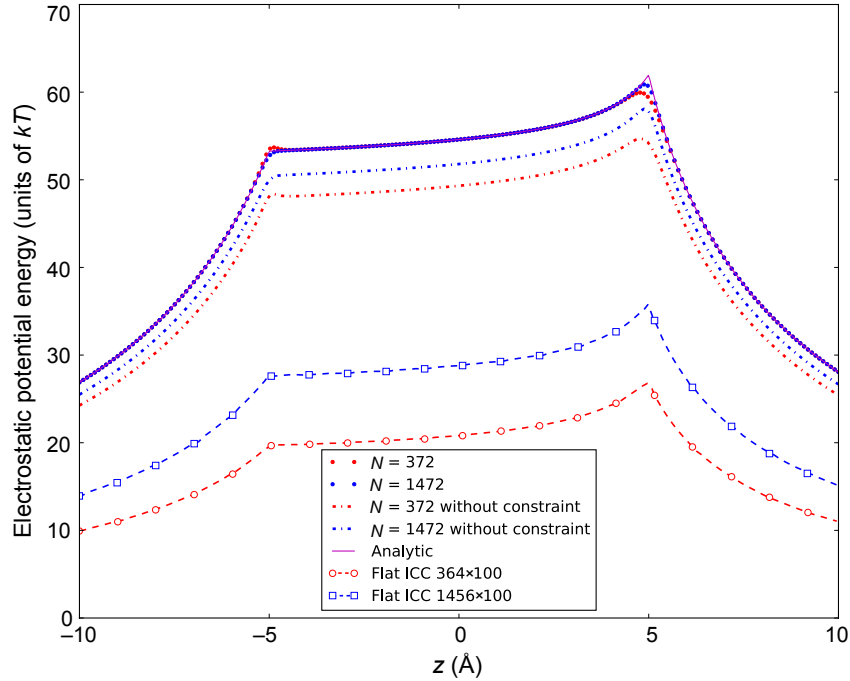
Figure 4.2. Accuracy comparison between the IDS (*iterative dielectric solver*) implementation of Ref. 2 and more costly alternative techniques for the induced charge potential along the z axis for the configuration of Fig. 4.1. Purple solid line marks the analytical solution. Open symbols represent data from Ref. 64 employing the induced charge computation (ICC) method [32], where the sphere is discretized into 364 (red open circles) and 1456 (blue open squares) flat patches with 100 subtiles per patch. The large discrepancy between these data and the analytical result can be significantly reduced by using one-point quadrature [2] (dashed lines marked "without constraint," for comparable patch numbers, namely 372 (red) and 1472 (blue)). Enforcing the net induced-charge constraint (cf. Ref. 2 and main text) improves the data (small red and blue solid circles) such that they become indistinguishable from the analytical result, except near the two surface boundary points ($z = \pm 5\text{Å}$), where discretization effects dominate. This improvement, which is achieved at negligible additional computational cost, can be understood from the eigenvalue spectrum of the operator employed in the IDS (see main text).
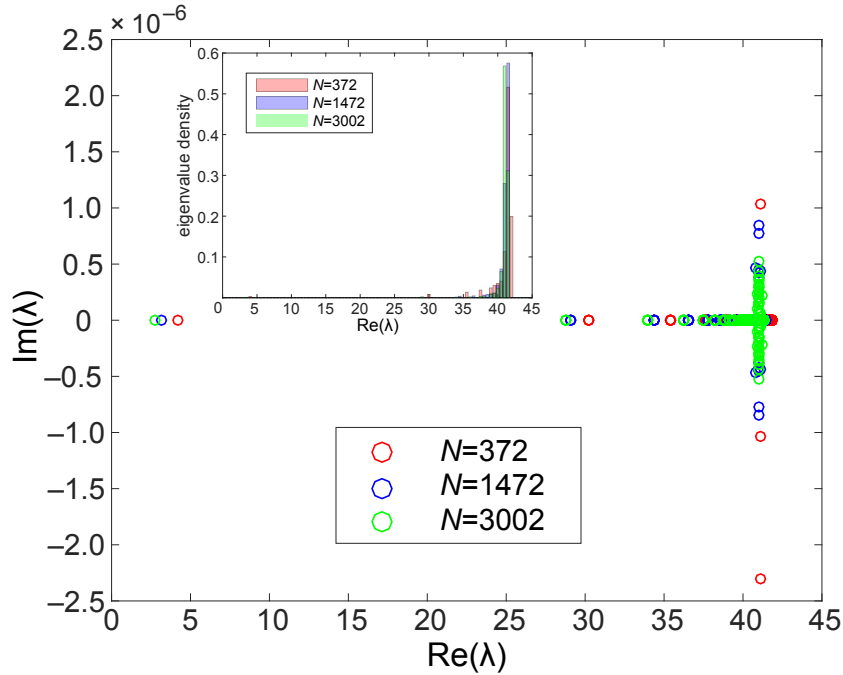
Figure 4.3. Complex spectrum λ of the operator $\mathcal{A}$ in Eq. (4.8) for the dielectric sphere of Fig. 4.1 at different discretization levels N. As N increases, the real parts of the smallest and largest eigenvalues approach 2 and 41, respectively, in agreement with Eq. (4.11) [2]. The imaginary parts are small across the entire spectrum, reflecting the near-symmetric character of $\mathcal{A}$. The inset shows the histogram of the real parts $\mathrm{Re}(\lambda)$, illustrating that apart from the outlying smallest eigenvalue all other values are clustered.

of $\mathcal{A}$ was solved analytically for a spherical geometry [2],

$$(4.11) \qquad \lambda = \left\{ \epsilon_{\mathrm{out}}, \left(\frac{2}{3}\epsilon_{\mathrm{out}} + \frac{1}{6}\epsilon_{\mathrm{in}} \right), \ldots, \left(\frac{1}{2}\epsilon_{\mathrm{out}} + \frac{1}{2}\epsilon_{\mathrm{in}} \right) \right\} \ .$$

yielding $\kappa(\mathcal{A}) = 41/2$, sufficiently small to guarantee a well-conditioned matrix.

In Fig. 4.3 I evaluate the eigenvalues of $\mathcal{A}$ based upon Eq. (4.8), at different discretization levels. The extreme eigenvalues $\min(\lambda)$ and $\max(\lambda)$ gradually approach the analytical predictions, i.e., 2 and 41, as the patch number N is increased. The relative imaginary

parts $\mathrm{Im}(\lambda)/\mathrm{Re}(\lambda)$ are indeed very small and decrease as N increases, indicating $\mathcal{A}$ is close to a normal matrix. For 372 patches, we find $\kappa(\mathcal{A}) \approx 9.87$.

The second contribution to the accuracy of the IDS also follows from the spectrum. Namely, the convergence rate of GMRES depends on the eigenvalue distribution of $\mathcal{A}$ in the complex plane [122]. For fast convergence, the eigenvalues should be clustered away from zero, i.e., the distance between any two eigenvalues should be much smaller than the distance of any eigenvalue from the origin [123, 124]. Figure 4.3 shows that the minimum eigenvalue is isolated from the other eigenvalues, compromising the quality of the spectrum. The eigenvector of this outlying eigenvalue is uniform, corresponding to a uniform surface charge density [2]. As the total induced charge follows from Gauss's theorem, this contribution can be computed analytically and imposed as a constraint during the GMRES iterations. Since $\mathcal{A}$ is real and near-symmetric, its eigenvectors are orthogonal. Thus, the physical constraint imposed in the IDS precisely eliminates contributions of the outlying eigenvalue. The remaining eigenvalues are clustered (cf. Fig. 4.3, inset), ensuring fast convergence of the IDS implementation in Fig. 4.2. Since each GMRES iteration involves evaluation of the electric field at each patch location subject to the accuracy of the Ewald solver, reduction of the number of iterations reduces the cumulative error as well.

The IDS, including the net-charge constraint, has been successfully applied to calculate the self-assembly and polarization of suspensions of binary mixtures of isotropic spherical colloids [14]. Indeed, this solver is applicable to arbitrary geometries, but the examination of the dielectric sphere has shown that subtle issues may arise. To clarify these issues in the case of dielectrically heterogeneous particles, where additional dielectric interfaces arise, I
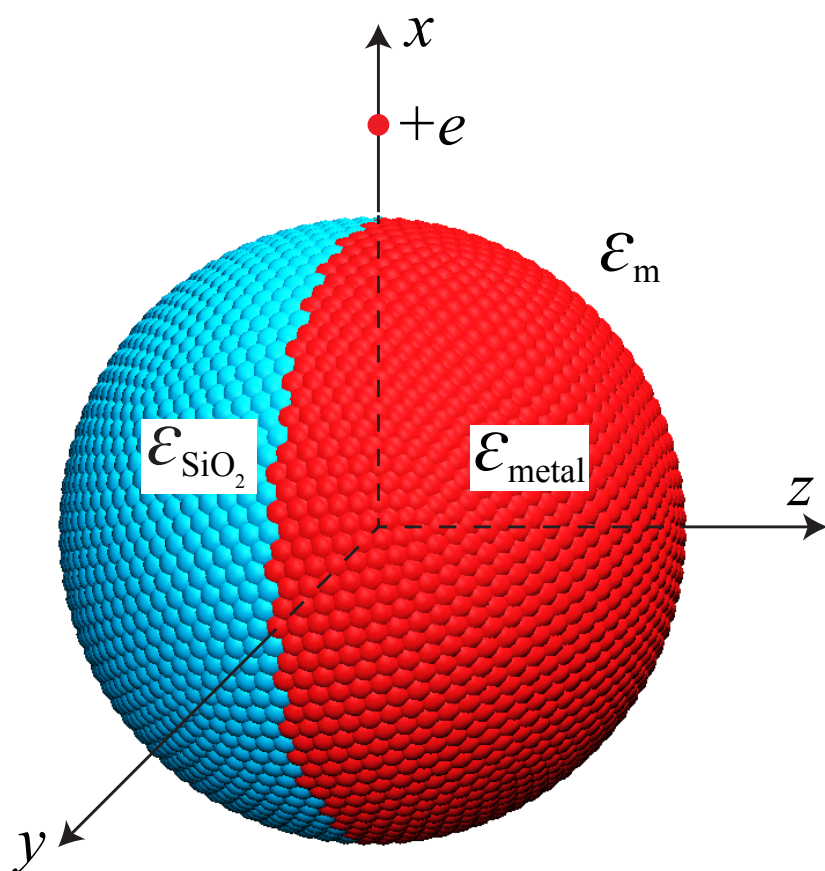
Figure 4.4. Silica/metal Janus particle of diameter 14σ (with $\sigma = 7.14$ Å). The two hemispheres are separated by a disk-shaped dielectric interface (hidden from view). As a test case of the dielectric solver applied to dielectrically anisotropic particles, I examine the surface potential induced by a positive unit charge located at $(9\sigma, 0, 0)$.

consider the prototypical example of a Janus sphere comprised of a silica hemisphere and a metallic hemisphere. This example exhibits three dielectric interfaces: two hemispherical surfaces and one equatorial disk (Fig. 4.4). The silica side has permittivity $\epsilon_{\mathrm{SiO_2}} = 4$ and the permittivity of the conducting side is approximated by $\epsilon_{\mathrm{h}} = 10^5$. The system is embedded in an uniform dielectric medium representing water ($\epsilon_{\mathrm{m}} = 80$). I set the diameter of the Janus particle to $d = 14\sigma = 10$ nm, where $\sigma = 7.14$ Å is the Bjerrum length.

To study the accuracy of the IDS, I compute the polarization charge induced on a Janus sphere by a monovalent ion and compare the resulting surface potential to a finite-element calculation performed using the COMSOL package (Version 5.1, 2015). The Janus particle has azimuthal symmetry about the z-axis. The positive unit charge is placed 9σ from its center, at a polar angle $\theta = \pi/2$ (i.e., in the equatorial plane of the Janus particle), so that the external source field acts equally on both hemispheres (Fig. 4.4). Since the IDS yields the surface charge density rather than the potential, additional errors are introduced when I back-compute the potential on each surface patch, especially for the contributions from immediately neighboring patches and from the patch itself. To reduce such errors I adopt a mesh with 10 242 patches on the sphere and 5 000 patches on the equatorial disk. The electric field is evaluated via PPPM Ewald summation, with a periodic simulation box that is large enough ($400 \times 400 \times 400\sigma^3$) to minimize periodicity artifacts. Both the relative error of the Ewald summation and the convergence criterion of GMRES are set to 10^{-6}. In the finite-element calculation, a ground potential is imposed at the boundaries of the simulation box. To suppress artifacts resulting from this, I employ the same large

simulation cell as for the BEM-based calculation. The entire 3D volume is discretized into a non-uniform mesh with $3\,147\,897$ tetrahedral elements.

Figure 4.5 compares the two approaches for the total surface potential. I plot the potential at all patch centroids as a function of their z coordinates. The red symbols show the FEM calculation, with a constant potential on the metal hemisphere ($z > 0$). The other symbols all represent BEM calculations using the IDS [2], with different conditions. These data exhibit minor deviations from the constant potential for small positive z (i.e., close to the equatorial plane), caused by discretization. More important, however, are the systematic discrepancies. If no net induced-charge constraint is imposed, the BEM data (cyan) display a strong, systematic deviation from the FEM data. For the metal hemisphere, the surface potential is almost twice higher than the correct result, and also for the silica hemisphere the potential is consistently too high. I emphasize that the data have converged, but to the incorrect result. This behavior is similar to what I observed for the isotropic sphere (Fig. 4.2), although with significantly larger deviations. Once the net induced-charge constraint is imposed (which amounts to a net-neutrality constraint in this case, as the point charge is located outside the sphere) for the entire Janus particle—i.e., for the entire system comprised of the patches on the two hemispheres as well the patches at the silica–metal interface—these deviations are significantly reduced, but by no means negligible (Fig. 4.5, blue data). The potential on the metal side is mostly constant, but still too high, and the potential on the silica side only matches the FEM calculation close to the equator.

To understand and resolve these discrepancies, I again turn to the spectrum of the operator $\mathcal{A}$. I find that the large dielectric mismatches at the metal–water interface and the
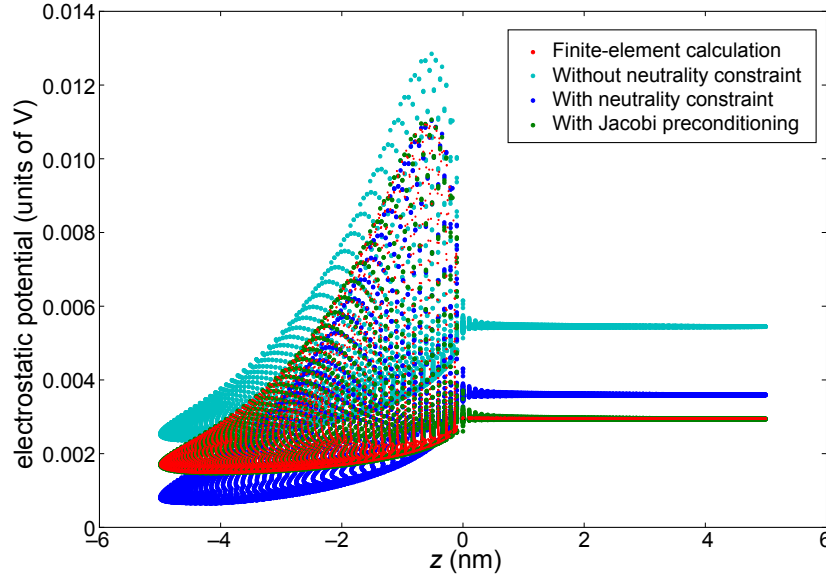
Figure 4.5. Comparison of different calculations of the total surface potential on a Janus sphere as set up in Fig. 4.4, i.e., a dielectric Janus particle embedded in water ($\epsilon_m = 80$), with a silica hemisphere ($\epsilon_{SiO_2} = 4$) and a metal hemisphere ($\epsilon_h = 10^5$), and a positive unit charge placed at $(9\sigma, 0, 0)$. The spherical dielectric interface centered at the origin has radius $7\sigma = 4.998$ nm and is divided into $10\,242$ patches on the sphere and $5\,000$ patches on the disk that constitutes the metal–silica interface. Red data points represent the surface potential as computed via a FEM calculation. The potential is constant on the metal hemisphere ($z > 0$) and varies on the silica hemisphere ($z < 0$). Cyan data are obtained with the IDS (iterative BEM-based dielectric solver) without any additional constraints. Blue data are obtained with the same solver, while constraining the net induced charge to zero. Both data sets exhibit significant deviations from the FEM solution. The green data points represent the IDS results obtained with a net-neutrality constraint as well as Jacobi preconditioning of the matrix operator. These results are obtained with negligible additional computational cost compared to a standard solver, and exhibit excellent agreement with the FEM data. See main text for a detailed discussion.
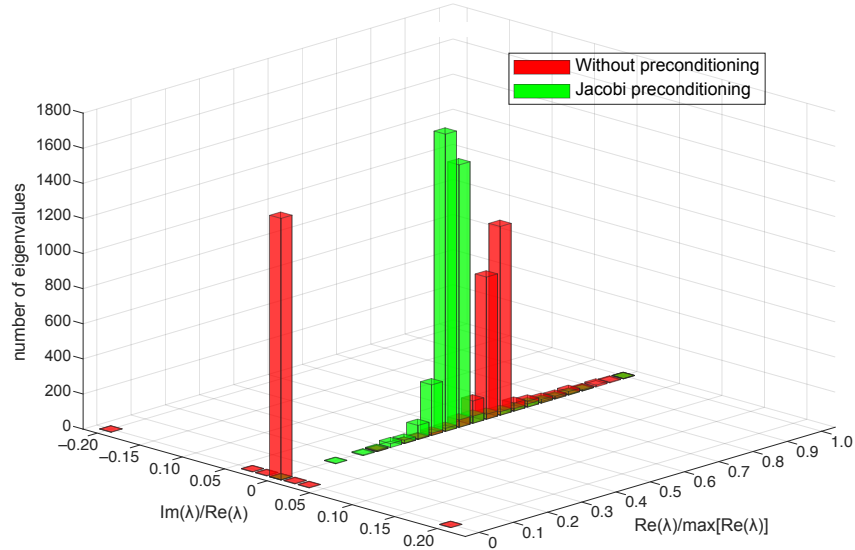
Figure 4.6. Comparison between the scaled spectra of the matrix $\mathcal{A}$ for a Janus particle (Fig. 4.4) with Jacobi preconditioning (green data) and without preconditioning (red data). The x-axis is scaled by the maximum of the real part of all eigenvalues. The y-axis gives the ratio between the imaginary and real parts of each eigenvalue.

central metal–silica interface have a detrimental effect on the condition number, yielding $\kappa(\mathcal{A}) = 2.93 \times 10^3$. Moreover, as illustrated in Fig. 4.6 (red data), the spectrum exhibits two groups of normalized eigenvalues, clustered around 0 and 0.65, respectively, resulting in slow convergence. The anisotropy of the Janus particle also results in an asymmetric matrix and significant imaginary parts for some of the eigenvalues, hindering numerical solution of the matrix equation [125]. To improve this, I apply a preconditioner $\mathcal{M}$ to transform the matrix equation [123], $\mathcal{M}^{-1}\mathcal{A}\boldsymbol{\sigma} = \mathcal{M}^{-1}\mathbf{b}$. The choice $\mathcal{M} = \mathcal{A}$ would yield perfect spectral properties, but is prohibitively costly in situations where $\mathcal{A}$ is dynamic. Instead, we observe that the simple Jacobi (or diagonal) preconditioner $\mathcal{M} = \mathrm{diag}(\mathcal{A}) = \mathrm{diag}(\bar{\epsilon}_{ii})$, can be applied here. It is efficient for diagonally dominant matrices [123], as confirmed by the modified spectrum (Fig. 4.6, green data). With the Jacobi preconditioning, the

condition number drops 46-fold to 63.7, and the scaled eigenvalues are clustered around 0.50. These improvements are reflected in the corresponding results for surface potential (Fig. 4.5, green data), which are in excellent agreement with the FEM calculations. Intuitively, this preconditioning remedies the disproportionate weight of patches with large prefactors in Eq. (4.8), i.e., large $\bar{\epsilon}_i$ and $\Delta\epsilon_i$ in the residual—precisely the situation that arises if multiple dielectric mismatches are present. This method of preconditioning can be implemented in a particularly simple manner, namely in each iteration of GMRES the residual of the ith patch is normalized by $\bar{\epsilon}_{ii}$.

4.3. Conclusion

In summary, these results demonstrate that a combination of high accuracy in the electrostatic summation, a strict convergence criterion in the GMRES method, and a fine discretization level in the BEM are *insufficient* to guarantee correctness of polarization charge calculations. Given how widely the BEM is adopted in dielectric simulations, unawareness of effective techniques can be problematic. I find that with proper preconditioning to reduce the matrix condition number for systems with multiple dielectric contrasts and a physical (net induced-charge) constraint to eliminate the effects of outlying eigenvalues in the operator spectrum, the iterative dielectric solver of Ref. 2 is capable of accurately and efficiently resolving induced charge in systems with multiple dielectric contrasts. A crucial observation is that the preconditioning proposed here can be achieved at no additional computational cost. This is essential for situations where the dielectric environment is time-dependent, such as in dynamical simulations of colloids, proteins, etc., and thus the induced charges must be resolved with the highest possible efficiency.

For simplicity, I have focused on the prototypical Janus geometry. However, the techniques to improve the spectrum of the BEM matrix are general and can be applied to a broad variety of dielectric systems [108].

CHAPTER 5

Application of the refined IDS to Janus colloids

The content of this chapter is based on the following publications:

- Huanxin Wu, Ming Han, and Erik Luijten, Dielectric effects on the ion distribution near a Janus colloid, *Soft Matter*, **12**, 9575–9584 (2016).
- Ming Han, Huanxin Wu, and Erik Luijten, Electric double layer of anisotropic dielectric colloids under electric fields, *Eur. Phys. J. Special Topics*, **225**, 685–698 (2016).

The finite–element calculation in Sec. 5.2.2 is performed by Ming Han.

5.1. Introduction

Many phenomena of interest occur at colloidal interfaces, where the dielectric mismatch between the solvent and the colloid gives rise to induced surface (polarization) charge, which is analytically complicated and computationally expensive to solve. Whereas current experimental techniques face limitations in measuring these interfacial properties at a molecular level, computer simulations can offer much insight. For isotropic colloids, the polarization effects on the ionic density profile near colloidal surfaces are well-studied via simulations and have been shown to be significant [12, 24, 100, 126]. Such effects on the structure of the electric double layer (EDL) surrounding a colloid may have consequences for many properties, such as surface ionization and complexation, chemical reactions, and electrophoretic mobility [127].

Recently, particles with anisotropic surface properties have attracted strong interest due to their promise for applications in photonic materials, electronics, electrokinetics, and drug delivery [128]. One of the simplest patchy geometries is the Janus particle, which comprises two domains of different materials [129, 130]. There are many possible design choices for the mismatch between these domains [131], including dipolar [132, 133], charged/hydrophobic [134, 135], or charged/magnetic [136], resulting in a variety of self-assembled structures [133, 137, 134, 136]. Current large-scale fabrication techniques can produce Janus particles with controllable sizes and geometries [129]. One of the methodologies for creating spherical Janus colloids is the application of a partial coating of a different material on a spherical colloid. The resulting dielectric heterogeneity in the particle is crucial for a variety of phenomena, including the well-known induced-charge electrophoresis [138]. Yet, owing to a lack of efficient modeling methods, most computer simulation studies ignore the polarization of Janus particles by the electrolyte [133, 139, 140, 141, 142].

For complicated geometries like Janus particles, boundary-element method (BEM)-based dielectric solvers offer advantages in convenience, capability, and efficiency [69]. Instead of solving Poisson's equation on a three-dimensional grid, the BEM only discretizes dielectric interfaces and solves the surface induced charge explicitly. Here, I apply the approach introduced in Refs. 2, 14 to investigate the ionic distribution around a Janus colloid via molecular dynamics simulations, in which the induced charges at dielectric interfaces are computed dynamically. I also adopt preconditioning techniques that can

significantly improve the accuracy and efficiency for systems with multiple dielectric contrasts [143]. This method has been successfully applied to study the EDL of anisotropic dielectric colloids under external electric fields [108].

This chapter is organized as follows. First, details of my simulation model are provided in Sec. 5.2.1. After examining the effects of Janus particle coating thickness in Sec. 5.2.2 I proceed to apply the IDS to examine the structure of symmetric and asymmetric electrolytes near two types of neutral Janus colloids (silica/silicon and silica/metal) in Sec. 5.3.1. Following that, Sec. 5.3.2 presents simulation results for the counterion distribution around various charged Janus colloids in both salt-free and electrolyte environments. I address the effects of colloid size and and ion radius in Sec. 5.3.3. I conclude the chapter with a brief summary in Sec. 5.4.

5.2. Methods and model

5.2.1. Molecular dynamics simulation model

To study dielectric effects on the EDL, I investigate a single dielectric Janus colloid of valence Z immersed in an aqueous electrolyte. The Janus sphere is comprised of two hemispheres of different materials and exhibits three dielectric interfaces: two hemispherical surfaces and one equatorial disk (Fig. 5.1). The particle has azimuthal symmetry about the z-axis. I consider two representative types of dielectrically heterogeneous Janus colloids. The first type consists of hemispheres made of silica ($\epsilon_{\mathrm{SiO_2}} = 4$) and silicon ($\epsilon_{\mathrm{Si}} = 12$), respectively. The second type has a silica hemisphere and a metal hemisphere, where the conducting side is approximated by a high permittivity $\epsilon_{\mathrm{h}} = 10^5$. The system is embedded in water ($\epsilon_{\mathrm{m}} = 80$). The spherical BEM mesh, i.e., the dielectric interface
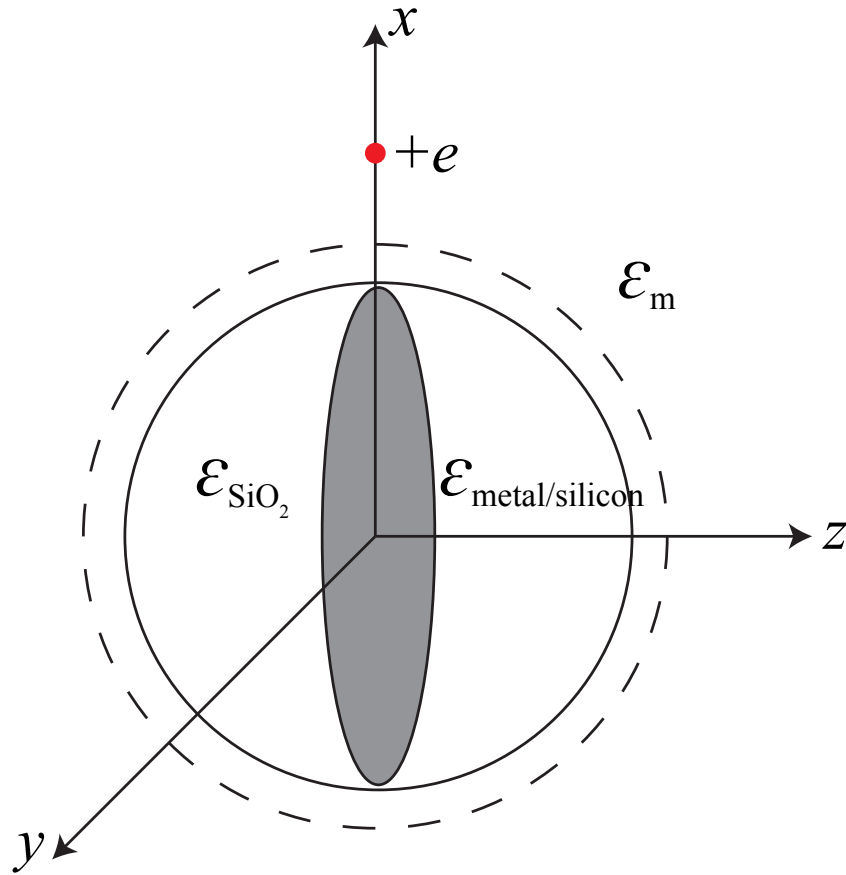
Figure 5.1. A silica/metal Janus particle (solid circle) comprised of two hemispheres that are separated by a disk-shaped dielectric interface (shaded region). To ensure that mobile external charges (ions) do not approach the particle surface—i.e., the dielectric interface separating the hemispheres from the surrounding medium—too closely, it is surrounded by a concentric spherical surface (dashed circle). This outer surface is modeled via a soft repulsive potential (cf. main text). The dielectric sphere has a diameter 14σ (with $\sigma = 7.14$ Å), whereas the effective diameter of the particle is 15σ (i.e., the dielectric interface is located 0.5σ below the effective particle surface). As a test case for the effects of coating thickness (Sec. 5.2.2), we examine the surface potential induced by a positive unit charge located at $(9\sigma, 0, 0)$.

between the water and the particle, has a radius $R = 7\sigma$, where $\sigma = 7.14$ Å is the Bjerrum length of water at room temperature. To prevent the ions from penetrating the BEM mesh, this dielectric interface is placed inside a concentric soft repulsive shell, modeled by a shifted-truncated Lennard-Jones (LJ) potential described below. As a result, the Janus particle has an effective diameter $d = 15\sigma = 10.71$ nm. As this is far smaller than the particle sizes typically employed in experiment, I systematically examine the effect of colloid size on our results in Sec. 5.3.3. Since the Janus particle is much larger than the ions, I only discretize the dielectric interfaces of the Janus particle, i.e., I ignore anisotropic polarization charge distribution on the hydrated ions [144]. This approximation implies that I also ignore the corresponding charge–dipole and dipole–dipole interactions between ions, as well as dielectrophoretic forces. Another simplification concerns the permittivity of the electrolyte solution, which is known to decrease with increasing ion concentration [145]. Capturing this effect requires solving the spatial and time-dependent *bulk* polarization, which goes beyond the assumption of sharp dielectric interfaces adopted here, but will be addressed in future work.

For the BEM mesh, the central disk is discretized into 183 patches and the spherical dielectric interface into 732 patches. These 732 patches are then assigned to either hemisphere, depending on the position of their center. Owing to my choice for the orientation of the mesh, this results in 363 and 369 patches belonging to either side, respectively. The Janus colloid is fixed at the center of a periodic cubic simulation box $(30 \times 30 \times 30\sigma^3)$, and is surrounded by hydrated ions that are represented as spheres of diameter σ. For the systems investigated, the Debye length is smaller than $1/10$ of the simulation box size, so that artifacts due to periodic images are negligible.

The electrostatic interactions are taken into account via PPPM Ewald summation, with a relative accuracy of 10^{-4} [146, 45]. Excluded-volume interactions between particles i and j are modeled via an expanded shifted-truncated Lennard-Jones (LJ) potential,

$$(5.1) \quad u_{\mathrm{LJ}}(r_{ij}) =$$

$$\begin{cases} \infty & r_{ij} \leq \Delta_{ij} \\ 4k_{\mathrm{B}}T \left[\left(\frac{\sigma}{r_{ij}-\Delta_{ij}} \right)^{12} - \left(\frac{\sigma}{r_{ij}-\Delta_{ij}} \right)^{6} + \frac{1}{4} \right] & \Delta_{ij} < r_{ij} < \Delta_{ij} + 2^{\frac{1}{6}}\sigma \\ 0 & r_{ij} \geq \Delta_{ij} + 2^{\frac{1}{6}}\sigma \end{cases} \quad ,$$

where $\Delta_{ij} = (d_i + d_j)/2 - \sigma$ is the hard-core distance, with d_i and d_j the diameters of particles i and j. Whereas this potential diverges at $r_{ij} = \Delta_{ij}$, the repulsive interaction already equals the thermal energy at $r_{ij} = \Delta_{ij} + \sigma = (d_i + d_j)/2$. According to Ref. 2, the average patch–patch separation must be chosen smaller than the minimum ion–patch distance, to suppress discretization effects. In my system, the closest ion–colloid separation is $r = 8\sigma$, which allows a surface discretization with an average patch–patch separation of approximately σ.

To investigate the EDL structure, I perform MD simulations of the ions surrounding the colloid. Depending on the system configuration, 232 to 867 ions are involved. To introduce thermal fluctuations, a Langevin thermostat is applied to the ions, with damping parameter $20t_0$, where $t_0 = (m\sigma^2/k_{\mathrm{B}}T)^{1/2}$ is the LJ unit time with m the ionic mass, keep the system at room temperature ($T = 298$ K). The resultant Bjerrum length $l_{\mathrm{B}} = e^2/(4\pi\epsilon_0\epsilon_{\mathrm{m}}k_{\mathrm{B}}T) = \sigma = 7.14$ Å coincides with the ion size. Each simulation starts from a random ion configuration. After an equilibration period of 2500 t_0, I sample the ion

distribution over 150000 time steps with 200 to 600 independent runs for each parameter set, which yields 2×10^5 to 6×10^5 independent samples.

5.2.2. Effects of coating thickness

In many experiments, dielectrically anisotropic Janus colloids are created by deposition of a thin metal coating [136, 138], as opposed to the evenly divided model of Fig. 5.1. To confirm that our model properly captures the polarization effects of a Janus particle generated by coating, my collaborator and I examine the effects of coating thickness of a silica/metal Janus particle via finite-element calculation using COMSOL (Version 5.1, 2015), a commercial finite-element code. Under the same system setup as described in the previous section (i.e., Janus director oriented along the z axis), in the absence of electrolyte, we place a positive external point charge in the equatorial plane and $\delta = 2\sigma$ away from the dielectric interface (Fig. 5.1). We consider a silica sphere with one hemisphere coated by metal. The coating thickness is parametrized by its ratio t with respect to the (dielectric) radius $R = 7\sigma$. To ensure high accuracy and a smooth surface potential, we mesh the system with more than 3×10^6 tetrahedral elements. As illustrated in Fig. 5.2, the surface potential depends strongly on thickness only for very thin coatings, starting to saturate already at $t \sim 0.01$—thinner than the coating applied in most experiments. Thus, to a good approximation, we can model the Janus colloids as evenly divided spheres, with results that also represent the dielectric response of Janus particles with surface coatings.

The surface potential shown in Fig. 5.2 is the sum of the source potential of the unit charge and the image potential induced by this charge. Whereas the charge is equidistant to both hemispheres, their dielectric response is very different. It is also informative to
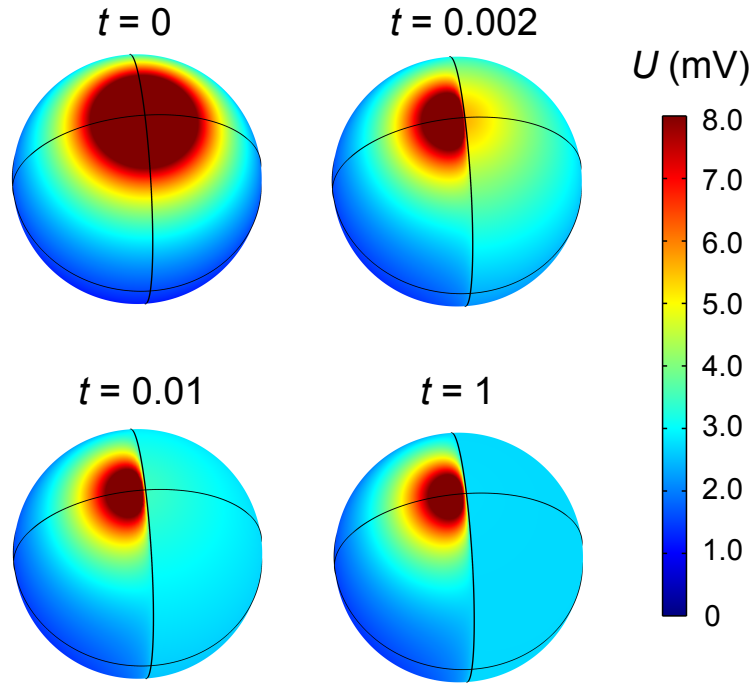
Figure 5.2. Surface potential of a silica (left)/metal (right) Janus sphere induced by an external unit charge, for four different thicknesses of the metal coating: $t = 0$ (a pure silica sphere), 0.002, 0.01, and 1 (evenly divided Janus sphere), where t is the ratio between coating thickness and particle radius. The orientation of the Janus particle and the location of the charge are the same as in Fig. 5.1. Although the potential is thickness dependent, it has nearly saturated for a thickness of 1% ($t = 0.01$). The potential on the right-hand side of the colloid becomes uniform, as expected for a metal.
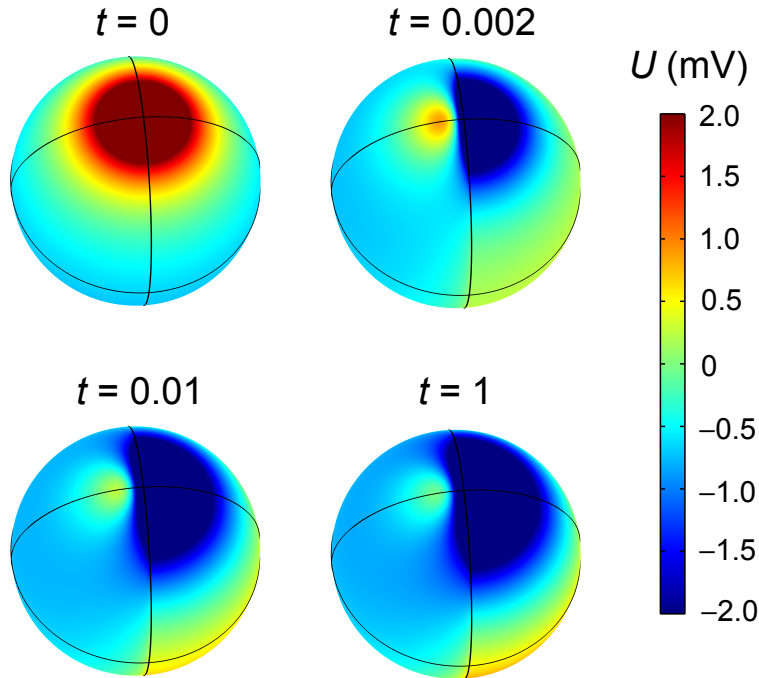
Figure 5.3. *Image potential* of the same system as depicted in Fig. 5.2, i.e., a silica (left)/metal (right) Janus sphere and an external unit charge, with 4 different metal coating thicknesses. The potential shown here is solely due to the electric charges induced on the colloidal surface.

compare the surface potential to the image potential, shown in Fig. 5.3, solely arising from the induced electric charges on the colloidal surface. It illustrates, e.g., how the constant surface potential on the metal hemisphere (Fig. 5.2, for $t \gtrsim 0.01$) arises from the image potential that varies with the polar angle and from the equally varying source potential.

5.3. Results

5.3.1. Electrolyte near a neutral dielectric Janus colloid

I first consider a neutral Janus dielectric colloid ($Z = 0$, no counterions) embedded in an aqueous electrolyte. Here, all electrostatic interactions between the Janus colloid and the
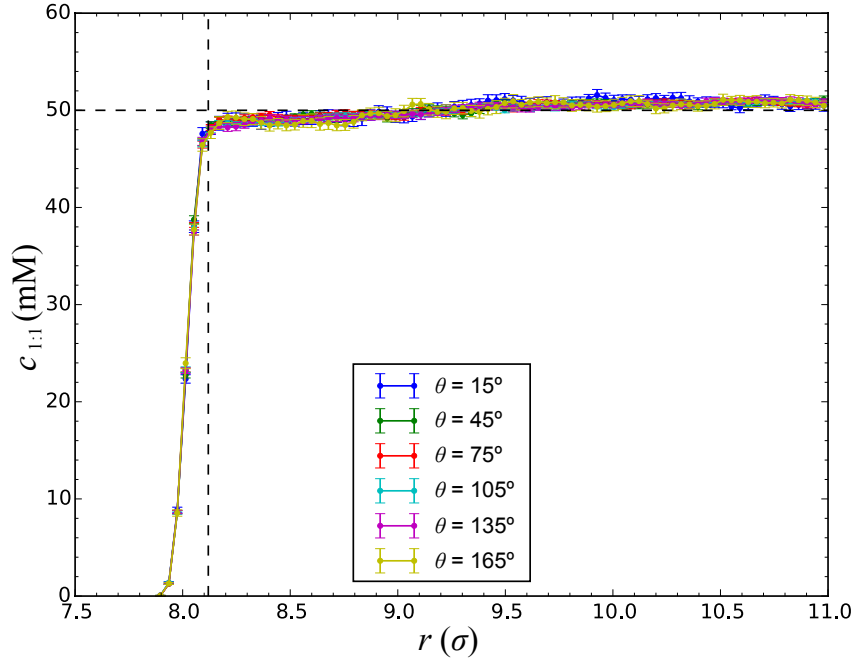
Figure 5.4. Ionic density distribution $c(r, \theta)$ of 50 mM monovalent aqueous salt around a silica/silicon Janus colloid at various θ, where θ is the polar angle with respect to the symmetry axis of the Janus colloid, i.e., $0 \leq \theta < 90°$ refers to the silicon hemisphere and $90° < \theta \leq 180°$ to the silica hemisphere. For each θ, the ion concentration is averaged over $[\theta - 1.5°, \theta + 1.5°]$. The dashed horizontal line marks the bulk concentration and the dashed vertical line marks the LJ interaction cutoff distance. Whereas the relative permittivities of both materials differ by a factor 3, their dielectric contrast with the surrounding medium is comparable, so that the ion distribution shows no θ dependence.

ions are purely due to polarization charges induced on the colloid. This allows us to isolate the dielectric response and compare the double layer around Janus colloids with different dielectric contrasts. I note that an ion of valence z located on the lower permittivity side of a dielectric interface induces an *attractive* polarization charge proportional to z, and vice versa. Thus, the dielectric interaction is proportional to z^2.

5.3.1.1. Symmetric monovalent salt. For the silica/silicon Janus colloid, dielectric effects are repulsive for both hemispheres, since $\epsilon_{SiO_2} < \epsilon_{Si} < \epsilon_m$. As the system exhibits
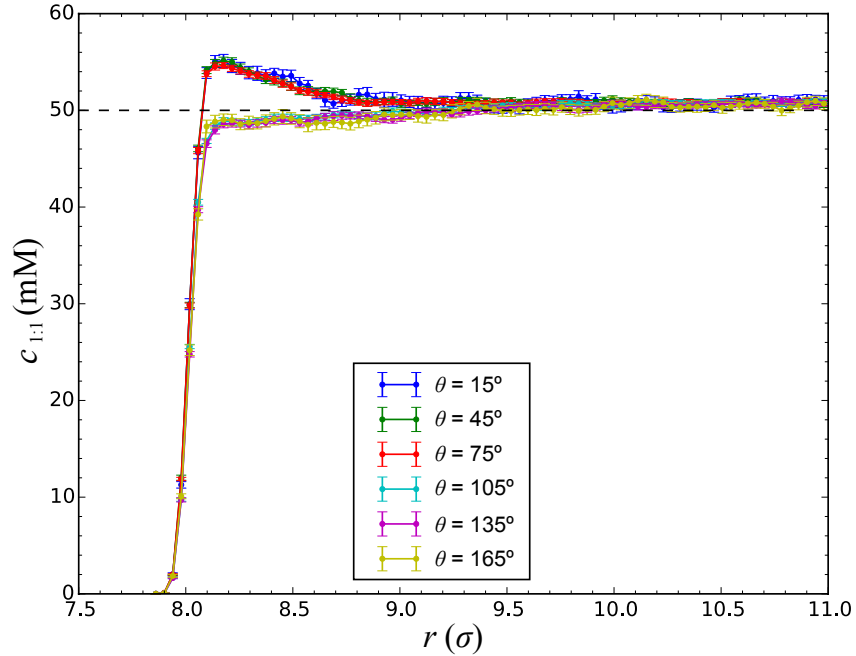
Figure 5.5. Ionic density distribution $c(r,\theta)$ of 50 mM monovalent salt around a single silica/metal Janus colloid at various polar angles θ. The metal side corresponds to $0 \leq \theta < 90°$, whereas the silica side corresponds to $90° < \theta \leq 180°$. For each θ, the ion concentration is averaged over $[\theta - 1.5°, \theta + 1.5°]$. The dashed horizontal line marks the bulk concentration. Due to the induced polarization charges, the ions aggregate around the metal hemisphere and are depleted on the silica side.

azimuthal symmetry around the z-axis (Fig. 5.1), I calculate the ionic density distribution $c(r,\theta)$. As illustrated in Fig. 5.4, I indeed observe a very weak depletion region near both hemispheres beyond $r_c = 8.12\sigma$ (dashed vertical line), where the LJ interactions vanish, due to dielectric repulsion. Even though the two hemispheres differ by a factor 3 in dielectric mismatch ($\epsilon_{Si} = 3\epsilon_{SiO_2}$), no clear dependence on the polar angle θ is observed. Thus, in this case the Janus colloid behaves similar to an isotropic colloid, simply because the dielectric contrast with the surrounding medium $\Delta\epsilon/\bar{\epsilon}$ [cf. Eq. (2.4)] differs only by 20% for the two materials.

The situation becomes more interesting when the two hemispheres have opposite dielectric responses. For a silica/metal Janus colloid, the silica side is repulsive to ions whereas the metal side is attractive. This is reflected in the ionic density distribution (Fig. 5.5), with a notable accumulation of ions near the metal hemisphere. The interference between the metal and the silica hemispheres is very small, as $c(r, \theta)$ on the silica side is indistinguishable from that in Fig. 5.4. An interesting consequence of the anisotropic ion distribution is the presence of a net entropic force of strength $(-0.87 \pm 0.03 \ k_\mathrm{B}T/l_\mathrm{B})$, oriented along the symmetry axis (director) of the silica/metal Janus particle and pointing towards the silica side. Energy conservation requires that this force, arising from the imbalanced (purely repulsive) excluded-volume LJ interactions between ions and the colloidal surface, be counteracted by other interactions. Indeed, I find that the electrostatic interactions between the ions and the induced surface charge give rise to a net electrostatic force $(0.8971 \pm 0.0007 \ k_\mathrm{B}T/l_\mathrm{B})$, directed towards the metal side.

Although the dielectric effects are stronger for the silica/metal Janus colloid, $c(r, \theta)$ is still independent of θ for angles belonging to the same hemisphere. Thus, to a good approximation, one could use the angular average of the distribution over each hemisphere to characterize the system. Since the silica/silicon Janus colloid closely resembles an isotropic dielectric colloid, which has been well studied [12], from now on I focus on the silica/metal Janus colloid.

5.3.1.2. Asymmetric salt. Asymmetric 2:1 and 3:1 salts, such as $MgCl_2$ and $AlCl_3$, are widely used in chemical systems. As noted above, multivalent ions experience quadratically stronger dielectric repulsion and attraction than monovalent ions, giving rise to a

symmetry breaking near interfaces where a jump occurs in the relative permittivity. Figures 5.6a and 5.6b illustrate this for the spatially varying ion concentration of a 2:1 salt (bulk concentration 50 mM) around a silica/metal Janus particle. The divalent cations (Fig. 5.6a) are strongly concentrated at the metal side while depleted at the silica side. However, for the monovalent anions (Fig. 5.6b), which have a four times smaller image potential energy, this imbalance is much weaker. Thus, although in the bulk the cation concentration C_{2+} is obviously half of the anion concentration C_{1-}, close to the silica hemisphere I find $C_{2+}/C_{1-} < \frac{1}{2}$, resulting in a net negative ionic charge density (Fig. 5.6c). Similarly, a positive ionic charge density is observed at the metal side. This net ionic charge density close to the colloidal surface decreases near the transition between the two hemispheres ($z = 0$).

Although the net charge of the ion layers near the two hemispheres is opposite in sign, I anticipate that the difference in permittivity of the hemispheres causes *both* layers to induce negative polarization charges. This is confirmed in Fig. 5.7a, where both the metal surface and the silica surface are negatively charged but with different surface charge density. However, the net induced charge on the colloid must vanish, and accordingly I observe a ring of positive charges at the equator of the Janus particle, where *three* domains of different relative permittivity meet. A consequence of the polarization charge distribution on the colloid is that the particle and its associated ion cloud studied in Fig. 5.6 acquire an effective dipole moment when immersed in an asymmetric electrolyte.

Another interesting observation is that the fluctuations in the induced charges are rather different for the two hemispheres (Fig. 5.7b). This can be attributed to the fact
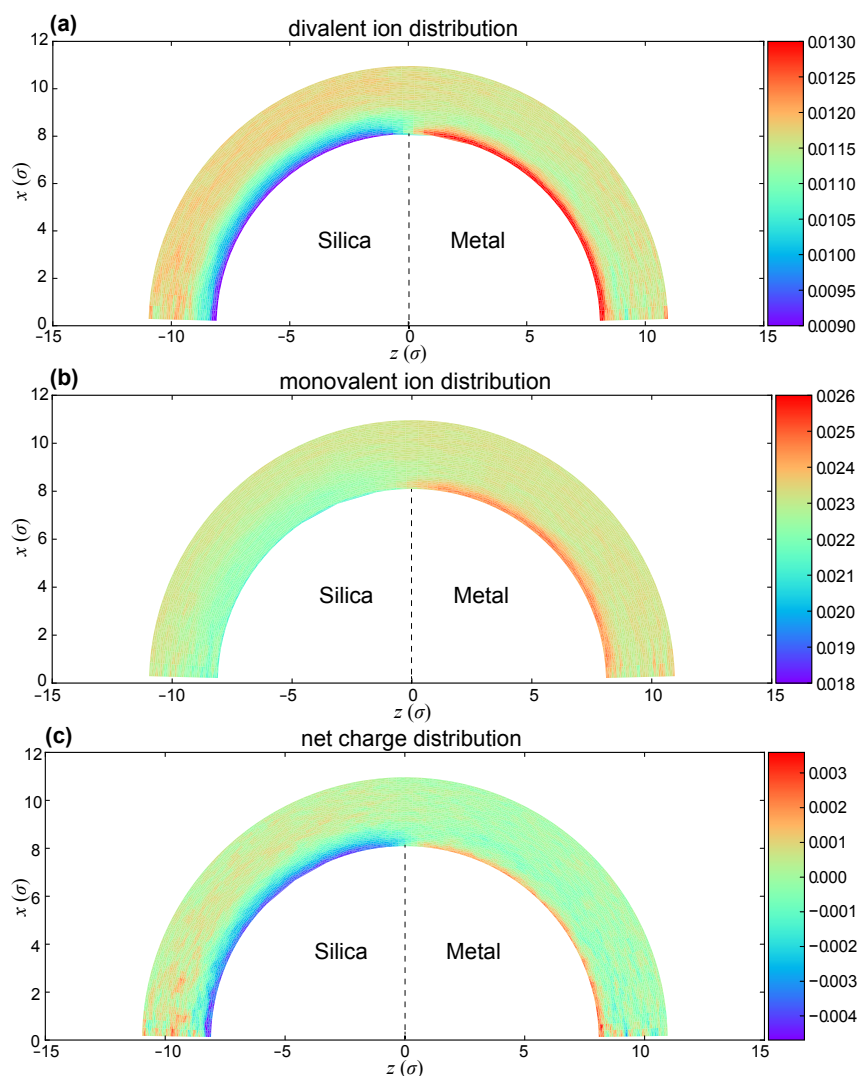
Figure 5.6. Ion number density (σ^{-3}) distribution of a 2:1 electrolyte around an isolated silica/metal Janus colloid. The bulk concentration of 50 mM corresponds to $0.0110\sigma^{-3}$ for divalent ions and $0.0220\sigma^{-3}$ for monovalent ions. (a) Divalent cation density distribution, enhanced near the metal surface and suppressed near the silica surface; (b) monovalent anion density distribution, with significantly lower enhancement and suppression; (c) net ionic charge density distribution, negative near the silica hemisphere and positive near the metal hemisphere.
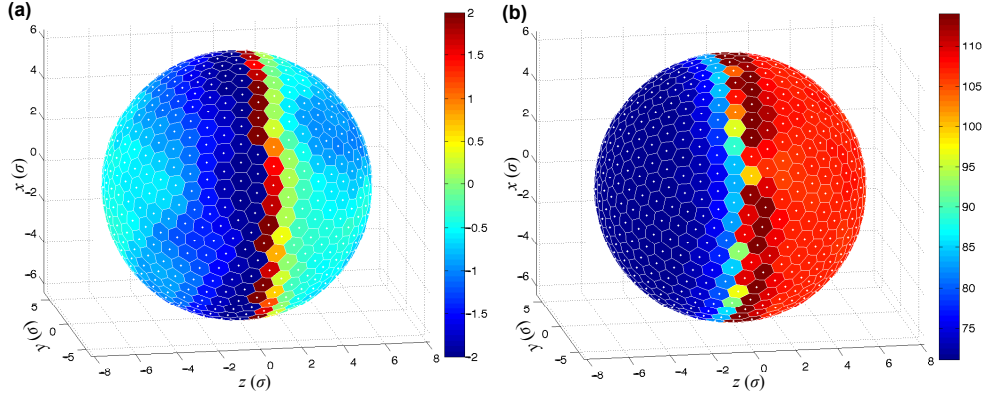
Figure 5.7. (a) Net polarization charge density and (b) its standard deviation induced on a single silica/metal Janus colloid by 50 mM 2:1 electrolyte. Both the magnitude and the standard deviation are in units $10^{-5}e/\sigma^2$. Note how the fluctuations by far exceed the magnitude of the induced charge.

that ions are more likely to interact with the dielectrically attractive metal hemisphere than with the repulsive silica hemisphere.

5.3.2. Counterion distribution near a charged dielectric Janus colloid

The situation changes when the Janus colloid also carries a *free* surface charge. Then, it will attract counterions from the solution that will form an electric double layer at the spherical surface. These ions interact with their induced charges on the Janus colloid as well as with the surface free charges. I am particularly interested in a strength comparison between the dielectric interactions and the intrinsic free-charge interactions.

5.3.2.1. Uniformly charged Janus colloid. I first consider an isotropically charged silica/metal Janus colloid of $Z = -60$ (-30.6 mC/m^2) surrounded by counterions (monovalent, $z = 1$, or divalent, $z = 2$) only. Figure 5.8a shows the monovalent counterion density distribution. Although, just as for the silica/metal Janus particle in Fig. 5.6, dielectric effects attract the counterions to the metal side and repel them from the silica side,

the attraction between the counterions and the surface free charges is so strong that it overwhelms the dielectric effects, resulting in little contrast between the two hemispheres. However, for divalent counterions the dielectric effects are sufficiently strong to produce a noticeable difference between the two hemispheres (Fig. 5.8b). This observation is consistent with a quick estimation of the interaction energies. The potential energy of a z-valent ion interacting with the free charge on the Janus colloid is $\frac{zZl_B}{r}k_BT = -7.5zk_BT$, where I have set $r = 8\sigma$ at contact and $l_B = \sigma$. The absolute interaction energy of such an ion with its induced polarization charge is $|E_p| < |\frac{\Delta\epsilon}{\epsilon}|\frac{z^2l_B}{2(r-7\sigma)}k_BT \approx \frac{1}{2}z^2k_BT$, where the upper limit corresponds to a planar geometry and $|\frac{\Delta\epsilon}{\epsilon}| \approx 1$ for both hemispheres, but opposite in sign. Thus, for monovalent counterions the difference in image potential energy between the silica and metal hemispheres is approximately $2|E_p| \approx k_BT$ and the total attraction experienced by the ions (including the effect of free charge) is quite similar. However, for divalent counterions the difference in image potential energy is approximately $4k_BT$, as borne out by Fig. 5.8b.

Generally, the addition of salt is expected to diminish dielectric effects. To examine this, I also study the system with 20 mM and with 50 mM additional monovalent salt. These salt concentrations correspond to Debye lengths of 21.5 Å (3.01σ) and 13.6 Å (1.90σ), respectively. Here I focus on the divalent counterion system. As illustrated in Fig. 5.9, compared to a salt-free environment, the divalent counterions become less concentrated near the colloidal surface with increasing salt concentration. This weakened binding simply reflects the screening of the surface charge by the salt. However, the location of the maximum in the counterion density is almost independent of the salt concentration, as it is determined by short-range excluded-volume effects. Moreover,
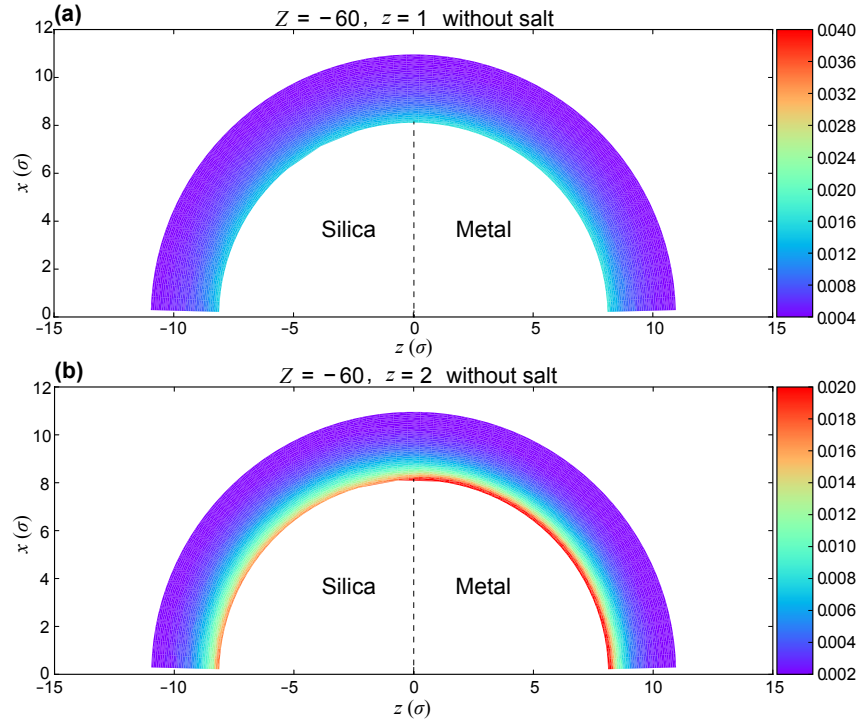
Figure 5.8. Counterion distribution around a uniformly charged ($Z = -60$) dielectric silica/metal Janus colloid. The concentration is expressed as the number density (units of σ^{-3}) and no additional salt is present. For monovalent counterions (a), there is no discernible difference in the concentration between the two hemispheres, as the free surface charge overwhelms the dielectric effects. However, for divalent counterions (b) these effects are far stronger and the distribution becomes asymmetric. See main text for a quantitative discussion.

taking the *ratio* of the peak heights for the metal and the silica hemispheres as a measure of the dielectric effects, I observe that this ratio is essentially constant at 1.4 for the three salt concentrations—showing that the relative effects of the dielectric mismatch are not diminished by salt at the concentrations examined here. In fact, this ratio is directly related to the binding energy difference for divalent ions between the metal and the silica hemispheres. Based upon our previous estimation, the interaction energy between a divalent ion and the free charge on the Janus colloid at contact is $-15k_\mathrm{B}T$, while the image potential energy is $\pm 2k_\mathrm{B}T$ on the silica and the metal side, respectively, which gives an energy ratio of $17/13 \approx 1.31$.

5.3.2.2. Anisotropically charged Janus colloid. In reality, a mismatch in dielectric properties typically implies a difference in surface chemistry as well, and the free-charge distribution on the surface of a Janus colloid may be anisotropic. For example, in water a silica surface will be negatively charged due to ionization [147], whereas a metal surface would generally be minimally charged. Here, I examine how this additional anisotropy affects the equilibrium structure of the EDL. I consider a silica/metal Janus colloid immersed in a 20 mM 1:1 electrolyte. The typical surface charge density of an ionized silica particle is $\mathcal{O}(1)$ mC/m^2 in aqueous solutions with a pH spanning from 4 to 8 and with electrolyte concentrations ranging from 5 mM to 0.3 M [148]. Accordingly, I set the total free surface charge on the silica side to $2e^-$ or $10e^-$ (-2.04 mC/m^2 or -10.2 mC/m^2, respectively), while keeping the metal side neutral. Since the ionization of silica is an equilibrium process in which silanol groups that are randomly distributed over the surface dynamically dissociate and reassociate, I spread the free surface charge uniformly across
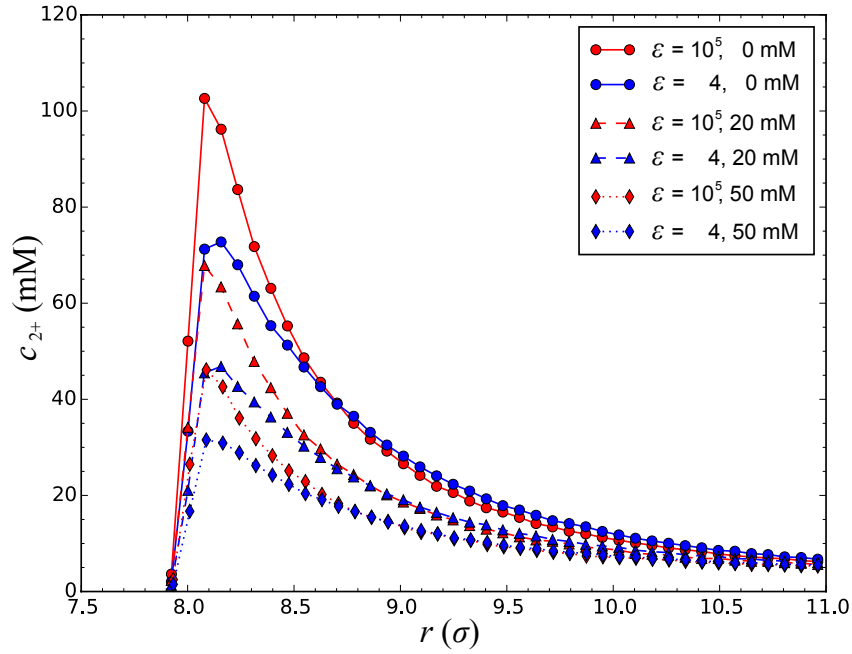
Figure 5.9. Effect of salt on the density distribution of divalent counterions around a uniformly charged ($Z = -60$) silica/metal Janus colloid. Data are angularly averaged for each hemisphere (red: metal, blue: silica). As the concentration of 1:1 salt increases from salt free (circles, solid lines), to 20 mM (triangles, dashed lines) to 50 mM (diamonds, dotted lines), the colloid charge becomes increasingly screened and the accumulation of the counterions decreases. However, the effect of the dielectric mismatch between both hemispheres remains, with a near-constant ratio between the peaks in the concentrations around the metal hemisphere and the silica hemisphere.

the silica hemisphere to represent the thermal average. All the counterions in this system are monovalent.

For surface charge density -2.04 mC/m^2 on the silica hemisphere (triangular symbols in Fig. 5.10), the repulsive dielectric effects at the silica surface overwhelm the attraction from its surface free charge, leaving a weakly depleted region of counterions on the silica side. At the same time, the dielectrically attractive metal side exhibits an accumulation of counterions. Thus, apart from the difference in global salt concentration, this distribution essentially mimics the one in Fig. 5.5 (Sec. 5.3.1.1). This demonstrates that the EDL can be strongly altered by dielectric effects for realistic ionization states. However, when I increase the silica surface charge density to -10.2 mC/m^2 (circular symbols in Fig. 5.10), this hemisphere shows strong counterion accumulation, significantly surpassing the metal side. In fact, compared to the case with lower surface charge density, even the metal side exhibits a slight enhancement in the counterion density. This is due to the attraction from the negative free charges on the opposing (silica side) as well as the negative charges they induce on the metal surface.

5.3.3. Size effects

5.3.3.1. Colloidal size effects. Although the Janus colloid modeled in this paper is larger than in earlier simulations of dielectrically isotropic spheres [99], it is still at least an order of magnitude smaller than particles used in most experiments. To verify that my findings apply to realistic particles, I revisit the divalent counterion distribution case of Sec. 5.3.2.1 with 20 mM 1:1 salt, and consider a Janus colloid with the same surface charge density as before, but four times larger diameter. To maintain the discretization
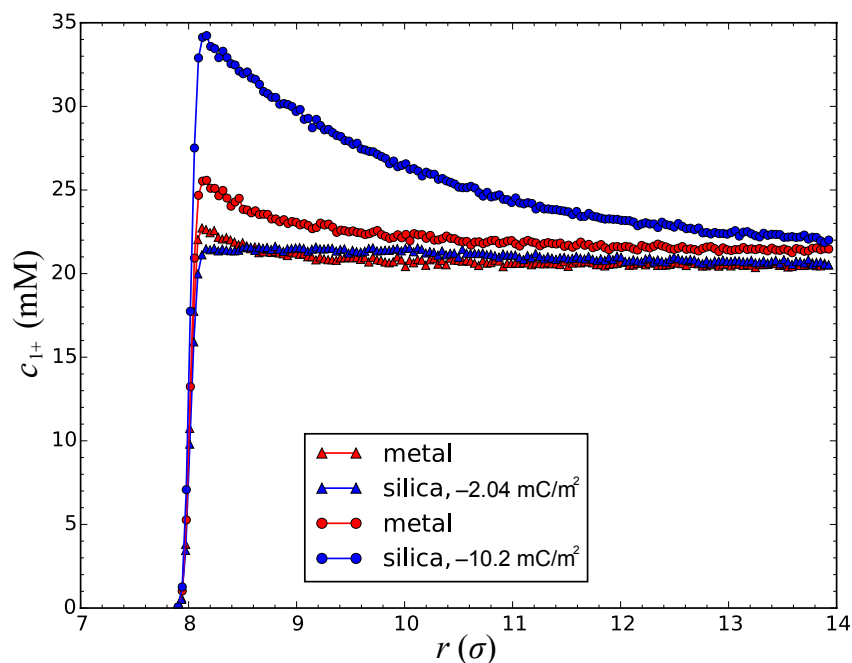
Figure 5.10. Effect of anisotropic surface charge on the density distribution of monovalent counterions. The silica/metal Janus colloid is immersed in a 20 mM 1:1 electrolyte. The metal hemisphere carries no free charge (although it can acquire a polarization charge), whereas the silica hemisphere carries a uniform free surface charge density of either $2e^-$ (triangles) or $10e^-$ (circles). Curves show the concentration of positive ions around either hemisphere, angularly averaged. For low free charge density on the silica surface, the attractive polarization charge (induced by ions) on the metal side dominates, but once the surface charge on the silica hemisphere is increased, the electric double layer becomes concentrated on that side. Interestingly, even the ion concentration on the metal side is slightly increased by the free charges on the silica hemisphere. For consistency, I note that the enhancement of positive ions around *both* hemispheres above the bulk concentration is quantitatively consistent with the number of excess counterions present.

accuracy in the IDS, the number of surface patches is increased by a factor 16. Moreover, to permit extrapolation to even larger particles, I also model planar metallic and silica interfaces with the same surface charge density, which correspond to an infinitely large Janus colloid. As shown in Fig. 5.11, with increasing colloidal size the divalent ions become more concentrated at the surface. This is mainly due to stronger attraction exerted by the free surface charge and can be understood from a simple analysis. Consider a z-valent ion at a distance Δx from a uniformly charged Janus particle radius R_{d} (referring to the location of dielectric jump, solid circle in Fig. 5.1), and free surface charge density σ_{f}. The electrostatic force exerted by the the surface free charges then can be written as $(4\pi\sigma_{\mathrm{f}}zl_{\mathrm{B}}k_{\mathrm{B}}T/e)\left(\frac{R_{\mathrm{d}}}{R_{\mathrm{d}}+\Delta x}\right)^{2}$ and, for fixed Δx, increases with R_{d}. On the other hand, the force also decays with ion distance Δx, at a rate that decreases with increasing colloid size—reaching a constant value in the planar limit. As a result, more ions are concentrated close to the surface when the colloid size increases. Despite this variation of density profile with colloid size (represented by the trends in Fig. 5.11), the contrast between the metal and silica hemispheres persists. Indeed, if I consider the maximum density ratio between the two hemispheres, the four times larger Janus colloid still gives the same ratio 1.4 ratio as in Sec. 5.3.2.1. For the planar limit, the ratio reduces to 1.307, coinciding with the ratio 17/13 predicted in my previous energy analysis.

5.3.3.2. Ionic size effects. Until this point, I have employed a constant ion size. However, the hydrated ion radius typically increases with valence [149], which would affect both the excluded-volume interactions and the electrostatic binding in my simulations. To assess the magnitude of these affects, I revisit the system of Sec. 5.3.1.2, i.e., a neutral silica/metal Janus colloid immersed in 50 mM 2:1 electrolyte, except that the divalent
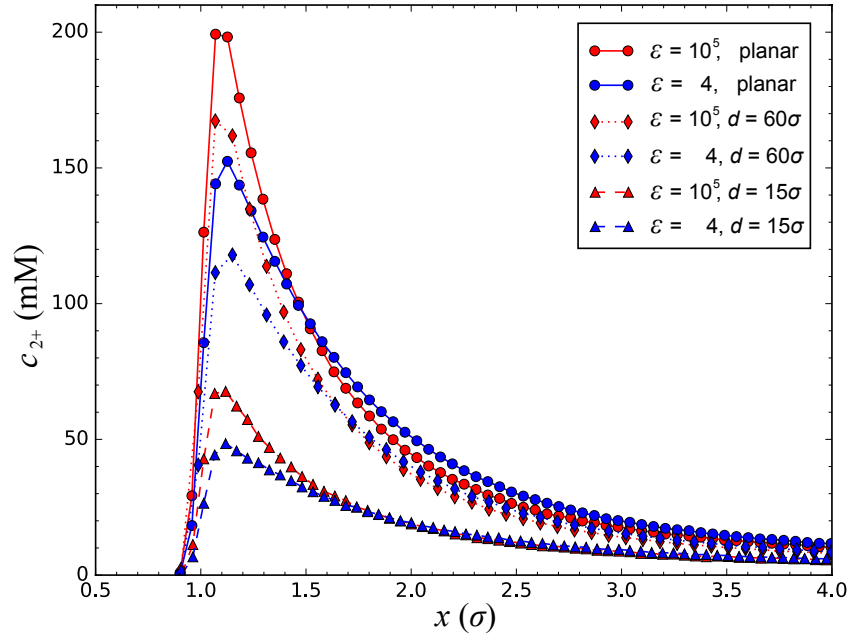
Figure 5.11. Effects of colloidal size on the density distribution of divalent counterions immersed in 20 mM 1:1 salt. The silica/metal Janus colloids are uniformly charged with surface free charge density $\sigma_f = -9.74 \times 10^{-2} e^-/\sigma^2$. The density profiles are shifted such that the horizontal axis represents the distance x of the ions to the dielectric interfaces. As the Janus colloid diameter increases from 15σ (triangles and dashed lines; data of Fig. 5.9) to 60σ (diamonds and dotted lines) and to infinity (circles and solid lines; planar interface), the counterions are more attracted to the surface, but the contrast in the counterion distribution between the metal and the silica hemispheres persists.

ions are 20% larger. As shown in Fig. 5.12, the concentration of divalent ions near the surface is systematically higher for the simulations with larger sizes (panel b). If I angularly average the density profile for each hemisphere (data not shown), I find that for both ion sizes the ion distributions approach the bulk density at very similar distances from the colloidal surface. Since the larger ions cannot approach the colloidal surface as closely as the smaller ones, the thickness of the electric double layer is effectively reduced, and the ion concentration is increased accordingly. In principle, this change in the distribution of the divalent ions could in turn affect the density profiles of the (unaltered) monovalent ions as well as the induced surface charge densities, but no statistically significant differences were observed.

5.3.4. Self-assembly of Janus particles

Not until recently, the role of the polarizations charges has been considered in the context of self-assembly of binary colloidal aggregates [14]. Depending on the dielectric mismatch between the isotropic particles and the solvent, the self-assembled structures can be qualitatively altered. However, as is demonstrated in the previous sections, heterogeneous colloids might have strong asymmetric ion distribution and display properties that are never observed for isotropic colloids. With synthesis techniques developed for more designable and controllable patchy particles, detailed manipulation of the electrostatic driven self-assembly becomes desirable. Based on the insights from this chapter, patchy colloids made of silica and metal will be considered. For a specific particle configuration, the dielectric mismatch can be tuned by changing the solvent. The dielectric interactions are attractive to free charges for both materials in non-polar solvents, while opposite in polar
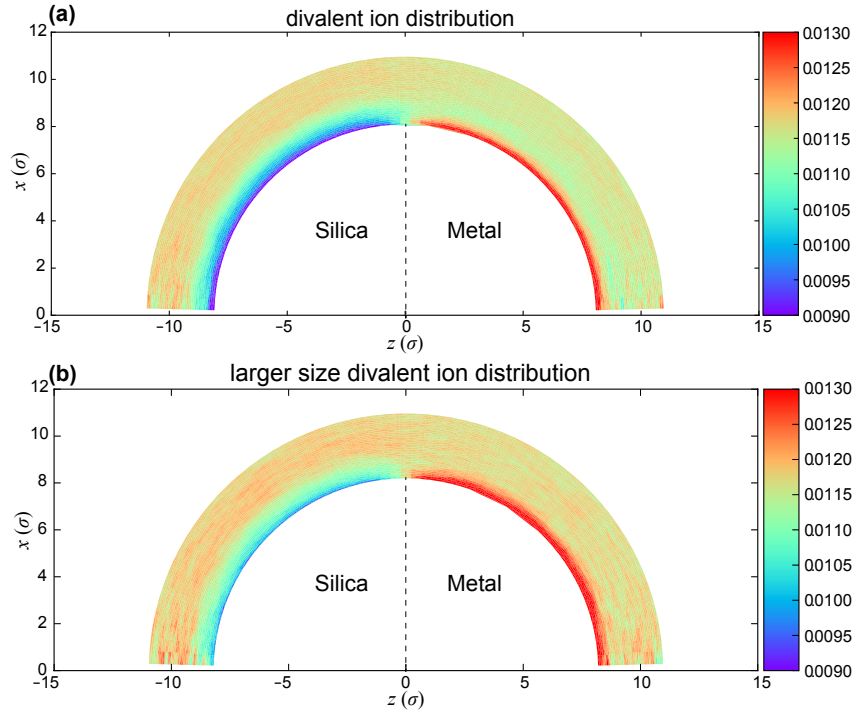
Figure 5.12. Divalent ion number density (σ^{-3}) distribution of 50 mM 2:1 electrolyte around a silica/metal Janus colloid. (a) Both monovalent and divalent ions have diameter σ; same data as in Fig. 5.6(a); (b) The same system, but with divalent ions of diameter 1.2σ.

solvents like water. This opens the possibility of generating solvent-dependent structures. Since induced charges are always weaker than source charges, to have the patchy colloids fully participate in the self-assembly process, similar to Ref. [14], I focus on binary mixture of charged spherical colloidal systems, which consist charged patchy colloids and counter-charged nanoparticles. In accordance with experiments, these particles are of size ~ 100 nm and surface charge density ~ 1 mC/m^2. The surface charges will be uniformly distributed on the colloidal surface or as a more realistic model, only reside on the silica surface.
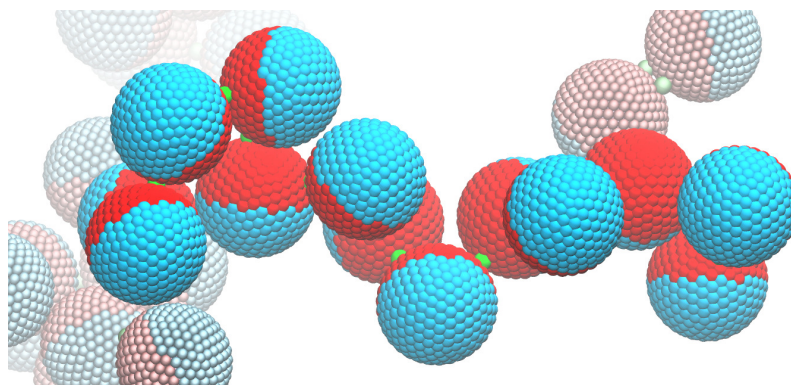
Figure 5.13. Self-assembly of divalent Janus nanoparticles with relative relative permittivity 1 (blue surface) and 100 (red surface) in a solvent of permittivity 2.

Here I present some preliminary work on the self-assembly of divalent uniformly charged Janus colloid with counter-charged nanoparticles (Fig. 5.13). The size asymmetry is 15:1. The Janus colloid has relative permittivities 1 (blue surface) and 100 (red surface) with solvent permittivity 2, i.e., dielectric effects are attractive for the red hemispheres, while repulsive for the blue. As a consequence, nanoparticles only attach to the red hemispheres. This structure is similar to the findings in Ref. 14, except the binding locations can be controlled by the surface coating, allowing possibilities for orientation control.

5.4. Conclusion

I have presented a systematic examination of dielectric effects on the ion distribution around a spherical Janus particle embedded in an aqueous electrolyte solution. I have employed molecular dynamics simulations supplemented with a boundary-element-based preconditioned dielectric solver that computes induced polarization charges at each

time step, at all dielectric interfaces [2, 143]. Via finite-element calculations I demonstrated that Janus particles created by metallic coatings can—as far as dielectric effects are concerned—be accurately represented as composed of two evenly divided hemispheres with a dielectric mismatch at the equatorial interface.

I have investigated two typical Janus particles that are representative in their dielectric configurations, namely silica/silicon and silica/metal. If such a colloid is neutral, ions are depleted from (or attracted to) the silica (or metal) hemispheres due to the dielectric contrast with the surrounding medium. Whereas a silica/silicon Janus colloid behaves effectively similar to a dielectrically isotropic particle, a silica/metal Janus colloid shows clear anisotropy in the surrounding ion distribution. In an asymmetric electrolyte, dielectric effects can even result in the generation of an effective electric dipole moment on the colloid.

For uniform highly charged silica/metal Janus colloids, the EDL contrast persists even at high salt concentration, especially for divalent counterions. As a more realistic model, I have also considered an *anisotropically* charged silica/metal Janus colloid. I found that dielectric effects still suppress the counterion concentration on the silica side, unless this hemisphere is highly ionized. These results demonstrate that dielectric effects cannot be ignored for the EDL structure of Janus particles.

Dielectric effects, even with the efficient solver of Ref. 2 and the preconditioning techniques of Ref. 143, are computationally costly. As a result, the Janus colloids are modeled here as significantly smaller than their typical experimental counterparts. However, as demonstrated in Sec. 5.3.3, the analysis presented remains applicable for larger particles. Although free charge interactions may vary, the dielectric effects are hardly affected.

Our findings not only clarify the effect of dielectric mismatch on the electrolyte distribution around synthetic Janus colloids, which is crucial for their colloidal interfacial properties, but also offer a potential avenue to control dielectric self-assembly [14] and may have implications for biological entities with dielectric anisotropy.

CHAPTER 6

Extension of the IDS for equipotential surfaces and bulk dielectrics

6.1. IDS for equipotential surfaces

6.1.1. Introduction

Conducting dielectric surfaces with constant electric potential widely appear in chemical and biological systems. For example, nanoelectrodes when applied with a voltage difference can mimic the transmembrane ion transport process [150]. They can also confine conducting nanoparticles through electrostatic trapping [151]. In real membranes, lipid bilayers can have pores generated by thermal fluctuations or electric fields. Due to the high permittivity of water and the voltage difference across the membrane, each ion channel acts as a conductor and a battery in parallel [152]. All these effects heavily involve polarization charges that are difficult to measure in experiments. Coarse-grained computer simulations can often provide insights into these systems.

Although finite-element methods (FEMs) or finite-difference methods (FDMs) can resolve polarization effects for interfaces with constant potentials, they are often limited to static systems, while in dynamical simulations, such effects need to be computed at each time step. Thus, accurate and efficient algorithms are desirable. Moreover, to investigate transport properties or collective motion behaviors, molecular dynamics (MD) simulations, in which forces instead of potential energy are used to evolve the systems, are

often more suitable than Monte Carlo (MC) simulations. The electrostatic forces are more accurately evaluated from pairwise charge interactions than via energy derivatives. Unlike the FEMs/FDMs that solve the 3D potential problem, the boundary-element method (BEM) computes the polarization charges on the dielectric interfaces directly, which is ideal for MD-based simulations. Since its introduction in the 1950s [153, 154], the BEM has mainly attracted attentions from applied mathematicians and mechanical engineers. Although still in its infancy for the soft matter community, several BEM-based dielectric algorithms have been proposed [31, 32, 26, 2]. Among them, the iterative dielectric solver (IDS), developed by Barros and Luijten [2], provides an optimized scheme for the BEM to be applied in MD simulations. The IDS can effectively solve dielectric systems with arbitrary geometries and surface free charges, but cannot impose constant potentials. One of the objective of this research is to extend the current IDS to solve for systems with constant potentials while maintaining its efficiency and accuracy.

6.1.2. Methods and results

For dielectric interfaces with constant potentials, we need to change the IDS boundary integral equation for the Poisson's equation from the previous Neumann boundary condition of Eq. (2.3) to the Dirichlet boundary condition, i.e., from the dielectric displacement discontinuity condition to the fixed surface potential constraint. Consider a dielectric surface $\mathbf{S}$ embedded in space $\mathbf{V}$. At an arbitrary surface location $\mathbf{s}$, we have the surface charge density $\sigma(\mathbf{s})$ including both free and induced charges. There is also a free charge distribution $\rho_{\mathrm{f}}(\mathbf{r})$ in the bulk. We impose a constant surface potential $u(\mathbf{s})$ at each surface

location. According to the Dirichlet boundary condition, we have

$$(6.1) \qquad \lim_{\delta \to 0} \iint_{\mathbf{S}, |\mathbf{s}-\mathbf{s}'|>\delta} \frac{\sigma(\mathbf{s}')}{4\pi\epsilon_0|\mathbf{s}-\mathbf{s}'|}d\mathbf{s}' + \iiint_{\mathbf{V}\backslash\mathbf{S}} \frac{\rho_{\mathrm{f}}(\mathbf{r}')}{4\pi\epsilon_0\epsilon(\mathbf{r}')|\mathbf{s}-\mathbf{r}'|}d\mathbf{r}' = u(\mathbf{s}) \;,$$

where to avoid the divergence of the layer potential, the infinitesimal disk $|\mathbf{s}-\mathbf{s}'| \leq \delta$ is excluded. $\epsilon(\mathbf{r}')$ is the relative permittivity in the bulk location $\mathbf{r}'$. If we discretize the dielectric surface into N patches, Eq. (6.1) can be transformed into a matrix equation $\mathcal{A}\sigma = \mathbf{b}$ with

$$(6.2) \qquad A_{ij} = \frac{\eta_i \sqrt{a_i}}{4\pi\epsilon_0} + \frac{q_j}{4\pi\epsilon_0|\mathbf{s}_i - \mathbf{s}_j|} \;,$$

$$(6.3) \qquad b_j = u_i(\mathbf{s}_i) - \frac{q_k}{4\pi\epsilon_0\epsilon(\mathbf{r}_k)|\mathbf{s}_i - \mathbf{r}_k|} \;,$$

where a_i is the area of patch i and η_i is the dimensionless geometric factor determined by its shape. It can be shown for the disk-shaped patches with mean curvature that are typically used in the IDS solver, $\eta = \sqrt{4\pi}$ (see Appendix 6.3). Similar to the IDS, the matrix equation can the solved iteratively via the GMRES. More importantly, A_{ij} requires on explicit construction of the matrix elements, since the time-consuming matrix–vector multiplication required at each iteration of the GMRES is essentially the potential at each patch that can be sped up by a fast Ewald solver. I implemented this algorithm in LAMMPS, a molecular dynamics simulations package, with tweaks for the fast Ewald solvers to obtain the potential per patch [155]. For a system with N surface patches and M bulk free charges, with Ewald summation, this algorithm scales as $\mathcal{O}(N+M)^{3/2}$. It has a better scaling for the particle–particle particle–mesh (PPPM) solver with $\mathcal{O}\left[(N+M)\log(N+M)\right]$

and for the multi-level summation method (MSM) solver with $\mathcal{O}(N + M)$. Here I demonstrate the effectiveness of this algorithm by considering a metal nanoparticle of size 14σ (20.16 nm) kept as a constant potential $u = 1V$ with a positive monovalent ion placed σ above its surface (see Fig. 6.1). The metal sphere is dicretized into 1472 patches. The extended IDS is used to resolve the polarization charges. Although the nanoparticle is positively charged in general to keep the positive $1V$ potential, the polarization charge density close to the ion is negative to balance the high potential generated by the source ion.

Furthermore, many important electrostatic phenomena involve both dielectric objects that have constant net charges and conducting objects that are kept at constant potentials. For example, in electrostatic trapping, nanoparticles are polarized by a nonuniform electric field between two nanoelectrodes. In fact, since the boundary conditions for the objects are invariant in dynamics, we can couple both Eq. (2.3) and Eq. (6.1) into the IDS. As a proof of principle, I apply the IDS with mixed boundary conditions to study the electrostatic trapping of a metal nanoparticle (10 nm in diameter) confined between two wedge-shaped electrodes kept at $+10V$ and $-10V$, respectively. The polarization charges for a snapshot of the system is shown in Fig. 6.2. Since the electric field strength increases with the curvature of the electrode, the field is strongest near the tips of the electrodes. Due to the dielectrophoresis (DEP) force, the nanoparticle is attracted towards high field and resides at one of the electrode due to spontaneous symmetry breaking. It is important to note that the polarization effects are calculated dynamically throughout the simulation. To the best of my knowledge, it is the first time that the electrostatic interactions in the
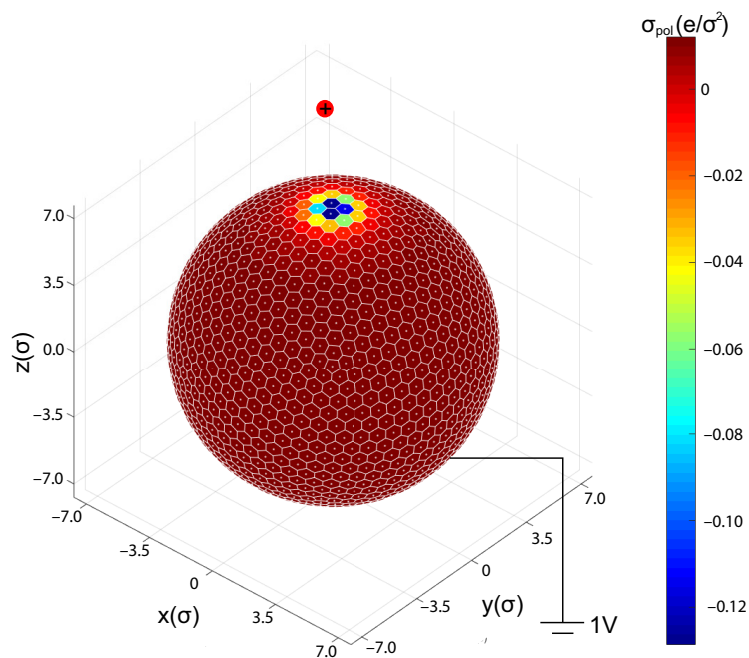
Figure 6.1. The surface charge density distribution of a metal surface kept at constant potential $1V$ with a positive monovalent ion at $z = 8\sigma$. The metal sphere has a diameter 14σ (20.16 nm) and is discretized into 1472 surface patches. For simplicity, we assume curved disk-like patches with uniform charge density. The metal sphere is generally positively charged to keep the surface at a positive potential, expect around locations close to the ion where the negative induced charges from the ion dominate.
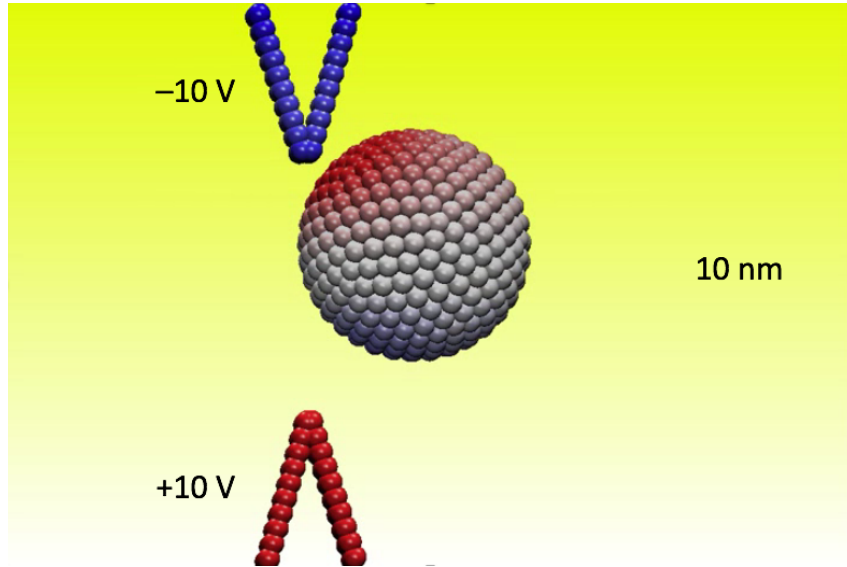
Figure 6.2. Simulation snapshot of the dielectrophoresis (DEP) of a 10 nm metal nanoparticle confined between two wedge-shaped electrodes kept at $+10V$ and $-10V$. Positive and negative surface charges are shown in red and blue colors, respectively.

DEP are fully resolved in a MD simulation. The extended IDS presents a new tool for design and study of collective motion of nanoparticles in the DEP self-assembly.

6.2. IDS for bulk dielectrics

6.2.1. Introduction

Although the sharp dielectric mismatch model is already a faithful representation of the real systems, it is still far from an accurate description. In most previous BEM studies, the ions are confined in their native dielectric media [24, 26, 32, 156]. However, penetrable dielectric boundaries are widely found in nature, such as the air–water interface of an open solution, the microfluidic channels and the nanopores of a membrane. As permittivity jumps at such interfaces, the ion–ion pair-interactions are different as well as their

dielectric self-energies [157]. To the best of my knowledge, there is only one BEM-based algorithm that allows ions to transport through a sharp dielectric boundary to a different dielectric region [158]. However, it is still limited to sharp interfaces, which only applies to systems with transition layer much thinner than the ion size. Moreover, smoothly varying dielectrics can occur in any inhomogeneous electrolyte solutions, as the permittivity of water is negatively correlated with the salt concentration [159], due to dielectric saturation [160]. Similar phenomena can also happen near charged colloids, electrodes, polyelectrolytes, or even concentrated bulk electrolytes. These problems are all beyond the scope of the IDS.

Until now, only limited research [161, 145] has been done in bulk dielectrics due to lack of efficient algorithms. Traditional grid-based FDM/FEM methods are prohibitively expensive if applied in particle-based simulations, let alone with mobile bulk dielectrics. As computational resources are growing rapidly over time, the study of mobile dielectrics with spatially varying permittivity is now within reach.

6.2.2. Methods and results

Similar to representing the surface induced charges as boundary elements in the IDS, the charge induced inside bulk dielectrics can be discretized into *volume-elements*. Thus, instead of assuming sharp dielectric boundaries, we solve the volume counterpart of Eq. (2.4), i.e., Eq. (1.12).

Upon grid discretization of the permittivity varying region, Eq. (1.12) can be easily transformed into a matrix equation. The similarity in the form between Eqs. (1.12) and Eq. (2.4) suggests that fast Ewald solvers can also be applied. Specifically, in the IDS, we

define each boundary element with the following quantities,

$$(6.4) \qquad\qquad \left[q_{\mathrm{f}}, \epsilon_{\mathrm{in}}, \epsilon_{\mathrm{out}}, s, \kappa, \hat{\mathbf{n}}_x, \hat{\mathbf{n}}_y, \hat{\mathbf{n}}_z\right] \ .$$

Here, q_{f} is the total free surface charge on a patch, which together with the patch area s gives the patch charge density σ_{f} in Eq. (1.12). The curvature κ is used for the self-contribution correction term for curved patches. Similarly, in the VEM implementation, we have the following parameters to define a volume element,

$$(6.5) \qquad\qquad \left[q_{\mathrm{f}}, \epsilon, v, (\nabla\epsilon)_x, (\nabla\epsilon)_y, (\nabla\epsilon)_z,\right] \ ,$$

where q_{f} divided by the volume v gives the free charge density ρ_{f} within a volume cell. For efficiency, the permittivity gradient $\nabla\epsilon$ can be precomputed if we only consider rigid dielectric objects. The self-polarization term within a volume cell requires special treatment and cannot be approximated by a single parameter, especially when source charges enter the volume cell.

This approach has mainly three advantages: (1) Discretization is required only in regions with inhomogeneous permittivity while source charges can be either inside or outside of dielectrics. (2) With proper force calculation, dynamic simulation of mobile rigid bulk dielectrics can be achieved, which is applicable for various biological systems. (3) With the independent $\nabla\epsilon$ calculation, the discretization scheme is not limited to cubic cells. In practice, there is a threefold challenge for this algorithm. First is to obtain accurate and convergent solution when source charges are outside of bulk dielectrics. Second is to allow source charges move freely inside bulk dielectrics, which needs to avoid the divergence of polarization charges when a source charge overlaps with gird points.

One also needs a good estimation for the self-contribution from the cell. Last, proper force calculation needs to be conducted to enable dynamics.

For this chapter, I try to tackle the first two stages of the challenge. I implemented the volume-element method (VEM) to consider only static configurations, i.e., no forces are concerned. Outside of the bulk dielectrics, charges can be at arbitrary locations. However, within bulk dielectrics, the grid is chosen such that source charges are away from the grid points (volume–element centers). To handle the divergence problem when a source charge approaches a grid point, I propose two ways. From the computation technique perspective, one can use an adaptive mesh, which requires careful treatment in the grid generation. From the physics perspective, another possible remedy is charge decomposition as adopted in the Maxwell equation molecular dynamics (MEMD) algorithm [162]. Similar to the particle mesh method in the PPPM, charges can be interpolated onto the grid, where the Poisson's equation gets solved. Then, the forces on the grid are used to back interpolate the forces on the original charges. Future studies can be carried out in both directions.

To verify the accuracy of the VEM, I consider the image potential of a unit charge moving through a gradual slab transition layer between silica ($\epsilon_{\mathrm{SiO_2}} = 2.1$) and silicon ($\epsilon_{\mathrm{Si}} = 11.7$). The simplest model for the transition layer is that the dielectric constant varies linearly

$$\epsilon(z) = \epsilon_{\mathrm{SiO_2}} + (\epsilon_{\mathrm{Si}} - \epsilon_{\mathrm{SiO_2}})\eta(z) \ , \tag{6.6}$$

where

$$
(6.7) \qquad \eta(z) = \begin{cases} 0, \ z < -z_t \\ z/z_t + 1, \ -z_t < z < 0 \\ 1, \ 0 < z \, . \end{cases}
$$

The image potential is defined as the electrostatic potential at the point charge due to its induced charges.

$$
(6.8) \qquad E_{\mathrm{imag}} = \frac{1}{2} \frac{Q}{4\pi\epsilon_0} \sum_i \frac{q_i}{r_i - r_0} \, ,
$$

where Q and r_0 are the source charge magnitude and location, q_i is the induced charge at site r_i. E_{img} can be solved analytically in a Fourier–Bessel form [163]. As a concrete comparison between the VEM and the analytical solution, we choose $z_t = 0.5$ nm and the point charge position ranges from -1.5 nm to 1.0 nm. In the VEM calculation, as an approximation to the infinite slab, the transition layer is 5×5 nm^2 periodic in the x and y directions and 100 nm in the z direction. Since the system has net charges, Ewald solver for non-neutral systems is used. When the source charge enters the transition layer, only the locations at volume cell vertices are calculated to minimize the discretization error.

As is shown in Fig. 6.3, the VEM results match very well with the analytical solutions. With finer grid in the z direction, better agreement is observed within the transition layer. It is important to note that at $z = -0.5$ nm and $z = 0.0$ nm, the analytical solution to the image potential is divergent. These two unphysical singularities are remediated with k-space dependent permittivity in the analytical solution.
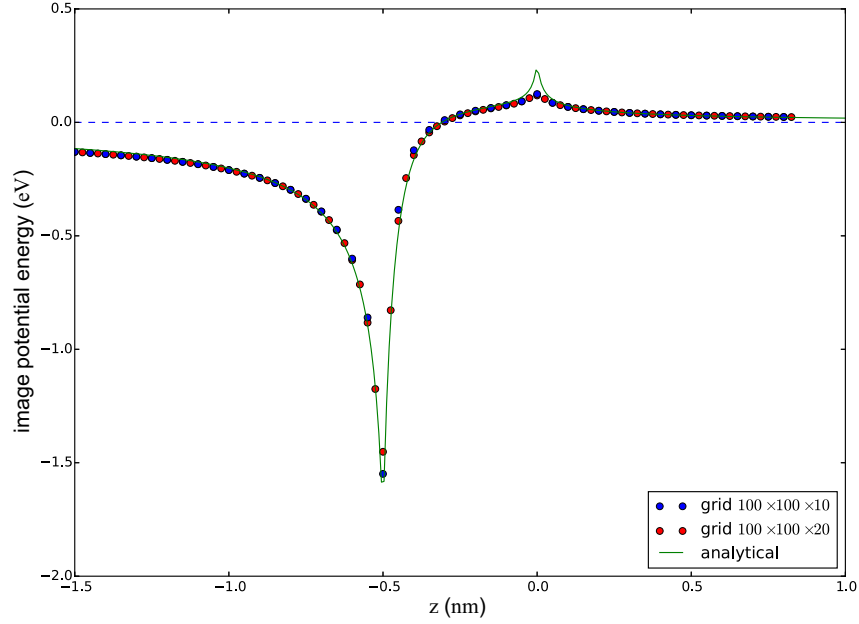
Figure 6.3. The image potential comparison between the VEM algorithm and the analytical solution of a point charge induced at a Si–SiO$_2$ transition layer with a linearly graded dielectric constant. The transition layer is discretized into 100×100 lattice points in the x–y planes and 10 (blue dots) or 20 (red dots) layers in the z direction.

6.3. Appendix: Self-potential for a disk-shaped patch

The original IDS assumes disk-shaped patches with a constant curvature as is shown in Fig. 6.4. Since one-point quadrature is used in the IDS, uniform surface charge density σ throughout the patch is assumed. Here I derive the self-potential of the patch at the center (purple dot).

The curved patch can be discretized along the θ_0 direction, giving a series of infinitesimal thin circular rings, each of area $2\pi R \sin \theta R d\theta$. The distance between the charges on each ring and the patch center is $2R \sin(\theta/2)$. Thus, the total self-potential at the center
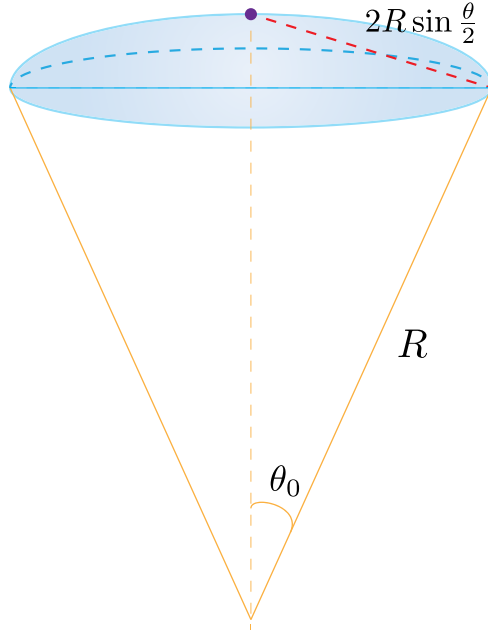
Figure 6.4. The sketch of a curved patch with constant curvature R^{-1} and uniform surface charge density σ. The self-potential of the patch is defined as the electric potential at the center of the patch (purple dot).

is

$$(6.9) \qquad \begin{aligned} \phi_{\mathrm{s}} &= \frac{1}{4\pi\epsilon_0} \int_0^{\theta_0} \frac{2\pi\sigma R \sin\theta R}{2R\sin(\theta/2)} d\theta \\ &= \frac{1}{\epsilon_0}\sigma R \sin\frac{\theta_0}{2} \ . \end{aligned}$$

Since in the IDS, each patch is characterized with the curvature R^{-1} and the area a. Note that $a = 2\pi R^2(1 - \cos\theta_0) = 4\pi R^2 \sin^2\frac{\theta}{2}$. Therefore,

$$(6.10) \qquad \phi_{\mathrm{s}} = \frac{\sigma\sqrt{4\pi a}}{4\pi\epsilon_0} \ .$$

Interestingly, the self-potential term is independent of the curvature.

CHAPTER 7

Surface tension of asymmetric electrolytes

This chapter represents a close comparison between Monte Carlo simulations and theoretical research. The theoretical calculation is performed by Mingnan Ding and Prof. Xiangjun Xing.

7.1. Introduction

Surfactants, substances that are adsorbed onto interfaces reducing their interfacial surface tensions, have broad applications in the detergent, oil recovery, and pharmaceutical industries [164]. On the contrary, when electrolytes are present, the surface tension of the liquid–vapor interface typically increases with their concentrations. Since the first measurement in 1910 [165], researchers have investigated such phenomenon actively for more than a century in both theory [78, 79, 166, 167, 168, 169, 170, 171, 172, 173] and experiment [174, 175]. However, it remains challenging due to the intangible effects of ion size and hydration, surface polarization, and ionic coupling. Moreover, when aqueous electrolytes are in contact with high permittivity media, such as metal, effects are anticipated to be qualitative different [168, 176], but results are scarce.

With the emergence of computer simulation techniques, coarse grained models help to incorporate many of the complicated effects, including the finite size effects, the ionic coupling, and the surface polarization. The most simple yet effective model for electrolytes is the restricted primitive model (RPM), which models the ions as hard spheres. Previous

Monte Carlo simulations predominately focused on symmetric electrolytes at water–air interface and achieved good agreements with experiments [15, 177]. The dielectric effects and steric effects were shown to be essential for the surface tension. For asymmetric electrolytes, the prediction for the excess surface tension is even harder since dielectrics effects are stronger for multivalent ions than monovalent ones. Such asymmetry in valences complicates the ion distributions. To the best of my knowledge, no simulation results are available for asymmetric electrolytes, despite their wide appearance in chemical and biological systems.

Theoretical approach to this problem dates back to 1924. Wagner [78] first attributed the excess surface tension to the depletion caused by the interactions between ions and their surface polarization charges, based on the Debye–Hückel (DH) theory of strong electrolyte [6]. Since then, giants like Onsager [79] were attracted to this fascinating topic. The famous Onsager–Samaras (OS) theory assumes constant Debye length throughout the system and derived a limiting law for symmetric electrolytes that agrees well with experiments at low concentrations. Under the OS framework, theories for asymmetric electrolyte were also developed [178, 167]. To resolve the theoretical puzzle at high concentrations, Levin and Flores-Mena [171] introduces an ion-free layer due to ion hydration in 2001 and achieved good accuracy even at high concentrations. This work was later generalized to general electrolyte solutions by Oshima [179]. However, the agreement between the theories based on Levin's framework and the experiments depends on the thickness of the ion-free layer as a fitting parameter, which is difficult to verify experimentally. Advantageous to experiments, systems are much cleaner and more tunable in simulations.

In light of this, to better test theoretical assumptions, my collaborators and I compare theories directly to our simulations.

In this chapter, I study the excess surface tension of electrolytes, especially asymmetric electrolytes with Monte Carlo simulations near two representative dielectric interfaces. For water–air interface, I compare my simulation results with the OS limiting law, the Levin's framework, and a newly developed theory based on charge renormalization. The charge renormalization theory corrects the bulk predictions of the linearized Poisson–Boltzmann theory and works particularly well for asymmetric electrolytes at high concentrations [91]. Although the excess surface tension originates from the excess ions near the interface, I find it remarkable that the charge renormalization in the bulk is actually essential for the properties at the interface. For water–metal interface, my simulations observe non-monotonic surface tension as a function of concentration. This indicates a competing mechanism between the dielectric adsorption and the steric effects.

7.2. Methods and Results

7.2.1. Simulation scheme

I consider aqueous electrolytes confined in a slab geometry of height H [see Fig. 7.1(a)]. The dielectric interface coincides with the Gibbs dividing surface at $z = 0$. The relative permittivity of water is $\epsilon_{\mathrm{w}} = 80$. The medium on the other side of the interface has permittivity $\epsilon_{\mathrm{a}} = 1$ or $\epsilon_{\mathrm{m}} = 10^5$, representing air and metal, respectively. The ions are modelled as non-additive hard spheres with point charges at their centers. There are two hard walls at $z = 0$ and $z = H$, i.e., the ion centers are confined in $d/2 < z < H$. Although ions are normally hydrated in water resulting in much lager radii than their crystal radii,
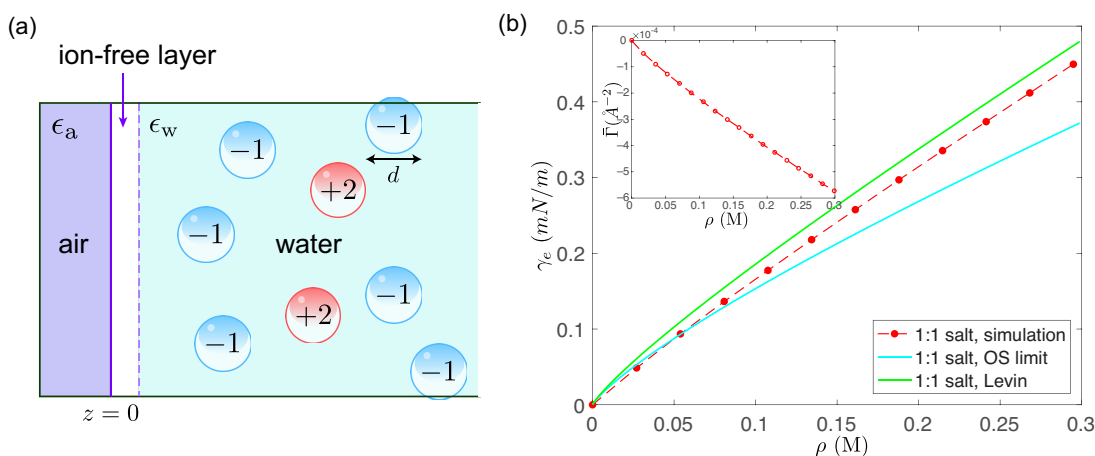
Figure 7.1. (a) Schematic plot of a 2:1 electrolyte near an interface between air and water. The aqueous electrolyte is confined in a slab geometry of height H (z direction). There is an ion-free layer with thickness $d/2$, where d is the ion size. Ions entering this layer would partially lose their hydration shell and therefore cost high energy. All ions are repelled from the interface by their image charges with multivalent ions (red circles) pushed further away because of their larger image charges. On average, the interface behaves as if negatively charged. Note that multivalent ions are surrounded by counter-ions in both sides. As a consequence, charge renormalization effects are important. (b) Surface tension of 1:1 electrolyte (dashed solid red) as a function of concentration with ion diameter $d = 4.6$Å. Two theoretical predictions are given, namely the OS limit theory (cyan) and Levin's theory (green). The inset shows the corresponding number of excess ion groups per unit area.

the hydration is much weaker near the interface [15]. For example, in $MgCl_2$, Cl^- is weakly hydrated at water–air interface with radii 2Å, compared to 3.32Å when fully hydrated with an adjustment ratio 0.6. Mg^{2+} has hydrated radius 4.28Å in the bulk [180]. For my model, I adopt the same adjustment ratio for the divalent ions that gives radii 2.6Å. To avoid extra steric effects arisen from ion size asymmetry that are difficult to treat in theories, I choose the average radius $d/2 = 2.3$Å for both ion species. It is important to note that my model and my collaborators' theory is not limited to $MgCl_2$, but applicable to other multivalent electrolytes. The system is at room temperature with Bjerrum length $l_B = 7.2$Å. I extend the slab Ewald summation with image charges incorporated to capture the polarization effects (see Appendix 7.4). The starting point of my model is the Gibbs adsorption isotherm.

$$(7.1) \qquad\qquad d\gamma_e = -\Gamma d\mu \ = -\Gamma_+ d\mu_+ - \Gamma_- d\mu_- \ ,$$

where $\mu_\pm$ are the chemical potentials of the positive and the negative ions. Since the ion distribution near the interface is different from the bulk, $\Gamma_\pm$ represent the number of excess ions per unit area for each ion species. As both $\mu_\pm$ and $\Gamma_\pm$ are concentration dependent, γ_e has to be integrated from zero concentration to the desired bulk concentration.

Thus, I first conduct canonical Monte Carlo simulations to obtain $\Gamma_\pm$ at various concentrations between 0 M and 0.273 M for a 2:1 electrolyte at both water–air and water–metal interfaces. It appears that the chemical potentials for each ion species are needed in order to apply Eq. (7.1). However, for arbitrary electrolyte of the form $A_m B_n$, based on particle number conservation, the excess cations and anions have to satisfy $\bar{\Gamma} = \frac{\Gamma_+}{m} = \frac{\Gamma_-}{n}$.

Together with Eq. (7.1), we have

$$(7.2) \qquad d\gamma_{\mathrm{e}} = -\frac{\Gamma_+}{m}(md\mu_+ + nd\mu_+) = -\bar{\Gamma}d\mu \ ,$$

where $\bar{\Gamma}$ is the number of excess ion groups $A_m B_n$ per unit area. This means no explicit chemical potential for each ion species is needed to calculate the excess surface tension. For the slab geometry,

$$(7.3) \qquad \Gamma_{\pm} = \int_0^{H/2} \rho_{\pm}(z)dz - \frac{H}{2}c_{\mathrm{b}} \ ,$$

where $\rho_{\pm}(z)$ are the density distributions for cations and anions, respectively. c_{b} is the actual bulk density. In each simulation, I ensure the electrolyte reaches bulk concentration at $H/2$ by choosing the box height $H > 10\lambda_{\mathrm{D}}$, where λ_{D} is the Debye length. c_{b} is obtained by taking the density average in the bulk region ($3.5\lambda_{\mathrm{D}} < z < H - 3.5\lambda_{\mathrm{D}}$).

Another set of grand canonical Monte Carlo simulations are followed to obtain the chemical potential as a function of concentration. I use a cubic simulation box of length $30d$ with periodic boundary conditions. The addition and removal of the ions are done in the unit of neutral ion groups to maintain the system charge neutral. For each given chemical potential, I obtain the corresponding electrolyte concentration at room temperature. I interpolate the data to get the corresponding chemical potentials in the previous canonical simulations. To avoid such chemical potential interpolation, a more elegant approach is to conduct GCMC simulations in a slab geometry, such that both the chemical potential and the excess ion number at a certain concentration can be obtained directly. Finally, numerical integration is performed to obtain the excess surface potential.

7.2.2. Surface tension at the electrolyte–air interface

The excess surface tension γ_e for the electrolyte–air interface has been extensively studied theoretically over the past century, especially for symmetric electrolytes. The agreements between previous theories and our simulations are shown in Fig. 7.1(b) for a typical 1:1 electrolyte. The prediction for the excess surface tension by the well-known OS theory (cyan curve) gives good accuracy at relative low concentrations ($\rho < 0.1$ M) compared to my simulation results (dashed solid red curve). However, its prediction is significantly smaller than the simulation data at high concentrations. The main reason for this error is that the OS theory ignores the depletion of ions near the interface, which gives smaller estimation for the number of excess surface ions. To remedy such steric effects, in the theory by Levin [171], an ion-free layer with thickness of the ion radii is introduced. They further realized that this depletion not only leads to a correction proportional to the ion radii, but also alters the image charge effects. In the OS theory, the image charge interaction has been assumed to have the form $e^{-\kappa z}$ in both the electrolyte and the depletion layer, where κ is the inverse of the Debye length. However, in the actual system, the image charge interaction decays much slower since there are no ions in the depletion layer. This leads to a stronger repulsion from the interface to the ions. Such theory (green curve) gives much better accuracy at high concentrations than the OS theory but is systematically biased towards higher values.

According to the Gibbs adsorption isotherm, the prediction for the surface tension strongly relies on the accuracy of the density profile, which is much more complicated for 2:1 electrolytes. As an example, the blue curves in Fig. 7.2(a) shows the density profile of 2:1 electrolyte at 0.17 M concentration for the water–air interface. Since the self-image
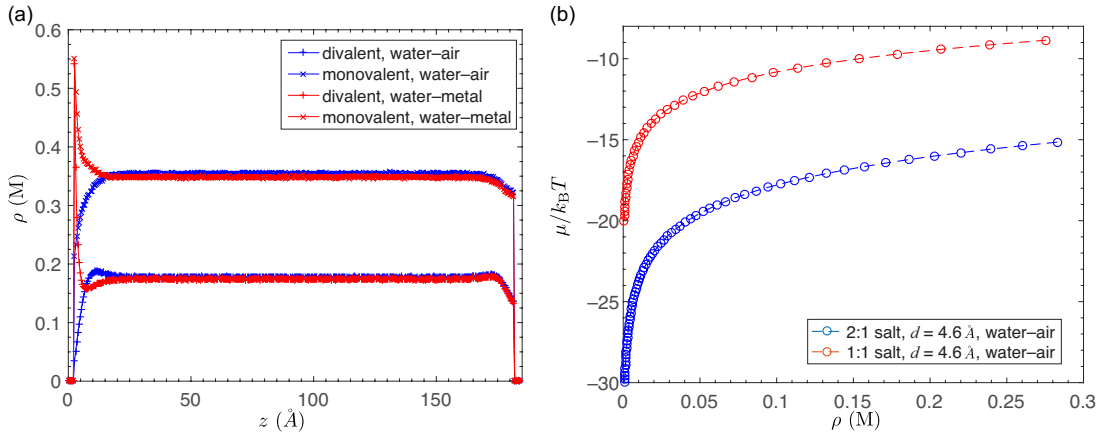
Figure 7.2. (a) The density profile of the 2:1 electrolyte at 0.17 M concentration with a dielectric interface (water–air or water–metal) at $z = 0$. The divalent ions are more depleted from or attracted to the interface than the monovalent ions. The depletion at the other hard wall ($z = 184$Å) is due to steric effects and electrostatic interactions (see main text). The bulk region in the middle is used to calculate the bulk concentration. (b) Chemical potential of the 2:1 electrolyte (dashed blue) and the 1:1 electrolyte (dashed red) as a function of concentration with ion diameters $d = 4.6$Å.

potential energy scales quadratically with the ion valence, near the interface, divalent ions are more depleted resulting a net negative charge layer. Such layer is compensated by a positive charge layer further away from the surface, as enforced by the charge neutrality condition of the system. The depletion region near the hard wall at $z = 184$Å manifests the lack of symmetric shell of screening counterions [69].

Contrary to the complicated density profile, the excess surface tension curve is very similar to the 1:1 electrolyte (see Fig. 7.3 red curve), except increases at a much faster rate with concentration. At high concentrations $\rho > 0.2$ M (inset of Fig. 7.3), the slope ratio between the 2:1 and 1:1 electrolytes is about 1.6. Two components attribute to the higher surface tension for the asymmetric electrolyte. First of all, its ions are more depleted from the interface than the 1:1 electrolyte. But since dielectric effects are relatively
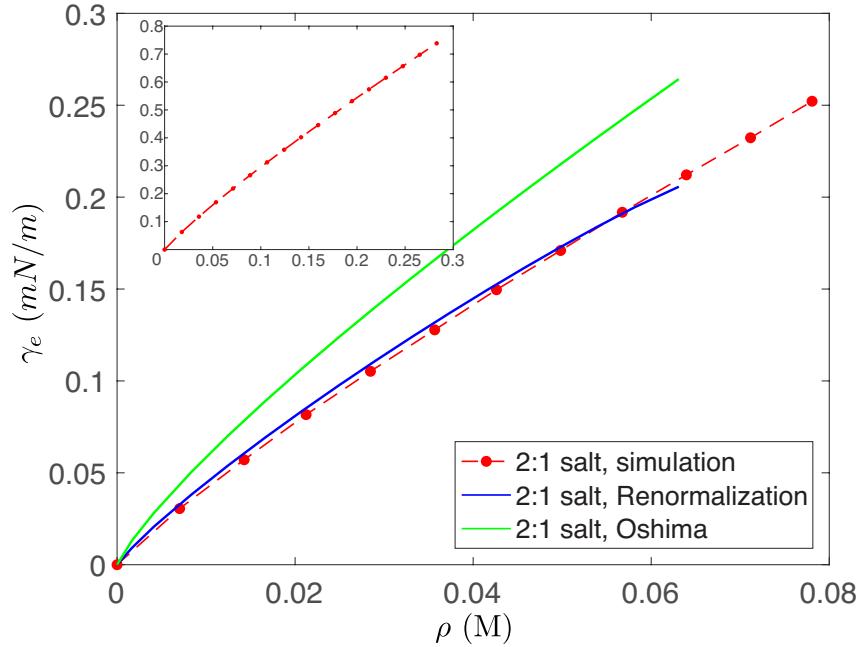
Figure 7.3. The inset shows the excess surface tension of the 2:1 electrolyte at water–air interface obtained in my simulations (dashed red). The main figure gives the predictions by Oshima based on Levin's framework (green) and my collaborators' charge renormalization theory (blue) at low relatively concentrations.

short-ranged, the majority of the difference originates from their chemical potentials [see Fig. 7.2(b)], as the chemical potential of a neutral group in the 2:1 salt is about 1.5 times larger than a neutral pair of the 1:1 salt. As a net effect, the surface tension increment $d\gamma_e/d\rho$ for the 2:1 salt is roughly 1.6 times larger.

To predict the excess surface tension from a theoretical perspective is even more challenging. Levin's theory has been generalized to asymmetric salts by Ohshima [179]. However, it doesn't give satisfactory agreement with our simulation even at low concentrations (green curve in Fig. 7.3). This is because the linearized PB theory fails to describe the bulk properties in such case. Charge renormalization manifests itself even in low densities. As we shall see, the renormalized charge of the divalent ions are much larger than the

bare charge so that repulsion of ions from their image charges becomes much larger. On the other hand, the renormalized charge gives smaller Deybe length predicting less ions repelled from the surface.

The charge renormalization theory starts by representing $\Gamma_\pm$ via the mean potential $\phi(z)$ of the system as

$$(7.4) \qquad \Gamma_\pm = \int_{d/2}^{\infty} \rho_\pm e^{-\beta U(z, q_\pm, \phi(z))} dz \ ,$$

where $U(z, q_\pm, \phi)$ are the potentials of mean force for each ion species. $\rho_\pm$ and $q_\pm$ are the corresponding densities and charges of the ions. In the PB theory, $U(z, q_\pm, \phi)$ are set to be

$$(7.5) \qquad U(z, q_\pm, \phi) \approx q_\pm \phi(z) \ ,$$

which is a mean-field assumption. It ignores the correlation between ions that is especially important for asymmetric electrolytes.

To give a more accurate description, the charge renormalization theory modifies this assumption to be

$$(7.6) \qquad U(z, q_\pm, \phi) \approx q_\pm^{\mathrm{R}} \phi(z) + \delta U(z, q_\pm) \ .$$

Here, $q_\pm^{\mathrm{R}}$ are the renormalized charges of the ions that are illustrated and calculated in Ref. 91. Such charge renormalization effects can be quite significant. For 0.5M 2:1 asymmetric electrolyte modelled in my simulations, the valence of the divalent ion after renormalization is about +5. This huge difference between the bare charge and the

renormalized charge is the reason why renormalization is important for asymmetric electrolytes. The second correction term of Eq. (7.6), $\delta U(z, q_\pm)$, contains the influence of the interface. It counts the interaction between an ion and its image charge in the OS theory. Levin and Flores-Mena pointed out that the depletion layer due to the finite size of the ions modifies this interaction [171]. As is shown in Fig. 7.1(b), they gave a much more accurate prediction for symmetric electrolytes. For asymmetric electrolytes, the correlation between ions should be included. In the charge renormalization theory, this means that we should replace the ion charges with the renormalized ones. Furthermore, charge renormalization also changes the decay length of the mean potential in an unusual way, giving a renormalized Debye length κ_R. κ_R is related to the renormalized charge through

$$(7.7) \qquad \left(\frac{\kappa_R}{\kappa_0}\right)^2 = \frac{q_+^R - q_-^R}{q_+ - q_-} \ .$$

Combining all these together, we obtain

$$(7.8) \qquad \delta U(z, q_\pm) \simeq \frac{\delta U(d/2, q_\pm)d}{2z} e^{-2\kappa_R z} \ ,$$

where $\delta U(d/2, q_\pm)$ as well as other details are given in the *Supplementary Note 1* of Ref. [181]. Since the renormalized charges are always larger than the bare charges, κ_R is larger than κ_0. This means the renormalized theory predicts a faster decay away from the interface than the previous mean-field theories. Although this effect predicts fewer ions that are repelled from the interface, the repulsion of ions due to image charges is greatly enhanced by the charge renormalization. To determine the net effect, we need to solve

the mean potential $\phi(z)$. We write down the Poisson equation of the system for $z > d/2$,

(7.9)
$$- \epsilon_0\epsilon_{\rm w}\frac{d^2\phi(z)}{dz^2} = \rho_+q_+e^{-\beta U(z,q_+,\phi)} + \rho_-q_-e^{-\beta U(z,q_-,\phi)} ,$$

with $\phi''(z) = 0$ in the ion-free layer $(0 < z < d/2)$. Combine Eq. (7.9) with Eq. (7.6) and Eq. (7.8), after linearization, we obtain a closed equation for $\phi(z)$,

(7.10)
$$- \epsilon_{\rm R}\phi''(z) + \epsilon_{\rm R}\kappa_{\rm R}^2\phi(z) = S(z) .$$

$\epsilon_{\rm R}$ is the renormalized dielectric constant that is close to $\epsilon_{\rm w}$ when the density is not high enough for charge oscillation to take place. $S(z)$ is defined as

(7.11)
$$S(z) \equiv \rho_+q_+e^{-\beta\delta U(z,q_+)} + \rho_-q_-e^{-\beta\delta U(z,q_-)} .$$

For the electrolyte–air interface, the boundary condition for this equation at $z = 0$ is $\phi'(0) = 0$. Consequently, the solution for Eq. (7.10) is

$$
\begin{aligned}
\phi(z) &= \frac{1}{2\kappa_{\rm R}\epsilon_{\rm R}}\Big(e^{-\kappa_{\rm R}z}\int_{d/2}^{\infty}(e^{\kappa_{\rm R}z'} + e^{\kappa_{\rm R}(d-z')})S(z')dz' \\
&\quad -e^{-\kappa_{\rm R}z}\int_{z}^{\infty}(e^{\kappa_{\rm R}z'} + e^{\kappa_{\rm R}(d-z')})S(z')dz' \\
&\quad + \big(e^{\kappa_{\rm R}z} + e^{\kappa_{\rm R}(d-z)}\big)\int_{z}^{\infty}e^{-\kappa_{\rm R}z'}S(z')dz'\Big) .
\end{aligned}
$$
(7.12)

Substitute Eq. (7.12) into Eq. (7.4), we get

(7.13)
$$\Gamma_\pm = \rho_\pm\int_{d/2}^{\infty}\left[1 - e^{-\beta\delta U(z,q_\pm)-\beta q_\pm^R\phi(z)}\right]dz + \frac{1}{2}\rho_\pm d .$$

The terms $\rho_\pm d/2$ is due to the depletion layer at $0 < z < d/2$.

To obtain the surface tension, we need to further calculate the chemical potential $\mu_\pm$, or in essence, $d\mu_\pm$. For symmetric electrolytes, the chemical potential μ_{OS} in the OS theory has the form

$$(7.14) \qquad \mu_{\mathrm{OS}} = k_{\mathrm{B}}T \log n + const. - \frac{q^2\kappa}{8\pi\epsilon_0\epsilon_{\mathrm{w}}(1+\kappa d)} \ .$$

In the renormalized theory, the chemical potential μ is modified to

$$(7.15) \qquad \mu = \mu_0 + \mu_{\mathrm{ex}} = k_{\mathrm{B}}T \log n + const. - \frac{q^2\kappa_{\mathrm{R}}}{8\pi\epsilon_0\epsilon_{\mathrm{w}}(1+\kappa_{\mathrm{R}}d)} \ ,$$

where ϵ_{w} is not renormalized. As long as the density is not high enough to have charge oscillation, $d\mu_{\mathrm{ex}}$ is much smaller than $d\mu_0$ as a function of the density. We can safely use $d\mu_0$ instead of $d\mu$ in theoretical calculations. This is also true for asymmetric electrolyte. With charge renormalization introduced, my collaborates' theory matches the simulation results very well at relative low concentrations (see Fig. 7.3 blue curve).

7.2.3. Surface tension at electrolyte–metal interface

So far I have studied the excess surface tension of the electrolyte–air interface. For the electrolyte–metal interface [see Fig. 7.4(a)], we have a different boundary condition at $z = 0$. The image charges of the ions are of the opposite sign, attracting the ions to the interface. According to Eq. (7.1), this leads to negative surface tension. On the other hand, the depletion among the ions and the interface persists. In light of Eq. (7.13), we can write the excess surface ion number as

$$(7.16) \qquad \Gamma_\pm = \rho_\pm \left(\int_{d/2}^{\infty} \left[1 - e^{-\beta\delta U(z,q_\pm)}\right] dz + \frac{1}{2}d \right) \ .$$
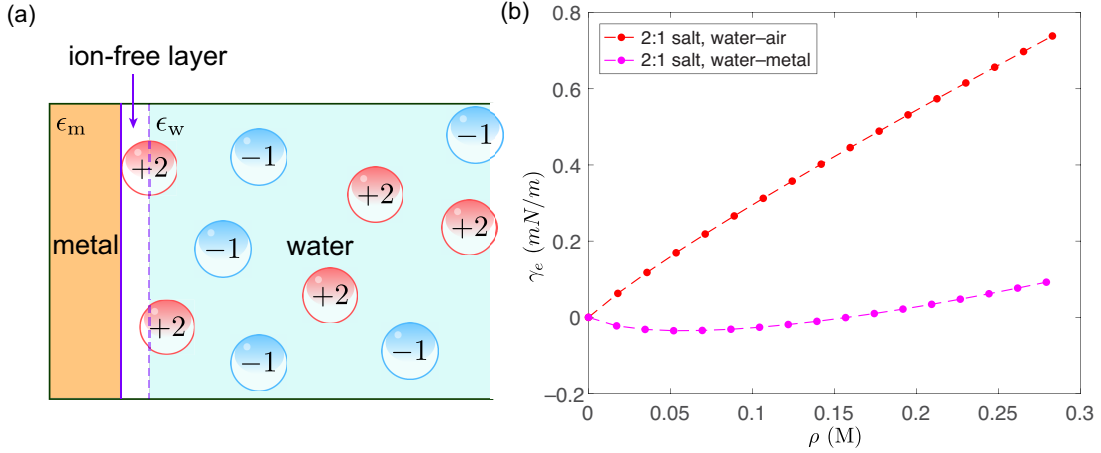
Figure 7.4. (a) Same system as Fig. 7.1(a) except the substrate is replaced by metal. All ions are attracted towards the interface by their image charges. The interface hence behaves as if positively charged. Furthermore, the absorbed multivalent ions are not surrounded by counter-ions on the left, hence the charge renormalization effects are much weaker. (b) The corresponding excess surface tension of the 2:1 electrolyte as a function of concentration (dashed purple). The surface tension shows non-monotonic behavior for the electrolyte–metal case and reaches a minimum at $\rho \approx 0.07$ M. The electrolyte–air case (dashed red) is included for comparison.

The only difference between Eq. (7.16) and Eq. (7.13) is that the mean potential $\phi(z)$ is ignored. This is because the ion densities converge to their bulk values so quickly (roughly within half of the Debye length) that the correlation energy $\delta U(z, q_\pm)$ dominates the exponential in Eq (7.16). Since $\delta U(z, q_\pm)$ is negative, the first term in Eq. (7.16) is also negative, showing the competition with the ion-free layer.

To a rough estimation, based on Eq. (7.8) and the fact that $U(d/2, q_\pm)d$ depends weakly on the density, the magnitude of δU decreases with the density. Thus, the net effect is that $\int_{d/2}^{\infty} e^{-\beta \delta U}$ decreases. As density grows, the decay of the density profile becomes so fast that fewer ions are attracted to the interface. Thus the $\frac{1}{2}\rho_\pm d$ term dominates. Since surface tension is the integration of $\Gamma_\pm$, the change of sign of $\Gamma_\pm$ leads

to the non-monotomicity of surface tension. As is shown in Fig. 7.4(b), the excess surface tension is non-monotonic with a minimum at $\rho \approx 0.07$ M. Such effect is not limited to asymmetric electrolytes. I observe the same phenomenon for symmetric electrolytes when I increase the ionic coupling.

7.3. Conclusion

In summary, I study the excess surface tension of asymmetric electrolytes at both water–air and water–metal interfaces. In agreement with previous studies, I find that dielectric effects are essential for the surface tension. I demonstrate that for symmetric electrolytes, Levin's theory with ion-free layer is a much more faithful representation of the system compared to the OS theory. However, such framework breaks down even at low concentrations for asymmetric electrolytes. With charge renormalization taken into account, our collaborators' theoretical prediction for the excess surface tension agrees very well with the simulation results at low concentrations. Furthermore, I find that for electrolyte–metal interface, adding ions to water could decrease the surface tension at low concentrations. The results presented in this paper provide a first through comparison between theory and simulation. I demonstrate that the charge renormalization framework is essential not only for understanding asymmetric electrolytes in the bulk, but also at the interface. The findings in this chapter help to understand the effects of ionic coupling on the surface tension, which has been ignored in previous theories.

7.4. Appendix: Ewald summation with image charges

Although the solution to the image charge of a planar geometry is well known [182, 66], it is not obvious to incorporate it into the Ewald summation, as the system involves
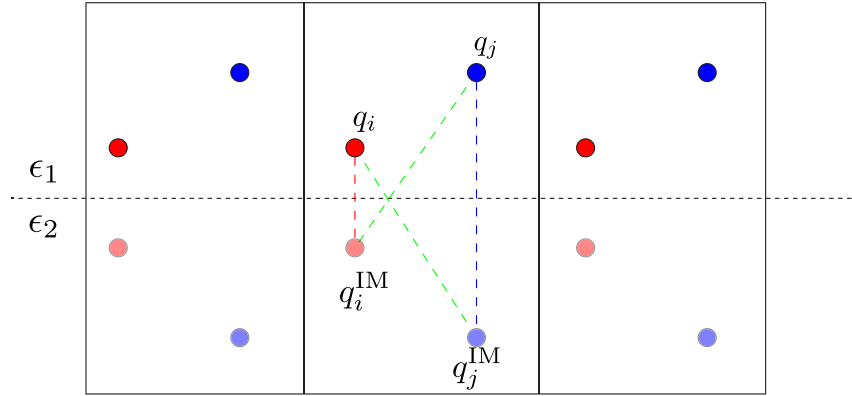
Figure 7.5. A system of N source charges confined in a slab geometry of permittivity ϵ_1. The corresponding image charges reside in the lower half space of permittivity ϵ_2.

multiple charges and periodic images. Here I demonstrate a technique that can obtain the system electrostatic energy without modifying the Ewald method.

Consider a system of N source charges embedded in a medium of relative permittivity ϵ_1 (see Fig. 7.5). The simulation box has a dimension of $L_x \times L_y \times L_z$ and is periodic in the xy plane. The medium below has a different permittivity ϵ_2. The polarization effects of a single charge q_i at $\mathbf{r}_i = (x_i, y_i, z_i)$ is equivalent to placing an image charge q_i^{IM} at $\mathbf{r}_i^{\mathrm{IM}} = (x_i, y_i, -z_i)$. By solving the Poisson's equation with boundary conditions at the interface, the magnitude of the image charge is

$$
(7.17) \qquad\qquad q_i^{\mathrm{IM}} = \frac{\epsilon_1 - \epsilon_2}{\epsilon_1 + \epsilon_2} \frac{q_i}{\epsilon_1} \; .
$$

The total energy of the system comprises two parts: the source–source charge interactions and the source–image charge interactions. The source–source charge potential

energy is simply given by the slab Ewald summation

(7.18)
$$U_{SS} = \frac{1}{2}\sum_{\mathbf{n}}{}' \sum_{i=1}^{N} \sum_{j=1}^{N} \frac{q_i q_j}{4\pi\epsilon_0\epsilon_1 |\mathbf{r}_{ij} + \mathbf{n}|} \ ,$$

where $\mathbf{n} = (n_x L_x, n_y L_y, 0)$ with n_x, n_y integers. The primed sum ignores the $i = j$ term when $\mathbf{n} = 0$. The slab Ewald summation can be done by adding a correction to the standard Ewald method [183]. As Ref. [182] pointed out, the potential energy between the source and the image charges needs to be reduced by a factor of 2. I show the same argument applies to the periodic system. I demonstrate this by adding charges one by one from infinity and calculate the corresponding potential energy. I start from a single charge q_i. It interacts with its image charge q_i^{IM} as well as the periodic images of q_i^{IM}. At any z distance from the surface, the force on q_i is

(7.19)
$$f_{ii'} = \sum_{\mathbf{n}} \frac{1}{4\pi\epsilon_0} \frac{q_i q_i^{IM}}{|2\mathbf{z} + \mathbf{n}|^2} \ ,$$

where $\mathbf{z} = (0, 0, z)$. By integrating the force from infinity to z_i, we have

(7.20)
$$\begin{aligned} u_{ii'} &= -\int_{\infty}^{z_i} f_{ii'} dz \\ &= -\int_{\infty}^{z_i} \sum_{\mathbf{n}} \frac{1}{4\pi\epsilon_0} \frac{q_i q_i^{IM}}{|2\mathbf{z} + \mathbf{n}|^2} dz \\ &= \frac{1}{2} \sum_{\mathbf{n}} \frac{1}{4\pi\epsilon_0} \frac{q_i q_i^{IM}}{|2\mathbf{z}_i + \mathbf{n}|} \ . \end{aligned}$$

When a second source charge q_j is added into the system, it interacts with both q_i^{IM} and q_j^{IM} as well as their periodic images.

(7.21)
$$
\begin{aligned}
u_{ji'} &= -\int_\infty^{z_j} \sum_{\mathbf{n}} \frac{1}{4\pi\epsilon_0} \frac{q_j q_i^{\mathrm{IM}}}{|\mathbf{x}_j + \mathbf{y}_j + \mathbf{z} - \mathbf{r}_i^{\mathrm{IM}} + \mathbf{n}|^2} dz \\
&= \sum_{\mathbf{n}} \frac{1}{4\pi\epsilon_0} \frac{q_j q_i^{\mathrm{IM}}}{|\mathbf{r}_j - \mathbf{r}_i^{\mathrm{IM}} + \mathbf{n}|}
\end{aligned}
$$

with $\mathbf{x}_j = (x_j, 0, 0)$ and $\mathbf{y}_i = (0, y_j, 0)$, and

(7.22)
$$
u_{jj'} = \frac{1}{2} \sum_{\mathbf{n}} \frac{1}{4\pi\epsilon_0} \frac{q_j q_j^{\mathrm{IM}}}{|2\mathbf{z}_j + \mathbf{n}|} \ .
$$

It is important to note that $u_{ji'}$ is not reduced, since q_i^{IM} is at a fixed location. Similarly, this process can be generalized to N source charges. The total image potential energy is

(7.23)
$$
\begin{aligned}
U_{\mathrm{SI}} &= \sum_{i=1}^{N} \sum_{j=1}^{i} u_{ij'} \\
&= \sum_{i=2}^{N} \sum_{j=1}^{i-1} \sum_{\mathbf{n}} \frac{1}{4\pi\epsilon_0} \frac{q_i q_j^{\mathrm{IM}}}{|\mathbf{r}_i - \mathbf{r}_j^{\mathrm{IM}} + \mathbf{n}|} + \frac{1}{2} \sum_{i=1}^{N} \sum_{\mathbf{n}} \frac{1}{4\pi\epsilon_0} \frac{q_i q_i^{\mathrm{IM}}}{|2\mathbf{z}_i + \mathbf{n}|} \\
&= \frac{1}{2} \sum_{\mathbf{n}} \sum_{i=1}^{N} \sum_{j=1}^{N} \frac{q_i q_j^{\mathrm{IM}}}{4\pi\epsilon_0 |\mathbf{r}_i - \mathbf{r}_j^{\mathrm{IM}} + \mathbf{n}|} \ .
\end{aligned}
$$

Eq. (7.23) shows that the image potential energy calculated by a dynamic charge addition process is equivalent to a static configuration by counting all the source–image interaction and reduce them by a factor of 2. This can be understood intuitively with the observation that $u_{ij'} \equiv u_{ji'}$ (two green dashed lines in Fig. 7.5). In the dynamic charge addition process, $u_{ii'}$ (red dashed line) and $u_{jj'}$ (blue dashed line) have 1/2 prefactor, while $u_{ji'}$ does not.

Since the Ewald summation involves all pairwise interactions between charges, to incorporate image charges into the Ewald summation, we can use a trick by reducing the image charge magnitude by $1/2$, i.e., $q_r^{\text{IM}} = q^{\text{IM}}/2$. We first calculate the total energy of N source charges and N reduced image charges. Denote the electrostatic energy between two groups of charges q_a and q_b to be $U[q_a, q_b]$. We have

$$U[q + q_r^{\text{IM}}] = U[q] + 2U[q, q_r^{\text{IM}}] + U[q_r^{\text{IM}}]$$

(7.24)
$$= U[q] + U[q, q^{\text{IM}}] + U[q_r^{\text{IM}}]$$

$$= U_{\text{SS}} + U_{\text{SI}} + + U[q_r^{\text{IM}}] \ .$$

Thus, the actual energy of the system is $U[q + q_r^{\text{IM}}] - U[q_r^{\text{IM}}]$.

CHAPTER 8

Conclusion

Polarization charges constantly appear in charged soft-matter systems and change their properties in unusual ways via many-body effects. To model such dielectric effects accurately and efficiently has been one of the key challenges for coarse-grained simulations as it involves solving the non-trivial Poisson's equation at every time step. Various algorithms have been proposed over the past decades. Among them, the boundary-element method (BEM) and the image-charge method (ICM) are the two major approaches to seek fast convergent solutions. This dissertation addresses various techniques regarding both methods with focus on the BEM approach. Here I present a summary of results and future outlook for each chapter.

I start with a direct comparison between the iterative dielectric solver (IDS) and the ICM in Chapter 2. Both methods are applied to study the polarization effects of multiple neutral dielectric spheres immersed in electrolytes. After analyzing their computational complexities and performances in particle-based simulations, I conclude that the IDS outperforms the ICM in complexity scaling when multiple objects are considered. The IDS is more suitable for molecular dynamics (MD) simulations since it does not require energy derivatives to calculate forces on dielectric objects. However, the ICM can be advantageous when charges are close to the dielectric interfaces since it does not involve surface discretization that can be expensive for the IDS. Two improvements can be made to both algorithms. For the ICM, dynamically changing the image-charge number based on the

charge–colloid distance can substantially reduce its computational cost. For the IDS, to overcome the singularity problem when source charges are in the vicinity of the interface, a non-uniform or even adaptive mesh can be explored. Furthermore, it is also possible to seek a hybrid method of the IDS and the ICM. In fact, recently via a combination of the ICM and the method of moments (MoM), a hybrid method has achieved $\mathcal{O}(N + M)$ linear complexity for systems with N ions and M dielectric spheres [184].

As a direct application of the IDS, I investigate the asymmetric electrolyte distribution near dielectric interfaces that display structures on the nanoscale in Chapter 3. Neutral surfaces are studied to isolate the dielectric effects from the intrinsic free charge interactions. In the presence of a repulsive dielectric interface, ion depletion is greatly enhanced by polarization charges. Furthermore, a net charge density accumulates near the interface that is mediated by the local curvature. Higher charge density is observed in the concave region than the convex region. The linearized Poisson–Boltzmann theory predicts linear charge density response to the surface undulation for small amplitudes. The findings suggest that charge patterns can be formed simply by tuning local surface structures.

The high accuracy of the IDS compared to other BEMs of the Poisson's equation is partially because its matrix equation is well-conditioned for extreme dielectric mismatches and complicated geometries. However, in Chapter 4, I show that the IDS suffers from low accuracy regardless of the discretization level for anisotropic particles with multiple dielectric mismatches. The eigenvalue spectrum of the matrix operator is no longer compact, suggesting a bad condition number. By introducing the Jacobi preconditioner together

with a physical constraint, the improved IDS is able to resolve the induced charges of anisotropic particles at high efficiency and accuracy.

The preconditioned IDS is applied to systematically study the electrolyte distribution near a Janus particle in Chapter 5. Two typical Janus particles are investigated, namely silica/silicon and silica/metal, as representative dielectric configurations. Anisotropic ion distribution is observed for the silica/metal Janus colloid while no significant distinction is found for the silica/silicon configuration. This shows that dielectric effects are not sensitive to small changes in the dielectric mismatch. For charged silica/metal Janus colloids, even with high concentration background salt, the electric double layer (EDL) contrast between the two hemispheres persist. This indicates that dielectric effects are essential for colloidal interfacial properties. Based on the results of a single Janus particle, I proceed to a preliminary study of the self-assembly of divalent uniformly charged Janus colloids with counter-charged nanoparticles. A chain structure is formed, similar to the previous result of the self-assembly of binary colloidal aggregates [14] except that the small nanoparticles only bind to the metallic hemispheres. The next step is to exploit this phenomenon by varying the metal coating area. This might serve as a pathway to control the Janus particle surface orientation and enable design of structures with chirality.

The boundary integral equation (BIE) formulated by the IDS is essentially based on the Neumann boundary condition that the electric displacement field satisfies the Gauss's law. The presumption of the IDS is that the net charge within a dielectric object is invariant. However, this condition is not valid for objects that are kept at constant potentials. In Chapter 6, I expand the IDS to resolve equipotential problems, and even systems with mixed boundary conditions, by imposing the Dirichlet boundary condition while keeping

its efficiency. This new tool enables us to simulate a broad range of systems, such as the electrostatic trapping of nanoparticles in dielectrophoresis, induced charge electro-osmosis (ICEO), and supercapacitors. Detailed analysis of the discretization error for this algorithm is needed. Moreover, since two BIEs are integrated into a single algorithm while they respond differently in accuracy for the same mesh, it would be insightful to explore preconditoning techniques for each matrix operator that can optimize the accuracy. Another presumption of the IDS is rooted in the sharp boundary assumption, which faces challenges for modeling many systems, such as the penetration of ions through a membrane and polyelectrolyte structure with spatially varying permittivity [145]. As a proof of principle, I demonstrate that via a volume-element approach, the extended IDS can readily resolve polarization charges within static bulk dielectrics. More challenging future work includes solving the divergence issue when source charges approaches the grid points, and performing appropriate force calculation to enable mobile bulk dielectrics.

I conclude the dissertation in Chapter 7 with a study of the excess surface tension of asymmetric electrolytes, which is strongly influenced by dielectric effects. Since only flat interfaces are concerned, the ICM is more efficient than the mesh-based IDS. I conduct MC simulations in collaboration with theoretical research. With the recently introduced concept of charge renormalization, my collaborator's theory matches my simulation results and outperforms previous theories. I find that for electrolyte–metal interface, the surface tension would decrease upon addition of salt at low concentrations. This effect is rarely discussed in previous studies.

References

[1] Jaydeep P. Bardhan, Robert S. Eisenberg, and Dirk Gillespie. Discretization of the induced-charge boundary integral equation. *Phys. Rev. E*, 80:011906, 2009.

[2] Kipton Barros, Daniel Sinkovits, and Erik Luijten. Efficient and accurate simulation of dynamic dielectric objects. *J. Chem. Phys.*, 140:064903, 2014.

[3] Yan Levin. Electrostatic correlations: from plasma to biology. *Rep. Prog. Phys.*, 65:1577–1632, 2002.

[4] Roger H. French, V. Adrian Parsegian, Rudolf Podgornik, Rick F. Rajter, Anand Jagota, Jian Luo, Dilip Asthagiri, Manoj K. Chaudhury, Yet-ming Chiang, Steve Granick, et al. Long range interactions in nanoscale science. *Rev. Mod. Phys.*, 82(2):1887–1944, 2010.

[5] David A. Walker, Bartlomiej Kowalczyk, Monica Olvera de La Cruz, and Bartosz A. Grzybowski. Electrostatics at the nanoscale. *Nanoscale*, 3(4):1316–1344, 2011.

[6] P. Debye and E. Hückel. Zur Theorie der Elektrolyte. I. Gefrierpunktserniedrigung und verwandte Erscheinungen. *Phys. Z.*, 24(9):185–206, 1923.

[7] Itamar Borukhov, David Andelman, and Henri Orland. Steric effects in electrolytes: A modified Poisson–Boltzmann equation. *Phys. Rev. Lett.*, 79(3):435–438, 1997.

[8] Jun Wang, Chunhu Tan, Yu-Hong Tan, Qiang Lu, and Ray Luo. Poisson–Boltzmann solvents in molecular dynamics simulations. *Commun. Comp. Phys.*, 3(5):1010–1031, 2008.

[9] Alexander R. J. Silalahi, Alexander H. Boschitsch, Robert C. Harris, and Marcia O. Fenley. Comparing the predictions of the nonlinear Poisson–Boltzmann equation and the ion size-modified Poisson–Boltzmann equation for a low-dielectric charged spherical cavity in an aqueous salt solution. *J. Chem. Theory Comput.*, 6(12):3631–3639, 2010.

[10] Erik Luijten, Michael E. Fisher, and Athanassios Z. Panagiotopoulos. Universality class of criticality in the restricted primitive model electrolyte. *Phys. Rev. Lett.*, 88:185701, 2002.

[11] Young C. Kim, Erik Luijten, and Michael E. Fisher. Screening in ionic systems: Simulations for the Lebowitz length. *Phys. Rev. Lett.*, 95:145701, 2005.

[12] René Messina. Image charges in spherical geometry: Application to colloidal systems. *J. Chem. Phys.*, 117(24):11062–11074, 2002.

[13] Elena Bichoutskaia, Adrian L. Boatwright, Armik Khachatourian, and Anthony J. Stace. Electrostatic analysis of the interactions between charged particles of dielectric materials. *J. Chem. Phys.*, 133(2):024105, 2010.

[14] Kipton Barros and Erik Luijten. Dielectric effects in the self-assembly of binary colloidal aggregates. *Phys. Rev. Lett.*, 113:017801, 2014.

[15] Alexandre Diehl, Alexandre P. dos Santos, and Yan Levin. Surface tension of an electrolyte–air interface: a Monte Carlo study. *J. Phys.: Condens. Matter*, 24(28):284115, 2012.

[16] Douglas J. Tobias, Abraham C. Stern, Marcel D. Baer, Yan Levin, and Christopher J. Mundy. Simulation and theory of ions at atmospherically relevant aqueous liquid–air interfaces. *Ann. Rev. Phys. Chem.*, 64:339–359, 2013.

[17] Arjan van der Vaart, Badry D. Bursulaya, Charles L. Brooks, III, and Kenneth M. Merz. Are many-body effects important in protein folding? *J. Phys. Chem. B*, 104(40):9554–9563, 2000.

[18] George D. J. Phillies. Excess chemical potential of dilute solutions of spherical polyelectrolytes. *J. Chem. Phys.*, 60(7):2721–2731, 1974.

[19] John D. Love. Dielectric sphere-sphere and sphere-plane problems in electrostatics. *Quart. J. Mech. Appl. Math.*, 28(4):449–471, 1975.

[20] Richard B. McClurg and Charles F. Zukoski. The electrostatic interaction of rigid, globular proteins with arbitrary charge distributions. *J. Colloid Interface Sci.*, 208(2):529–542, 1998.

[21] Per Linse. Electrostatics in the presence of spherical dielectric discontinuities. *J. Chem. Phys.*, 128(21):214505, 2008.

[22] Rosalind Allen and Jean-Pierre Hansen. Density functional approach to the effective interaction between charges within dielectric cavities. *J. Phys.: Condens. Matter*, 14(46):11981–11997, 2002.

[23] Itay Lotan and Teresa Head-Gordon. An analytical electrostatic model for salt screened interactions between multiple proteins. *J. Chem. Theory Comput.*, 2(3):541–555, 2006.

[24] Alexandre P. dos Santos, Amin Bakhshandeh, and Yan Levin. Effects of the dielectric discontinuity on the counterion distribution in a colloidal suspension. *J. Chem. Phys.*, 135(4):044124, 2011.

[25] Zecheng Gan and Zhenli Xu. Multiple-image treatment of induced charges in Monte Carlo simulations of electrolytes near a spherical dielectric interface. *Phys. Rev. E*,

84(1):016705, 2011.

[26] Vikram Jadhao, Francisco J. Solis, and Monica Olvera de la Cruz. Simulation of charged systems in heterogeneous dielectric media via a true energy functional. *Phys. Rev. Lett.*, 109(22):223905, 2012.

[27] L. D. Landau, E. M. Lifshitz, and L. P. Pitaevskii. *Electrodynamics of Continuous Media*, volume 8 of *Course of Theoretical Physics*. Elsevier Butterworth Heinemann, Oxford, 2nd edition, 1993.

[28] David G. Levitt. Electrostatic calculations for an ion channel. I. Energy and potential profiles and interactions between ions. *Biophys. J.*, 22(2):209–219, 1978.

[29] R. J. Zauhar and R. S. Morgan. A new method for computing the macromolecular electric potential. *J. Mol. Biol.*, 186(4):815–820, 1985.

[30] Hajime Hoshi, Minoru Sakurai, Yoshio Inoue, and Riichirô Chûjô. Medium effects on the molecular electronic structure. I. The formulation of a theory for the estimation of a molecular electronic structure surrounded by an anisotropic medium. *J. Chem. Phys.*, 87(2):1107–1115, 1987.

[31] R. Allen, J.-P. Hansen, and S. Melchionna. Electrostatic potential inside ionic solutions confined by dielectrics: a variational approach. *Phys. Chem. Chem. Phys.*, 3(19):4177–4186, 2001.

[32] Dezső Boda, Dirk Gillespie, Wolfgang Nonner, Douglas Henderson, and Bob Eisenberg. Computing induced charges in inhomogeneous dielectric media: Application in a Monte Carlo simulation of complex ionic systems. *Phys. Rev. E*, 69:046702, 2004.

[33] Per-Gunnar Martinsson. Fast evaluation of electro-static interactions in multi-phase dielectric media. *J. Comp. Phys.*, 211(1):289–299, 2006.

[34] Sandeep Tyagi, Mehmet Süzen, Marcello Sega, Marcia Barbosa, Sofia S. Kantorovich, and Christian Holm. An iterative, fast, linear-scaling method for computing induced charges on arbitrary dielectric boundaries. *J. Chem. Phys.*, 132:154112, 2010.

[35] Rio Yokota, Jaydeep P. Bardhan, Matthew G. Knepley, L. A. Barba, and Tsuyoshi Hamada. Biomolecular electrostatics using a fast multipole BEM on up to 512 GPUs and a billion unknowns. *Comput. Phys. Commun.*, 182(6):1272–1283, 2011.

[36] Zhenli Xu. Electrostatic interaction in the presence of dielectric interfaces and polarization-induced like-charge attraction. *Phys. Rev. E*, 87(1):013307, 2013.

[37] William Thomson. Extrait d'une Lettre de M. William Thomson à M. Liouville. *Journal de mathématiques pures et appliquées*, 10:364–367, 1845.

[38] C. Neumann. *Hydrodynamische Untersuchungen, nebst einem Anhange über die Probleme der Elektrostatik und der magnetischen Induction.* B.G. Teubner, Leipzig, 1883.

[39] Frank Olyslager and Ismo V Lindell. Closed form solutions of maxwell's equations in the computer age. *Radio Science Bull.*, 76(2):30–37, 2003.

[40] Zhenli Xu and Wei Cai. Fast analytical methods for macroscopic electrostatic models in biomolecular simulations. *SIAM Rev.*, 53(4):683–720, 2011.

[41] Zhenli Xu, Wei Cai, and Xiaolin Cheng. Image charge method for reaction fields in a hybrid ion-channel model. *Commun. Comp. Phys.*, 9(4):1056–1070, 2011.

[42] Youcef Saad and Martin H. Schultz. GMRES: A generalized minimal residual algorithm for solving nonsymmetric linear systems. *SIAM J. Sci. Stat. Comp.*, 7(3):856–869, 1986.

[43] Jie Liang and Shankar Subramaniam. Computation of molecular electrostatics with boundary element methods. *Biophys. J.*, 73(4):1830–1841, 1997.

[44] R. W. Hockney and J. W. Eastwood. *Computer Simulation Using Particles*. IOP Publishing, Bristol, 1988.

[45] E. L. Pollock and Jim Glosli. Comments on P³M, FMM, and the Ewald method for large periodic Coulombic systems. *Comput. Phys. Commun.*, 95(2–3):93–110, 1996.

[46] Josh Barnes and Piet Hut. A hierarchical $O(N \log N)$ force-calculation algorithm. *Nature*, 324:446–449, 1986.

[47] Andrew W. Appel. An efficient program for many-body simulation. *SIAM J. Sci. Stat. Comp.*, 6(1):85–103, 1985.

[48] Zhong-Hui Duan and Robert Krasny. An adaptive treecode for computing non-bonded potential energy in classical molecular systems. *J. Comput. Chem.*, 22(2):184–195, 2001.

[49] Zecheng Gan and Zhenli Xu. Efficient implementation of the Barnes–Hut octree algorithm for Monte Carlo simulations of charged systems. *Sci. China Math.*, 57(1):1331–1340, 2014.

[50] Jianzhong Wu, Dusan Bratko, and John M. Prausnitz. Interaction between like-charged colloidal spheres in electrolyte solutions. *Proc. Natl. Acad. Sci. U.S.A.*, 95:15169–15172, 1998.

[51] J. Z. Wu, D. Bratko, H. W. Blanch, and J. M. Prausnitz. Monte Carlo simulation for the potential of mean force between ionic colloids in solutions of asymmetric salts. *J. Chem. Phys.*, 111:7084–7094, 1999.

[52] Jiwen Liu and Erik Luijten. Stabilization of colloidal suspensions by means of highly charged nanoparticles. *Phys. Rev. Lett.*, 93:247802, 2004.

[53] Jiwen Liu and Erik Luijten. Colloidal stabilization via nanoparticle halo formation. *Phys. Rev. E*, 72(6):061401, 2005.

[54] C. J. Martinez, J. Liu, S. K. Rhodes, E. Luijten, E. R. Weeks, and J. A. Lewis. Interparticle interactions and direct imaging of colloidal phases assembled from microsphere–nanoparticle mixtures. *Langmuir*, 21(22):9978–9989, 2005.

[55] Stephen A. Barr and Erik Luijten. Effective interactions in mixtures of silica microspheres and polystyrene nanoparticles. *Langmuir*, 22:7152–7155, 2006.

[56] Guillermo Iván Guerrero-García, Enrique González-Tovar, and Mónica Olvera de la Cruz. Entropic effects in the electric double layer of model colloids with size-asymmetric monovalent ions. *J. Chem. Phys.*, 135(5):054701, 2011.

[57] Leslie Greengard and Vladimir Rokhlin. A fast algorithm for particle simulations. *J. Comp. Phys.*, 73(2):325–348, 1987.

[58] Leslie Greengard and Vladimir Rokhlin. A new version of the Fast Multipole Method for the Laplace equation in three dimensions. *Acta Numer.*, 6(1):229–269, 1997.

[59] H. Cheng, L. Greengard, and V. Rokhlin. A fast adaptive multipole algorithm in three dimensions. *J. Comp. Phys.*, 155:468–498, 1999.

[60] Lexing Ying, George Biros, and Denis Zorin. A kernel-independent adaptive fast multipole algorithm in two and three dimensions. *J. Comp. Phys.*, 196(2):591–626,

2004.

[61] M. Hoyles, S. Kuyucak, and S.-H. Chung. Solutions of Poisson's equation in channel-like geometries. *Comput. Phys. Commun.*, 115(1):45–68, 1998.

[62] Jean-Luc Guermond. Numerical quadratures for layer potentials over curved domains in $\mathbb{R}^3$. *SIAM J. Numer. Anal.*, 29(5):1347–1369, 1992.

[63] Jaydeep P. Bardhan, Michael D. Altman, David J. Willis, Shaun M. Lippow, Bruce Tidor, and Jacob K. White. Numerical integration techniques for curved-element discretizations of molecule-solvent interfaces. *J. Chem. Phys.*, 127:014701, 2007.

[64] Claudio Berti, Dirk Gillespie, Jaydeep P. Bardhan, Robert S. Eisenberg, and Claudio Fiegna. Comparison of three-dimensional Poisson solution methods for particle-based simulation and inhomogeneous dielectrics. *Phys. Rev. E*, 86:011912, 2012.

[65] John G. Kirkwood. Theory of solutions of molecules containing widely separated charges with special application to zwitterions. *J. Chem. Phys.*, 2(7):351–361, 1934.

[66] John David Jackson. *Classical Electrodynamics*. Wiley, New York, 3rd edition, 1999.

[67] Wei Cai, Shaozhong Deng, and Donald Jacobs. Extending the fast multipole method to charges inside or outside a dielectric sphere. *J. Comp. Phys.*, 223(2):846–864, 2007.

[68] Zhenli Xu. A fast algorithm for treating dielectric discontinuities in charged spherical colloids. *Interdiscip. Sci. Comput. Life Sci.*, 4(1):19–26, 2012.

[69] Zecheng Gan, Huanxin Wu, Kipton Barros, Zhenli Xu, and Erik Luijten. Comparison of efficient techniques for the simulation of dielectric objects in electrolytes. *J. Comp. Phys.*, 291:317–333, 2015.

[70] Henry A. Boateng and Robert Krasny. Comparison of treecodes for computing electrostatic potentials in charged particle systems with disjoint targets and sources. *J. Comput. Chem.*, 34(25):2159–2167, 2013.

[71] K. Binder and E. Luijten. Monte Carlo tests of renormalization-group predictions for critical phenomena in Ising models. *Phys. Rep.*, 344:179–253, 2001.

[72] Per Linse. Simulation of charged colloids in solution. *Adv. Polym. Sci.*, 185:111–162, 2005.

[73] Dirk Gillespie, Mónika Valiskó, and Dezso Boda. Density functional theory of the electrical double layer: the RFD functional. *J. Phys.: Condens. Matter*, 17(42):6609–6626, 2005.

[74] S. Asakura and F. Oosawa. On interaction between two bodies immersed in a solution of macromolecules. *J. Chem. Phys.*, 22:1255–1256, 1954.

[75] Sho Asakura and Fumio Oosawa. Interaction between particles suspended in solutions of macromolecules. *J. Polym. Sci.*, 33(126):183–192, 1958.

[76] Patrice Simon and Yury Gogotsi. Materials for electrochemical capacitors. *Nature Mater.*, 7(11):845–854, 2008.

[77] Osamu Shirai, Sorin Kihara, Yumi Yoshida, and Masakazu Matsui. Ion transfer through a liquid membrane or a bilayer lipid membrane in the presence of sufficient electrolytes. *J. Electroanal. Chem.*, 389(1-2):61–70, 1995.

[78] C Wagner. Die oberflächenspannung verdünnter elektrolytlösungen. *Phys. Z.*, 25:474–477, 1924.

[79] Lars Onsager and Nicholas N. T. Samaras. The surface tension of debyehückel electrolytes. *J. Chem. Phys.*, 2(8):528–536, 1934.

[80] Jean-Pierre Hansen and Hartmut Löwen. Effective interactions between electric double layers. *Ann. Rev. Phys. Chem.*, 51(1):209–242, 2000.

[81] David C Grahame and Roger Parsons. Components of charge and potential in the inner region of the electrical double layer: aqueous potassium chloride solutions in contact with mercury at 25°. *J. Am. Chem. Soc.*, 83(6):1291–1296, 1961.

[82] Marco Favaro, Beomgyun Jeong, Philip N Ross, Junko Yano, Zahid Hussain, Zhi Liu, and Ethan J Crumlin. Unravelling the electrochemical double layer by direct probing of the solid/liquid interface. *Nature Comm.*, 7, 2016.

[83] Luc Belloni. Ionic condensation and charge renormalization in colloidal suspensions. *Colloids and Surfaces A: Physicochemical and Engineering Aspects*, 140(1):227–243, 1998.

[84] A. Y. Grosberg, T. T. Nguyen, and B. I. Shklovskii. The physics of charge inversion in chemical and biological systems. *Rev. Mod. Phys.*, 74:329–345, 2002.

[85] Otto Stern. Zur theorie der elektrolytischen doppelschicht. *Berichte der Bunsengesellschaft für Physikalische Chemie*, 30(21-22):508–516, 1924.

[86] Kurt Andresen, R Das, Hye Yoon Park, H Smith, Lisa W Kwok, Jessica S Lamb, EJ Kirkland, D Herschlag, KD Finkelstein, and Lois Pollack. Spatial distribution of competing ions around dna in solution. *Phys. Rev. Lett.*, 93(24):248103, 2004.

[87] JEB Randles. Structure at the free surface of water and aqueous electrolyte solutions. *Physics and Chemistry of Liquids*, 7(1-2):107–179, 1977.

[88] Guangming Luo, Sarka Malkova, Jaesung Yoon, David G Schultz, Binhua Lin, Mati Meron, Ilan Benjamin, Petr Vanỳsek, and Mark L Schlossman. Ion distributions near a liquid-liquid interface. *Science*, 311(5758):216–218, 2006.

[89] Douglas Henderson. Recent progress in the theory of the electric double layer. *Progress in Surface Science*, 13(3):197–224, 1983.

[90] Marcelo Lozada-Cassou, Rafael Saavedra-Barrera, and Douglas Henderson. The application of the hypernetted chain approximation to the electrical double layer: Comparison with monte carlo results for symmetric salts. *J. Chem. Phys.*, 77(10):5150–5156, 1982.

[91] Mingnan Ding, Yihao Liang, Bing-Sui Lu, and Xiangjun Xing. Charge renormalization and charge oscillation in asymmetric primitive model of electrolytes. *J. Stat. Phys.*, 165(5):970–989, 2016.

[92] Tamás Pajkossy. Impedance of rough capacitive electrodes. *J. Electroanal. Chem.*, 364(1-2):111–125, 1994.

[93] LI Daikhin, AA Kornyshev, and M Urbakh. Double-layer capacitance on a rough metal surface. *Phys. Rev. E*, 53(6):6192, 1996.

[94] Eric M Vrijenhoek, Seungkwan Hong, and Menachem Elimelech. Influence of membrane surface properties on initial rate of colloidal fouling of reverse osmosis and nanofiltration membranes. *Journal of Membrane Science*, 188(1):115–128, 2001.

[95] Subir Bhattacharjee, Chun-Han Ko, and Menachem Elimelech. Dlvo interaction between rough surfaces. *Langmuir*, 14(12):3365–3375, 1998.

[96] W Richard Bowen and Teodora A Doneva. Atomic force microscopy studies of membranes: effect of surface roughness on double-layer interactions and particle adhesion. *J. Colloid Interface Sci.*, 229(2):544–549, 2000.

[97] W Richard Bowen, Teodora A Doneva, and J Austin G Stoton. The use of atomic force microscopy to quantify membrane surface electrical properties. *Colloids and*

Surfaces A: Physicochemical and Engineering Aspects, 201(1):73–83, 2002.

[98] Scott A Bradford and Saeed Torkzaban. Colloid interaction energies for physically and chemically heterogeneous porous media. *Langmuir*, 29(11):3668–3676, 2013.

[99] R. Messina, E. González-Tovar, M. Lozada-Cassou, and C. Holm. Overcharging: The crucial role of excluded volume. *Europhys. Lett.*, 60:383–389, 2002.

[100] Leo Lue and Per Linse. Macroion solutions in the cell model studied by field theory and Monte Carlo simulations. *J. Chem. Phys.*, 135(22):224508, 2011.

[101] Alireza Mashaghi, P Partovi-Azar, Tayebeh Jadidi, Nasser Nafari, Philipp Maass, M Reza Rahimi Tabar, Mischa Bonn, and Huib J Bakker. Hydration strongly affects the molecular and electronic structure of membrane phospholipids. *J. Chem. Phys.*, 136(11):114709, 2012.

[102] JP Dilger, SG McLaughlin, TJ McIntosh, and SA Simon. The dielectric constant of phospholipid bilayers and the permeability of membranes to ions. *Science*, 206(4423):1196–1198, 1979.

[103] Pu Tian. Computational protein design, from single domain soluble proteins to membrane proteins. *Chemical Society Reviews*, 39(6):2071–2082, 2010.

[104] Kendall E. Atkinson. *The Numerical Solution of Integral Equations of the Second Kind*. Cambridge University Press, Cambridge, U.K., 1997.

[105] Alexander H. Boschitsch, Marcia O. Fenley, and Huan-Xiang Zhou. Fast boundary element method for the linear Poisson–Boltzmann equation. *J. Phys. Chem. B*, 106(10):2741–2754, 2002.

[106] André Buchau and Wolfgang M. Rucker. Preconditioned fast adaptive multipole boundary-element method. *IEEE Transactions on Magnetics*, 38(2):461–464, 2002.

[107] Michael D. Altman, Jaydeep P. Bardhan, Jacob K. White, and Bruce Tidor. Accurate solution of multi-region continuum biomolecule electrostatic problems using the linearized poisson–boltzmann equation with curved boundary elements. *J. Comput. Chem.*, 30(1):132–153, 2009.

[108] Ming Han, Huanxin Wu, and Erik Luijten. Electric double layer of anisotropic dielectric colloids under electric fields. *Eur. Phys. J. Special Topics*, 225:685–698, 2016.

[109] Michael K. Gilson and Barry Honig. Calculation of the total electrostatic energy of a macromolecular system: Solvation energies, binding energies, and conformational analysis. *Proteins*, 4(1):7–18, January 1988.

[110] Michael K. Gilson, Kim A Sharp, and Barry H. Honig. Calculating the electrostatic potential of molecules in solution: Method and error assessment. *J. Comput. Chem.*, 9(4):327–335, June 1988.

[111] Nathan A. Baker, David Sept, Simpson Joseph, Michael J. Holst, and J. Andrew McCammon. Electrostatics of nanosystems: Application to microtubules and the ribosome. *Proc. Natl. Acad. Sci. U.S.A.*, 98(18):10037–10041, August 2001.

[112] Sining Yu, Yongcheng Zhou, and G. W. Wei. Matched interface and boundary (MIB) method for elliptic problems with sharp-edged interfaces. *J. Comp. Phys.*, 224(2):729–756, June 2007.

[113] Tony J. You and Stephen C. Harvey. Finite element approach to the electrostatics of macromolecules with arbitrary geometries. *J. Comput. Chem.*, 14(4):484–501, April 1993.

[114] M. Holst, N. Baker, and F. Wang. Adaptive multilevel finite element solution of the Poisson–Boltzmann equation I. Algorithms and examples. *J. Comput. Chem.*, 21(15):1319–1342, November 2000.

[115] R. J. Zauhar and R. S. Morgan. Computing the electric potential of biomolecules: Application of a new method of molecular surface triangulation. *J. Comput. Chem.*, 11(5):603–622, 1990.

[116] Jaydeep P. Bardhan. Numerical solution of boundary-integral equations for molecular electrostatics. *J. Chem. Phys.*, 130(9):094102, 2009.

[117] Lothar Gaul, Martin Kögl, and Marcus Wagner. *Boundary Element Methods for Engineers and Scientists.* Springer, Berlin, 2013.

[118] Desző Boda, Mónika Valiskó, Bob Eisenberg, Wolfgang Nonner, Douglas Henderson, and Dirk Gillespie. The effect of protein dielectric coefficient on the selectivity of a calcium channel. *J. Chem. Phys.*, 125:034901, 2006.

[119] Johannes Tausch, Junfeng Wang, and Jacob White. Improved integral formulations for fast 3-D method-of-moments solvers. *IEEE Trans. Comput.-Aided Des. Integr. Circuits Syst.*, 20(12):1398–1405, 2001.

[120] T. P. Doerr and Yi-Kuo Yu. Electrostatics in the presence of dielectrics: The benefits of treating the induced surface charge density directly. *Am. J. Phys.*, 72(2):190–196, 2004.

[121] Nicholas J. Higham. *Accuracy and Stability of Numerical Algorithms.* SIAM, Philadelphia, 2nd edition, 2002.

[122] Roland W. Freund, Gene H. Golub, and Noël M. Nachtigal. Iterative solution of linear systems. *Acta Numer.*, 1:57–100, 1992.

[123] Michele Benzi. Preconditioning techniques for large linear systems: A survey. *J. Comp. Phys.*, 182(2):418–477, 2002.

[124] Edward W. Larsen and Jim E. Morel. Advances in discrete-ordinates methodology. In Yousry Azmy and Enrico Sartori, editors, *Nuclear Computational Science: A Century in Review*, chapter 1. Springer, Dordrecht, 2010.

[125] Youcef Saad. Numerical solution of large nonsymmetric eigenvalue problems. *Comput. Phys. Commun.*, 53(1):71–90, 1989.

[126] Zecheng Gan, Xiangjun Xing, and Zhenli Xu. Effects of image charges, interfacial charge discreteness, and surface roughness on the zeta potential of spherical electric double layers. *J. Chem. Phys.*, 137(3):034708, 2012.

[127] Robert O. James and George A. Parks. Characterization of aqueous colloids by their electrical double-layer and intrinsic surface chemical properties. In Egon Matijević, editor, *Surface and Colloid Science*, volume 12, chapter 2, pages 119–216. Plenum, New York, 1982.

[128] Amar B. Pawar and Ilona Kretzschmar. Fabrication, assembly, and application of patchy particles. *Macromol. Rapid Commun.*, 31(2):150–168, 2010.

[129] S. Jiang, Q. Chen, M. Tripathy, E. Luijten, K. S. Schweizer, and S. Granick. Janus particle synthesis and assembly. *Adv. Mater.*, 22:1060–1071, 2010.

[130] Andreas Walther and Axel H. E. Müller. Janus particles: Synthesis, self-assembly, physical properties, and applications. *Chem. Rev.*, 113(7):5194–5261, July 2013.

[131] Jie Zhang, Erik Luijten, and Steve Granick. Toward design rules of directional Janus colloidal assembly. *Ann. Rev. Phys. Chem.*, 66(1):581–600, 2015.

[132] T. Nisisako, T. Torii, T. Takahashi, and Y. Takizawa. Synthesis of monodisperse bicolored Janus particles with electrical anisotropy using a microfluidic co-flow system. *Adv. Mater.*, 18(9):1152–1156, 2006.

[133] Liang Hong, Angelo Cacciuto, Erik Luijten, and Steve Granick. Clusters of charged Janus spheres. *Nano Letters*, 6:2510–2514, 2006.

[134] Qian Chen, Jonathan K. Whitmer, Shan Jiang, Sung Chul Bae, Erik Luijten, and Steve Granick. Supracolloidal reaction kinetics of Janus spheres. *Science*, 331:199–202, 2011.

[135] Shan Jiang, Jing Yan, Jonathan K. Whitmer, Stephen M. Anthony, Erik Luijten, and Steve Granick. Orientationally glassy crystals of Janus spheres. *Phys. Rev. Lett.*, 112(21):218301, 2014.

[136] Jing Yan, Moses Bloom, Sung Chul Bae, Erik Luijten, and Steve Granick. Linking synchronization to self-assembly using magnetic Janus colloids. *Nature*, 491:578–581, 2012.

[137] Stoyan K. Smoukov, Sumit Gangwal, Manuel Marquez, and Orlin D. Velev. Reconfigurable responsive structures assembled from magnetic Janus particles. *Soft Matt.*, 5:1285–1292, 2009.

[138] Sumit Gangwal, Olivier J. Cayre, Martin Z. Bazant, and Orlin D. Velev. Induced-charge electrophoresis of metallodielectric particles. *Phys. Rev. Lett.*, 100(5):058302, 2008.

[139] Matthew C. Hagy and Rigoberto Hernandez. Dynamical simulation of dipolar Janus colloids: Equilibrium structure and thermodynamics. *J. Chem. Phys.*, 137(4):044505, 2012.

[140] Mahdy Malekzadeh Moghani and Bamin Khomami. Self-assembly of spherical Janus particles in electrolytes. *Soft Matt.*, 9(19):4815–4821, 2013.

[141] Sidney J. de Carvalho, Ralf Metzler, and Andrey G. Cherstvy. Critical adsorption of polyelectrolytes onto charged Janus nanospheres. *Phys. Chem. Chem. Phys.*, 16(29):15539–15550, 2014.

[142] Sumit Gangwal, Olivier J. Cayre, and Orlin D. Velev. Dielectrophoretic assembly of metallodielectric Janus particles in AC electric fields. *Langmuir*, 24(23):13312–13320, 2008.

[143] Huanxin Wu and Erik Luijten. Accurate and efficient numerical simulation of dielectrically anisotropic particles, 2017. submitted.

[144] Rui Wang and Zhen-Gang Wang. Continuous self-energy of ions at the dielectric interface. *Phys. Rev. Lett.*, 112:136101, Apr 2014.

[145] Florian Fahrenberger, Owen A. Hickey, Jens Smiatek, and Christian Holm. Importance of varying permittivity on the conductivity of polyelectrolyte solutions. *Phys. Rev. Lett.*, 115:118301, Sep 2015.

[146] R. W. Hockney and J. W. Eastwood. *Computer Simulation Using Particles.* McGraw-Hill, New York, 1981.

[147] Sven H. Behrens and David G. Grier. The charge of glass and silica surfaces. *J. Chem. Phys.*, 115(14):6716–6721, 2001.

[148] J. Sonnefeld, A. Göbel, and W. Vogelsberger. Surface charge density on spherical silica particles in aqueous alkali chloride solutions. Part 1. Experimental results. *J. Colloid Polym. Sci.*, 273(10):932–938, 1995.

[149] Jacob N. Israelachvili. *Intermolecular and Surface Forces.* Academic, San Diego, 3rd edition, 2011.

[150] Damien WM Arrigan. Nanoelectrodes, nanoelectrode arrays and their applications. *Analyst*, 129(12):1157–1165, 2004.

[151] A Bezryadin, C Dekker, and G Schmid. Electrostatic trapping of single conducting nanoparticles between nanoelectrodes. *Appl. Phys. Lett.*, 71(9):1273–1275, 1997.

[152] David E Goldman. Potential, impedance, and rectification in membranes. *The Journal of general physiology*, 27(1):37–60, 1943.

[153] Ivar Fredholm. Sur une classe déquations fonctionnelles. *Acta mathematica*, 27(1):365–390, 1903.

[154] SG Mikhlin, N Sneddon, and S Ulam. Integral equations. international series of monographs on pure and applied mathematics 4, 1957.

[155] David M Heyes. Pressure tensor of partial-charge and point-dipole lattices with bulk and surface geometries. *Phys. Rev. B*, 49(2):755, 1994.

[156] Huimin Lin, Huazhong Tang, and Wei Cai. Accuracy and efficiency in computing electrostatic potential for an ion channel model in layered dielectric/electrolyte media. *J. Comp. Phys.*, 259:488–512, 2014.

[157] Mary Hongying Cheng and Rob D Coalson. An accurate and efficient empirical approach for calculating the dielectric self-energy and ion-ion pair potential in continuum models of biological ion channels. *The Journal of Physical Chemistry B*, 109(1):488–498, 2005.

[158] Dezső Boda, Douglas Henderson, Bob Eisenberg, and Dirk Gillespie. A method for treating the passage of a charged hard sphere ion as it passes through a sharp

dielectric boundary. *J. Chem. Phys.*, 135(6):064105, 2011.

[159] Berk Hess, Christian Holm, and Nico van der Vegt. Modeling multibody effects in ionic solutions with a concentration dependent dielectric permittivity. *Phys. Rev. Lett.*, 96(14):147801, 2006.

[160] F Booth. The dielectric constant of water and the saturation effect. *J. Chem. Phys.*, 19(4):391–394, 1951.

[161] Florian Fahrenberger, Zhenli Xu, and Christian Holm. Simulation of electric double layers around charged colloids in aqueous solution of variable permittivity. *The Journal of chemical physics*, 141(6):064902, 2014.

[162] AC Maggs and Vincent Rossetto. Local simulation algorithms for coulomb interactions. *Phys. Rev. Lett.*, 88(19):196402, 2002.

[163] Frank Stern. Image potential near a gradual interface between two dielectrics. *Physical Review B*, 17(12):5009, 1978.

[164] Milton J Rosen and Joy T Kunjappu. *Surfactants and interfacial phenomena*. John Wiley & Sons, 2012.

[165] Adolf Heydweiller. Über physikalische eigenschaften von lösungen in ihrem zusammenhang. ii. oberflächenspannung und elektrisches leitvermögen wässeriger salzlösungen. *Ann. Phys. (Leipzig)*, 338(11):145–185, 1910.

[166] Malcolm Dole. Surface tension of strong electrolytes. *Nature*, 140:464–465, 1937.

[167] GM Bell and PD Rangecroft. Theory of surface tension for a 2-1 electrolyte solution. *Trans. Faraday Soc.*, 67:649–659, 1971.

[168] AM Gabovich and AI Veitenko. Surface tension at the interface between electrolyte solution and metal (semiconductor) electrode. spatial dispersion effects. *Electrochimica acta*, 28(12):1771–1776, 1983.

[169] LB Bhuiyan, Dušan Bratko, and CW Outhwaite. Electrolyte surface tension in the modified poisson-boltzmann approximation. *J. Phys. C*, 95(1):336–340, 1991.

[170] Mathias Boström, David RM Williams, and Barry W Ninham. Surface tension of electrolytes: specific ion effects explained by dispersion forces. *Langmuir*, 17(15):4475–4478, 2001.

[171] Yan Levin and JE Flores-Mena. Surface tension of strong electrolytes. *Europhys. Lett.*, 56(2):187, 2001.

[172] Hiroyuki Ohshima and Hiroki Matsubara. Surface tension of electrolyte solutions. *J. Colloid Polym. Sci.*, 282(9):1044–1048, 2004.

[173] Yan Levin, Alexandre P Dos Santos, and Alexandre Diehl. Ions at the air–water interface: an end to a hundred-year-old mystery? *Phys. Rev. Lett.*, 103(25):257802, 2009.

[174] Grinnell Jones and Wendell A Ray. The surface tension of solutions of electrolytes as a function of the concentration. i. a differential method for measuring relative surface tension. *J. Am. Chem. Soc.*, 59(1):187–198, 1937.

[175] Neldon L Jarvis and Milton A Scheiman. Surface potentials of aqueous electrolyte solutions. *J. Phys. C*, 72(1):74–78, 1968.

[176] L Šamaj and B Jancovici. Surface tension of a metal–electrolyte boundary: Exactly solvable model. *J. Stat. Phys.*, 103(5-6):717–735, 2001.

[177] Ching-Hung Ho, Heng-Kwong Tsao, and Yu-Jane Sheng. Interfacial tension of a salty droplet: Monte carlo study. *J. Chem. Phys.*, 119(4):2369–2375, 2003.

[178] André Bellemans. The surface tension of ionic solutions: I. derivation of the limiting law at infinite dilution from the poisson-boltzmann equation. *Physica*, 30(4):924–930, 1964.

[179] Hiroyuki Ohshima. Surface tension of general electrolyte solutions. *J. Colloid Polym. Sci.*, 283(2):119–124, 2004.

[180] E. R. Nightingale, Jr. Phenomenological theory of ion solvation. effective radii of hydrated ions. *J. Chem. Phys.*, 63:1381–1387, September 1959.

[181] Huanxin Wu, Mingnan Ding, Xiangjun Xing, and Erik Luijten. Surface tension of asymmetric electrolyte solutions, 2017. in preparation.

[182] David J. Griffiths. *Introduction to Electrodynamics*. Prentice Hall, Upper Saddle River, New Jersey, 3rd edition, 1999.

[183] In-Chul Yeh and Max L Berkowitz. Ewald summation for systems with slab geometry. *J. Chem. Phys.*, 111(7):3155–3162, 1999.

[184] Zecheng Gan, Shidong Jiang, Erik Luijten, and Zhenli Xu. A hybrid method for systems of closely spaced dielectric spheres and ions. *SIAM Journal on Scientific Computing*, 38(3):B375–B395, 2016.